

## Master Thesis

# Reaction Paths of Repair Fragments on Damaged Ultra-low-k Surfaces

B. Sc. Anja Förster

Chemnitz, 25.09.2014

**First Examiner:** Prof. Dr. Sibylle Gemming  
Professorship “Skalenübergreifende Modellierung von Materialien und  
Materialverbünden unter externen Einflussfaktoren”  
Faculty of Natural Science  
Technische Universität Chemnitz

---

**Second Examiner:** Prof. Dr. Stefan E. Schulz  
Department Head Back-end of Line, Fraunhofer ENAS  
Honorary Professorship ”Technologien der Nanoelektronik”  
Faculty of Electrical Engineering and Information Technology  
Technische Universität Chemnitz

B.Sc. Anja Förster

Master Thesis

Reaction Paths of Repair Fragments on Damaged Ultra-low-k Surfaces

Technische Universität Chemnitz, Faculty of Natural Science

Chemnitz, 25.09.2014

# Contents

<b>Table of Contents</b>	<b>i</b>
<b>List of Figures</b>	<b>ii</b>
<b>List of Tables</b>	<b>iv</b>
<b>Abbreviations</b>	<b>vii</b>
<b>Symbols</b>	<b>ix</b>
<b>Abstract</b>	<b>xiii</b>
<b>1. Introduction</b>	<b>1</b>
<b>2. Theoretical Background</b>	<b>3</b>
2.1. Ultra-low-k Materials . . . . .	3
2.1.1. Definition, Usage and Challenges . . . . .	3
2.1.2. k-Restore . . . . .	5
2.2. Reaction Theory . . . . .	8
2.2.1. Reaction Process . . . . .	8
2.2.2. Thermal Influence . . . . .	9
<b>3. Computational Methods</b>	<b>11</b>
3.1. Overview . . . . .	11
3.2. Density Functional Theory . . . . .	12
3.2.1. Theoretical Background . . . . .	12
3.2.1.1. The Schrödinger Equation and the Variational Principle . . . . .	12
3.2.1.2. From the Electron Density to the Kohn-Sham Approach . . . . .	14
3.2.1.3. Exchange-Correlation Functionals and Basis Sets . . . . .	15
3.2.2. Used Program Packages . . . . .	18
3.3. ReaxFF . . . . .	19
3.3.1. Theoretical Background . . . . .	19
3.3.2. Used Program Packages . . . . .	20
<b>4. Model System</b>	<b>21</b>
4.1. Damaged ULK Materials . . . . .	21
4.1.1. ULK-Fragments . . . . .	21
4.1.2. Silicon Oxide Cluster . . . . .	22
4.2. Repair Fragments . . . . .	25
4.2.1. Overview . . . . .	25
4.2.2. Fragmentation of DMADMS . . . . .	26
4.2.3. Fragmentation of OMCTS . . . . .	29
4.2.4. Continuing Reactions . . . . .	32

<b>5. Results and Discussion</b>	<b>35</b>
5.1. Reactions between Repair Fragments and ULK-Fragments . . . . .	35
5.1.1. Repair of OH-damages . . . . .	35
5.1.2. Repair of H-damages . . . . .	37
5.1.3. Selected Repair Reactions with Gaussian . . . . .	39
5.2. Reactions Between Repair Fragments and Silicon Oxide Cluster . . . . .	42
5.2.1. Comparison Between ULK-Fragments and Silicon Oxide Cluster . . . . .	42
5.2.2. Comparability of DFT and MD Results . . . . .	43
5.3. Comparison with Experimental Results . . . . .	46
<b>6. Summary and Outlook</b>	<b>49</b>
<b>A. Appendix</b>	<b>51</b>
A.1. Temperature Influence . . . . .	51
A.1.1. Temperature Influence on the DMADMS Fragmentation in Dmol <sup>3</sup> . . . . .	51
A.1.2. Temperature Influence on the OMCTS Fragmentation in Dmol <sup>3</sup> . . . . .	51
A.2. Tests . . . . .	53
A.2.1. DMADMS Fragmentation with Gaussian . . . . .	53
A.2.2. G2 Test Set . . . . .	53
A.2.3. Calculation Time of the Silicon Oxide Cluster in Dmol <sup>3</sup> . . . . .	54
A.3. Error Analysis . . . . .	55
A.3.1. Basis Set Superposition Error in Dmol <sup>3</sup> . . . . .	55
A.3.2. Dispersion Correction . . . . .	55
A.4. Illustration of Defects . . . . .	57
A.5. Bookmark . . . . .	58
<b>Bibliography</b>	<b>58</b>
<b>Acknowledgment</b>	<b>65</b>
<b>Statement of Authorship</b>	<b>67</b>



# List of Figures

1.1. Moore's law vs. reality . . . . .	1
2.1. SSQ and SiCOH basic structures . . . . .	3
2.2. Overview of ULK/LK materials . . . . .	4
2.3. Silylation with DMADMS and HMDS . . . . .	5
2.4. Overview of possible plasma repair fragments . . . . .	7
2.5. Reaction process . . . . .	8
2.6. Overview of reaction processes . . . . .	9
2.7. Exemplary entropy correction for OMCTS . . . . .	10
3.1. Overview of computational methods . . . . .	11
3.2. Scaling of HF, ReaxFF and post-HF methods . . . . .	12
3.3. Correlation between the basis set size and the calculation time . . . . .	17
4.1. Overview ULK-fragments . . . . .	22
4.2. Basic structure of the silica cluster . . . . .	22
4.3. Top view of the minimal silicon oxide cluster . . . . .	23
4.4. Silicon oxide cluster . . . . .	24
4.5. Overview repair fragments . . . . .	25
4.6. DMADMS and OMCTS . . . . .	26
4.7. Scheme of the DMADMS fragmentation . . . . .	26
4.8. Fragmentation of DMADMS with Lammmps . . . . .	27
4.9. Fragmentation of DMADMS . . . . .	28
4.11. Dependency between the number of products and the reaction energy . . . . .	29
4.10. Scheme of the OMCTS fragmentation . . . . .	30
4.12. Fragmentation of OMCTS . . . . .	31
4.13. Mass spectroscopy results . . . . .	31
4.14. Continuing reactions of the repair fragments . . . . .	32
4.15. Continuing reactions . . . . .	33
5.1. Repair of OH-damages . . . . .	35
5.2. Exemplary OH-damage repair reactions . . . . .	36
5.3. Exemplary OH <sub>2</sub> - and (OH) <sub>2</sub> -damage repair reactions . . . . .	37
5.4. Repair of H-damages . . . . .	37
5.5. Exemplary H-damage repair reactions . . . . .	38
5.6. Anomalous H-damage repair reactions . . . . .	38
5.7. OH-repair with Gaussian . . . . .	39
5.8. H-repair with Gaussian . . . . .	39
5.9. Gaussian and Dmol <sup>3</sup> H-repair calculations with different functionals . . . . .	40
5.10. Dmol <sup>3</sup> OH-repair calculations with different functionals . . . . .	41
5.11. OH-repair on the silicon oxide cluster . . . . .	42
5.12. H-repair on the silicon oxide cluster . . . . .	43
5.13. OH-repair with MD . . . . .	44

## List of Figures

5.14. H-repair with MD . . . . .	44
5.15. Silicon oxide cluster from Dmol <sup>3</sup> and Lammmps calculations . . . . .	45
5.16. Experimental repair of damaged ULK materials . . . . .	46
6.1. The most effective repair fragments . . . . .	50
A.1. Temperature influence on the DMADMS fragmentation in Dmol <sup>3</sup> . . . . .	51
A.2. Temperature influence on the OMCTS fragmentation in Dmol <sup>3</sup> . . . . .	52
A.3. Fragmentation of DMADMS with different Gaussian basis sets . . . . .	53
A.4. G2 test set comparison . . . . .	54
A.5. Energy and calculation time deviation . . . . .	54
A.6. BSSE for ULK-fragment repair reactions in Dmol <sup>3</sup> . . . . .	55
A.7. H-repair with dispersion correction . . . . .	56
A.8. Illustration of defects . . . . .	57
A.9. Bookmark . . . . .	58

# List of Tables

2.1. (Dis-)advantages of different k-restore methods . . . . .	6
3.1. Overview calculation details DFT . . . . .	18
3.2. Overview calculation details ReaxFF . . . . .	20
3.3. Overview ReaxFF parameter sets for Lammmps . . . . .	20



# Abbreviations

<b>BSSE</b>	Basis set superposition error
<b>CC</b>	Coupled cluster
<b>CFD</b>	Computational fluid dynamics
<b>CGF</b>	Contracted Gaussian functions
<b>CH<sub>4</sub> plasma</b>	Hydrocarbon plasma
<b>DEMS</b>	Diethoxymethylsilane
<b>DFT</b>	Density functional theory
<b>DFT-D</b>	Density functional theory with dispersion correction
<b>DMA</b>	Dimethylamine
<b>DMADMS</b>	Bis(dimethylamino)-dimethylsilane
<b>ENAS</b>	[Fraunhofer Institute for] Electronic Nano Systems
<b>GGA</b>	Generalized gradient approximation
<b>GTO</b>	Gaussian-type-orbital
<b>HF</b>	Hartree-Fock
<b>HMDS</b>	Hexamethyldisilazane
<b>HMX</b>	Octahydro-1,3,5,7- tetranitro-1,3,5,7-tetrazocine
<b>HSSQ</b>	Hydrogen-silsesquioxane
<b>IC</b>	Integrated circuit
<b>KMC</b>	Kinetic Monte Carlo
<b>LDA</b>	Local-density approximation
<b>LK</b>	Low-k
<b>LSD</b>	Local spin-density approximation
<b>MD</b>	Molecular dynamics
<b>MM</b>	Molecular mechanics
<b>MP</b>	Møller–Plesset
<b>MSSQ</b>	Methyl-silsesquioxane

## *Abbreviations*

**OMCTS** Octamethylcyclotetrasiloxane

**p-SiCOH** Porous silica based materials

**PECVD** Plasma enhanced chemical vapor deposition

**PGTO** Primitive Gaussian-type-orbital

**post-HF** post Hartree-Fock

**ReaxFF** Reactive Force Field

**SiCOH** Silica based materials

**SiOH** Silanol group

**SiO<sub>y</sub>(CH<sub>3</sub>)<sub>x</sub>H<sub>z</sub>** Plasma repair fragments, with  $y = \{0; 1; 2\}$ ,  $x \in \{1; 2; 3\}$  and  $z = \{0; 1; 2\}$

**SOD** Spin-on Dielectrics

**SSQ** Silsesquioxane

**STO** Slayter-type-orbital

**TATB** 1,3,5-triamino-2,4,6-trinitrobenzene

**TMAS** Trimethylaminosilane

**TS** Transition state

**ULK** Ultra-low-k

**ZPVE** Zero-point vibrational energy

# Symbols

$\pm$  Additional diffuse functions in Gaussian basis set

$*$  Additional polarization functions in Gaussian basis set

$A$  Surface area

$\alpha, \beta$  Electron spins

$C$  Capacitance

$C_{par}$  Parasitic capacitance

$c_{i\mu}$  Coefficients to construct the wave function from the basis set

$d$  Thickness

$d_{\alpha\tau}$  Contraction coefficient

$E$  Energy

$E_A$  Activation energy

$E_0$  Ground state energy

$E_b$  Energy gained from the approximated wave function

$E_{bond}$  Bond energy

$E_{BSSE}$  Basis set superposition error energy difference

$E_{conj}$  Energy from conjugated effects

$E_{Coulomb}$  Energy from Coulomb interaction

$E_{Dimer}$  Energy of the dimer

$E_{Educts}$  Ground state energy of the educts

$E_{ee}$  Electron-electron interaction energy

$E_{elec}$  Electron energy

$E_{lp}$  Energy contribution from lone electron pairs

$E_{Monomer}$  Energy of the monomer

$E_{ncl}$  Non-classical electron-electron interaction energy

$E_{ne}$  Nucleus-electron interaction energy

$E_{nuc}$  Nucleus-nucleus interaction energy

## Symbols

$E_{over}$	Energy penalty for overcoordinated atoms
$E_{pen}$	Energy penalty for double bonds sharing an atom
$E_{Products}$	Ground state energy of the products
$E_R$	Reaction energy
$E_{rot}$	Rotational energy
$E_{system}$	Total energy of the system
$E_{tor}$	Energy contribution from the torsion angle
$E_{tot}$	Total energy
$E_{trans}$	Translational energy
$E_{TS}$	Energy of the transition state
$E_{under}$	Energy penalty for undercoordinated atoms
$E_{val}$	Energy contribution for the valence angles
$E_{vdWaals}$	Energy from van der Waals interaction
$E_{vib}$	Vibrational energy
$E_{XC}$	Exchange-correlation energy
$\epsilon_0$	Electric constant
$\epsilon_{XC}$	Exchange-correlation energy of the electron gas
$\epsilon_r, \kappa$	Dielectric constant
$\eta_\mu$	Basis set
$F_{HK}$	Hohenberg-Kohn functional
$G$	Gibbs free energy
$G(T)$	Gibbs free energy correction
$\Delta G_A(T)$	Gibbs free energy correction for the activation energy
$\Delta G_R(T)$	Gibbs free energy correction for the reaction energy
$H$	Enthalpy
$H(T)$	Enthalpy correction
$\hat{H}$	Hamilton operator
$\tilde{\hat{H}}$	Trial Hamilton operator
$\hat{H}_{elec}$	Electronic Hamilton operator
$J$	Classical Coulomb interaction



$L$  Orbital quantum number  
 $\lambda$  Coupling strength parameter  
 $\lambda_i$  ReaxFF fitting parameters  
 $M$  Number of nuclei  
 $M_A$  Nucleus mass  
 $N$  Number of electrons **or** number of atoms (in LAMMPS)  
 $n$  Principal quantum number  
 $p_{over}$  Bond parameter  
 $\phi_i$  One-electron functional  
 $\psi$  Wave function  
 $\tilde{\psi}$  Trial wave function  
 $\psi_0$  Ground state wave function  
 $\psi_b$  Approximated wave function  
 $\psi_{elec}$  Electronic wave function  
 $R$  Ohmic resistance **or** ideal gas constant  
 $\vec{r}_i$  Spatial coordinates  
 $r_{xy}$  Electron-electron, electron-nucleus or nucleus-nucleus distance  
 $\rho$  Electron density  
 $\tilde{\rho}$  Trial density  
 $\rho_\alpha, \rho_\beta$  Electron density belonging to the electrons with spins  $\alpha$  or  $\beta$   
 $S$  Entropy  
 $S(T)$  Entropy correction  
 $s_i$  Spin coordinates  
 $S_{rot}$  Rotational contribution to the entropy  
 $S_{trans}$  Translational contribution to the entropy  
 $S_{vib}$  Vibrational contribution to the entropy  
 $T$  Temperature  
 $\hat{T}_C$  Kinetic energy difference between the reference system and the real system  
 $\hat{T}_e$  Kinetic energy of the electrons  
 $\hat{T}_S$  Kinetic energy of the reference system

## *Symbols*

$\tau$  Delay time

$V$  Volume

$\hat{V}_{ee}$  Potential energy between electrons

$\hat{V}_{en}$  Potential energy between electrons and nuclei

$\hat{V}_{ext}$  External potential

$\hat{V}_{nn}$  Potential energy between nuclei

$\vec{x}_i$  Electron coordinates

$\xi$  Orbital exponent

$Y_{lm}$  Spherical harmonics

$Z_M$  Nucleus charge

# Abstract

In the present work, the plasma repair for damaged ultra-low-k (ULK) materials, newly developed at the Fraunhofer ENAS, is studied with density functional theory (DFT) and molecular dynamic (MD) methods to obtain new insights into this repair mechanism. The ULK materials owe their low dielectric constant (k-value) to the insertion of k-value lowering methyl groups. During the manufacturing process, the ULK materials are damaged and their k-values increase due to the adsorption of hydroxyl groups (OH-damage) and hydrogen atoms (H-damage) that replaced the methyl groups.

The first investigation point is the creation of repair fragments. For this purpose the silylation molecules bis(dimethylamino)-dimethylsilane (DMADMS) and octamethylcyclotetrasiloxane (OMCTS) are fragmented. Here, only fragmentation reactions that lead to repair fragments that contain one silicon atom and at least one methyl group were considered. It is shown that the repair fragments that contain three methyl groups are preferred, especially in a methyl rich atmosphere.

The effectivity of the obtained repair fragments to cure an OH- and H-damage are investigated with two model systems. The first system consists of an assortment of small ULK-fragments, which is used to scan through the wide array of possible repair reactions. The second system is a silicon oxide cluster that investigates whether the presence of a cluster influences the reaction energies.

In both model systems, repair fragments that contain three methyl groups or two oxygen atoms are found to be most effective. Finally, the quantum chemical results are compared to experimental findings to get deeper insight into the repair process.



# 1. Introduction

The aim of the microelectronic industry's development of integrated circuits (ICs) over the last decades can be summarized as '*smaller and faster*'. From the 250 nm technology in 1997 [1], now in 2014 the 14 nm technology is used [2]. This development over the years was fueled by Moore's law.

In 1965 Gordon E. Moore predicted that the number of transistors per IC would double yearly [3] and corrected the statement in 1975 to every two years [4]. Moore's prediction, or Moore's law, is in good agreement with the actual development as shown in figure 1.1.

Microprocessor Transistor Counts 1971-2011 & Moore's Law

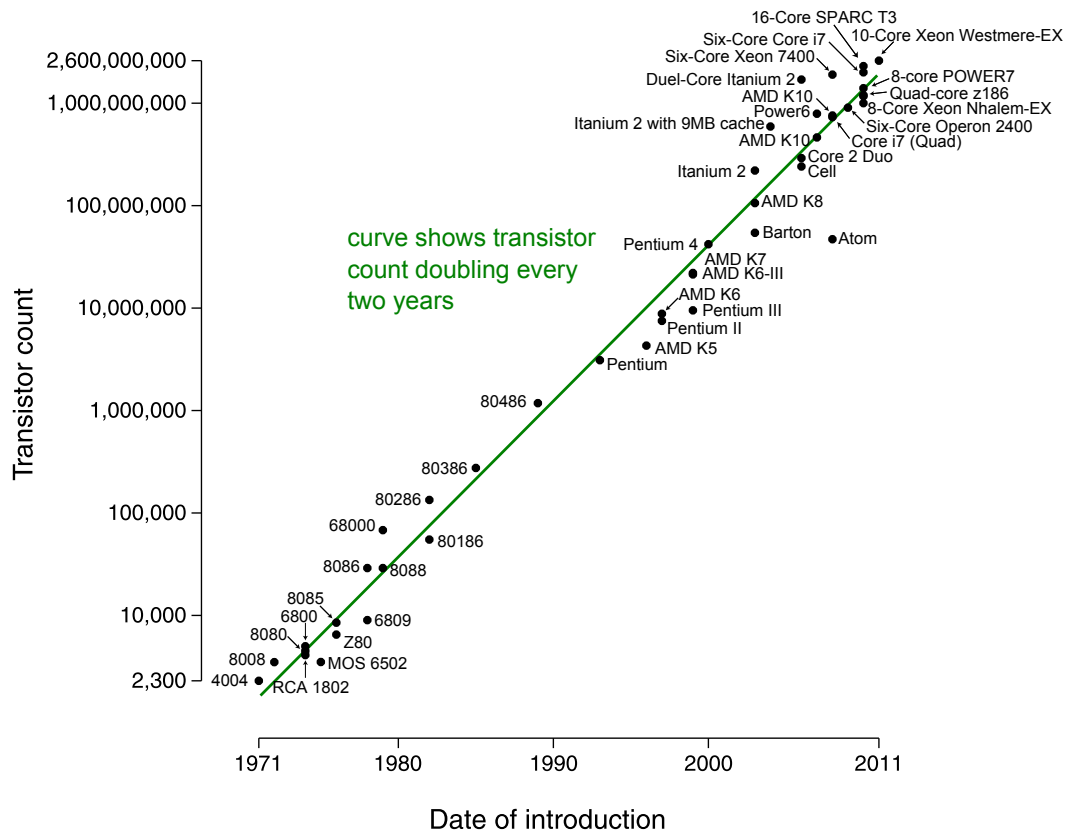


Figure 1.1.: Moore's law vs. reality. Modified from [5].

While this development led to personal computers becoming more powerful over the last years, there is one major problem nowadays: '*Smaller and faster*' do not go hand in hand anymore. With the reduction of the chip size, the signal delay time  $\tau$  caused by the interconnects increases. As  $\tau$  is defined as

$$\tau = RC \quad (1.1)$$

## 1. Introduction

and therefore dependent on the ohmic resistance  $R$  and the capacitance  $C$  of the chip interconnect system, either of them needs to be reduced in order to decrease  $\tau$ .

$R$  was reduced by using the contact metal copper instead of alumina, minimizing  $R$  from  $0.027 \frac{\Omega\text{mm}^2}{\text{m}}$  to  $0.017 \frac{\Omega\text{mm}^2}{\text{m}}$  [6]. The parasitic capacitance  $C_{par}$  is defined as shown in equation 1.2 and is a part of the overall capacitance  $C$ .

$$C_{par} = \epsilon_0 \epsilon_r \frac{A}{d} \quad (1.2)$$

With the electric constant  $\epsilon_0$  being fixed and the surface area  $A$  and the thickness  $d$  being predetermined by the design of the chip<sup>1</sup>, only the dielectric constant  $\epsilon_r$  of the dielectric material in the on chip interconnect system can be changed.

$\epsilon_r$  is linked to the polarity of a material. Water with its strong polar bond has a dielectric constant value of about 80, whereas silicon oxide, the basis isolation material for ICs, has only a dielectric constant of 3.9 [7]. Improvements of the delay time can thus be achieved by use of carbon based materials whose  $\epsilon_r$  value is below that of silica. As  $\epsilon_r$  is also known as  $\kappa$  these materials are called low-k (LK) or ultra-low-k (ULK) materials. Often methyl groups are inserted into the material to decrease the  $\epsilon_r$  (k-value) of the material and thus  $\tau$ . However, the methyl groups are also prone to damage.

During the chip manufacturing process an increased k-value is observed in the interconnect dielectrics. This is due to loss of the k-value lowering methyl groups because of active radicals and highly energetic vacuum-ultra-violet photons that break the Si-CH<sub>3</sub>-bonds and lead to the formation of k-value raising Si-OH groups [8]. Thus, it is necessary to find ways to restore the k-value in situ during the back-end of line processes.

There are three k-restore processes in existence. One is the repair by silylation, the second is the hydrocarbon plasma repair and the third is the UV assisted thermal curing. All three methods have specific advantages and disadvantages. The silylation molecules can repair the surface damage, however they are too large to diffuse into the materials and restore the damage in the deeper regions of the porous ULK material. The small methyl groups from the hydrocarbon plasma repair, on the other hand, would be small enough to diffuse into the pores. However, they do not show a repair process at all; instead they build a carbon rich polymer film on the surface [9]. And while the UV assisted thermal curing removes water and hydroxyl groups from the ULK material, the ULK material is compressed at the same time.

Scientists at the Fraunhofer Institute for Electronic Nano Systems (ENAS) develop an in situ repair process which combines the advantages of all previously mentioned methods. Here, plasma fragmented silylation molecules are used to repair the material and thus restore the k-value. The reactivity of the silylation reaction is preserved while at the same time using molecule fragments which are small enough to also repair the damage in deeper regions [10].

The aim of the present work is to gain new insights to the experimental results which are described in [10] based on extensive modeling of reactions while also creating a model system, for testing the usability of possible new fragments. Density functional theory (DFT) and molecular dynamics (MD) will be used to study repair reactions with ULK-fragments and on a silicon oxide cluster.

The following chapter 2.1 will give an overview of ULK materials and how the k-value can be restored, while chapter 2.2 provides a short theoretical background on reaction kinetics. This is followed by the introduction of the used methods of this thesis in chapter 3. Chapter 4 covers the creation of the model system, while chapter 5 presents the simulation results followed by a short summary and outlook in chapter 6.

---

<sup>1</sup> $d$  is important for the operation condition reliability and  $A$  for the 3D integration.

## 2. Theoretical Background

### 2.1. Ultra-low-k Materials

#### 2.1.1. Definition, Usage and Challenges

In chapter 1 it was already mentioned that LK and ULK materials are materials whose dielectric constant  $\epsilon_r$  is below 3.9. In the present discussion, the material is only called ULK if its  $\epsilon_r \leq 2.4$  [11]. To gain such LK materials, the k-value of silica has to be reduced<sup>2</sup>. This can be done in two ways. Either by the integration of pores or by substituting the Si-O bond with less polarizable bonds. The first possibility lowers the k-value as air has a k-value of slightly over 1. Thus, the overall k-value of the porous material is reduced. However, the pores reduce the mechanical stability of the material. This makes this solution unfavorable as a certain mechanical stability is necessary for subsequent process steps like the chemical-mechanical planarization<sup>3</sup>.

The second option has the advantage that not only the k-value of the material is reduced by replacing the Si-O bond by less polarizable Si-F or Si-CH<sub>3</sub> bonds, but also that the insertion of fluorine and methyl groups lead to a larger atom distance. This larger distance and steric hindrance, especially from methyl, makes it easy to mix the positive effect on the k-value by the substitution of Si-O bonds with the integration of pores to create ULK materials. Here, the materials are divided into silsesquioxane (SSQ) and silica based (SiCOH) materials.

SSQ based materials received their name from the Latin word 'sesqui', meaning one and a half and is referring to the empirical formula  $(R-SiO_{1.5})_n$  of the basic structure (see figure 2.1). For the use in the microelectronic industry often hydrogen and methyl groups are used in place of R. These materials are then called hydrogen-silsesquioxane (HSSQ) or methyl-silsesquioxane (MSSQ). SSQ based materials are produced by spin-on deposition processes. This is why they are also known as spin-on dielectrics (SOD).

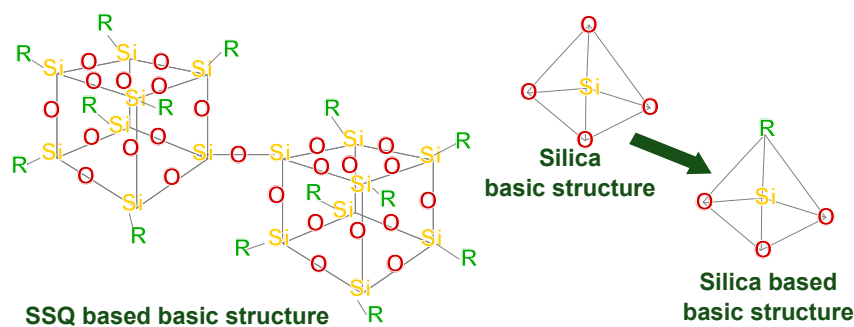


Figure 2.1.: Basic structure of silsesquioxane and silica based LK materials. Figure based on [12].

Silica based LK materials, on the other hand, have the tetrahedral structure of silica as their basic structure, where one oxygen atom is replaced by fluorine or methyl groups (see figure 2.1). They are fabricated by plasma enhanced chemical vapor deposition (PECVD). To deposit silica

<sup>2</sup>There are also non-silicon based LK materials, such as amorphous carbon; they will not be discussed in this thesis.

<sup>3</sup>The chemical-mechanical planarization is used to pattern the chips.

## 2. Theoretical Background

based LK materials precursors like octamethylcyclotetrasiloxane (OMCTS) or diethoxymethylsilane (DEMS) are used [13]. If the aim is to produce porous ULK materials (p-SiCOH), then a second organic precursor, named porogen, is added. After Grill et al. suggested this approach with CH in 2001 [14], other porogens such as butadiene monoxide and cyclopentene oxide [15] were successfully tested. In most cases, these porogens possess aromatic rings which provide steric hindrances that later become the pores [11].

Porosity is gained by heating the materials to 400°C. During this thermal treatment the incorporated porogens are evaporated from the ULK material. Usually this not only results in the creation of pores but also in the shrinkage of the ULK material, if not the collapse of the structure. To avoid the collapse, the porogen precursors have to be chosen such that the silicon atoms are only bound to one methyl group instead of two [11].

Figure 2.2 shows an overview of different SSQ and silica based LK/ULK materials with regard to the technology they are used for. The figure illustrates that while SSQ based materials reach lower k-values than silica based materials, for each technology node size both material groups are used. The reason behind this is that the smaller basic structure together with the PECVD make silica based LK materials the first choice for the use in the microelectronic industry. Also, silica based dielectrics are less prone to damage in comparison to SSQ based materials [13].

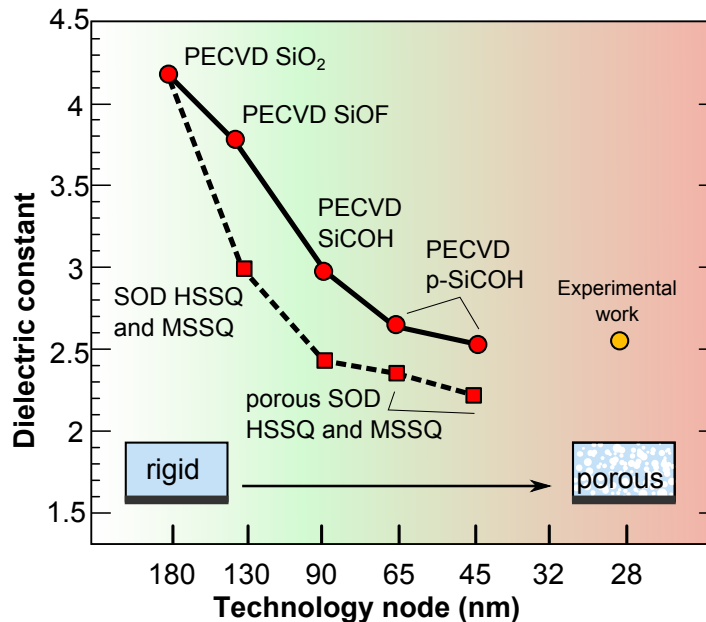


Figure 2.2.: Overview of ULK/LK materials. Translated from [10], based on [16]. The experimental work refers to [10].

The damage to the LK/ULK materials occurs during the patterning with reactive ion etching and during the thermal annihilation of the porogens. Hereby, in contrast to silica, the pores and methyl groups of the LK and ULK materials are prone to various attacks. During the etching process they are exposed to UV-light, radicals and ions [8]. The damage most often observed is a carbon depletion by radicals and ion bombardment [17]. This is especially critical as the created dangling Si bonds are replaced by Si-H bonds, which increase the k-value of the material. This damage structure is referred to as H-damage in this thesis. If the H-damages come into contact with air, they react to silanol groups (SiOH) [18]. This introduces OH-damages which raise the k-value even more due to the strongly polar bond between oxygen and hydrogen. Furthermore, the silanol groups are inclined to absorb water [19]. Because of all this, it is necessary to restore the k-value of the LK and ULK materials after the etching process by repairing the H- and OH-damage.



### 2.1.2. k-Restore

Today, three different types of k-restore processes exist. The first is the UV assisted thermal curing, the second is silylation and the third is the k-restore via hydrocarbon plasma ( $\text{CH}_4$  plasma) treatment.

The UV assisted thermal curing has the advantage that absorbed water molecules and silanol groups are removed from the material. The UV radiation together with the high temperatures provide the energy for the bond breaking and the evacuation of the removed molecules. However, this goes along with an undesired compression of the material [20]. Also, for a complete damage removal, temperatures of 600-1000°C are necessary, which lie in the critical range of the ULK materials' thermal stability [8].

The major advantage of the  $\text{CH}_4$  plasma treatment is that the methyl radicals, in theory, are small enough to diffuse into the pores of the ULK material. There, they replace the Si-OH groups with Si- $\text{CH}_3$ . However, in experiments it is observed that this desired repair reaction does not take place. Instead, the methyl radicals build a carbon rich layer on the surface of the ULK material [9]. While this carbon rich layer protects the ULK material from further moisture absorption and keeps the electrical property stable [21], no k-restore is achieved through the  $\text{CH}_4$  plasma treatment.

Opposed to the  $\text{CH}_4$  plasma, the k-restore by silylation is actually able to restore the k-value [22, 23, 24]. This happens via the reaction of the silanol groups with silylation molecules ( $\text{Si}(\text{CH}_3)_x\text{-R}$ ) such as OMCTS, bis(dimethylamino)-dimethylsilane (DMADMS) [25] or hexamethyldisilazane (HMDS) [26]. The k-value is once again lowered because methyl groups are reinserted into the ULK material and Si-O-H bonds are reformed into Si-O-Si- $\text{CH}_3$  bonds. Hereby, only the  $\text{Si}(\text{CH}_3)_x$  group of the silylation molecules is bound to the surface of the ULK material. The rest R reacts with the hydrogen atom of the OH-damage to R-H and, in the best case, leaves the material. Figure 2.3 shows exemplary repair reactions for HMDS and DMADMS.

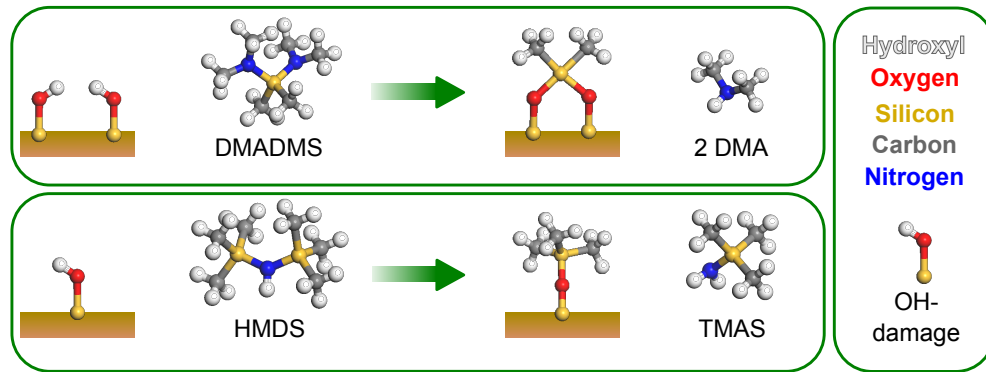


Figure 2.3.: Silylation with DMADMS and HMDS. The byproducts from a successful silylation with DMADMS or HMDS are dimethylamine (DMA) or trimethylaminosilane (TMAS).

The disadvantage of this repair process is that while the k-value can be restored, the repair process only takes place at the surface of the damaged ULK material [27]. The reason behind this is that the repair molecules are too large<sup>4</sup> to diffuse into the pores and the lower layers.

To sum up, the point in which one repair process is proficient, the other repair processes fail. Thus, up to now there is no k-restore process available which fulfills all requirements. However, if it is possible to combine the three methods' advantages, one would gain a new fourth method that

<sup>4</sup>DMADMS, OMCTS and HMDS have a size of 6.85 Å, 8.80 Å and 7.75 Å, respectively [25]. In [28] the size of ULK pores are stated in between 8.1 Å and 11.8 Å.

## 2. Theoretical Background

would be able to not only repair the damage to the k-value on the surface but also in the deeper layers without compression of the ULK material.

Such a fourth method is currently developed at the Fraunhofer ENAS. The idea is to fragment the silylation molecules to obtain smaller plasma fragments. Like the  $\text{CH}_4$  plasma, they are able to diffuse into the pores while still retaining the silylation molecules' ability to repair the k-value. This method is called plasma repair. However, this method also has its disadvantages, which together with the advantages and disadvantages of the other methods are summarized in table 2.1.

Method	Advantage	Disadvantage
<b>UV Assisted Thermal Curing</b>	<ul style="list-style-type: none"> <li>removal of silanol groups and water</li> </ul>	<ul style="list-style-type: none"> <li>compression of the material</li> <li>no reintegration of lost methyl groups</li> </ul>
<b>Hydrocarbon Plasma</b>	<ul style="list-style-type: none"> <li>small fragments can penetrate deeply into the damaged material</li> </ul>	<ul style="list-style-type: none"> <li>builds a carbon rich layer on the surface</li> <li>no reactions between the methyl fragments and the damaged ULK material</li> </ul>
<b>Silylation</b>	<ul style="list-style-type: none"> <li>restores the k-value by replacing silanol groups with less polar groups</li> <li>repair process can be easily integrated into existing manufacturing process</li> </ul>	<ul style="list-style-type: none"> <li>large molecules allow only a k-restore at the surface</li> </ul>
<b>Plasma Repair</b>	<ul style="list-style-type: none"> <li>small fragments can penetrate deeply into the damaged material</li> <li>restores the k-value by replacing silanol groups with less polar groups</li> <li>repair process can be easily integrated into existing manufacturing process</li> <li>able to repair H-damage</li> </ul>	<ul style="list-style-type: none"> <li>process parameters for the best repair effect unknown</li> <li>some repair fragments are prone to new H-/OH-damages</li> <li>the repair plasma can contain radicals that damage the ULK material</li> </ul>

Table 2.1.: (Dis-)advantages of different k-restore methods

Since the plasma repair process is still in the development phase, there are many open questions to be answered. One question is how the fragments from the silylation molecules are constituted. As they are plasma fragments, they are open shell radicals that also satisfy the following demands: being as small as possible and being able to restore the k-value. The first demand is met with the fragments only consisting of one silicon atom (see figure 2.4). Additionally, they must possess at least one methyl group to restore the k-value. If it is desired that the repair fragments are also able to cure H-damages in addition to OH-damages, then the fragments must further possess at least one oxygen atom. This leads to repair fragments whose empirical formula is  $\text{SiO}_y(\text{CH}_3)_x$ , with  $y = \{0; 1; 2\}$  and  $x \in \{1; 2; 3\}$ . Figure 2.4 shows nine possible repair fragments and their assumed repair behavior.

There are two major conclusions which can be drawn from figure 2.4. The first observation is that while the repair fragments  $\text{SiO}_y\text{CH}_3$  are able to repair two defective sites, they themselves are prone to H- and OH-damage. However, as they cure two defective sites and only introduce one new defect, a repair effect can still be attributed to them. The second conclusion which can be taken from figure 2.4 is that the  $\text{SiO}_y(\text{CH}_3)_3$  fragments are limited to repair only one damaged site. Thus, the fragment group  $\text{SiO}_y(\text{CH}_3)_2$  seems to be preferable.

The experimental work of Köhler [10] showed that a repair effect can be achieved with the plasma repair method. While in the experiment a variation of parameters were studied. Also, the preferred fragments were analyzed with mass spectroscopy which shows a further fragmented

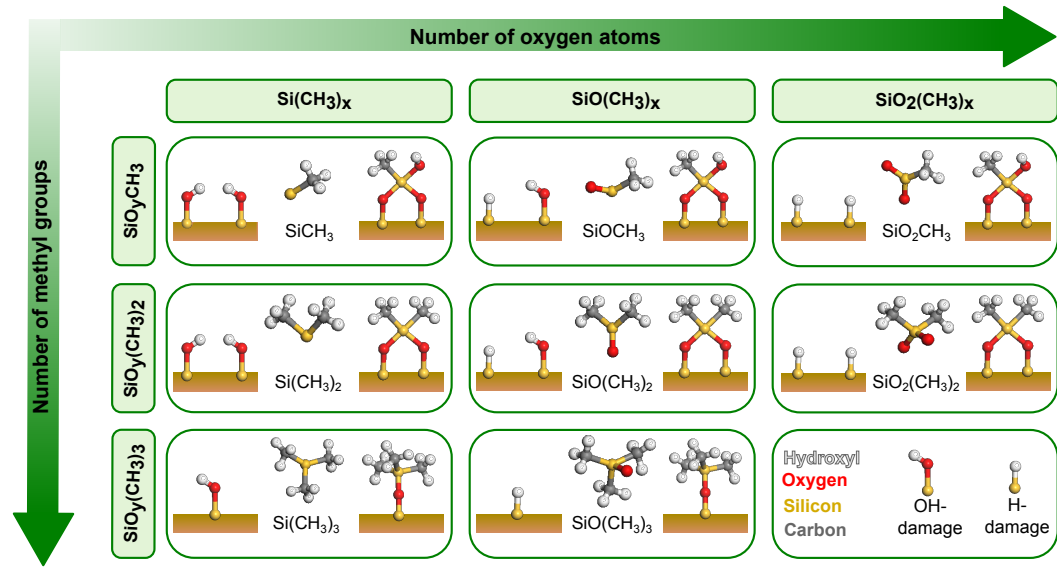


Figure 2.4.: Overview of possible plasma repair fragments and their assumed repair behavior.

spectrum of the plasma condition. However, the reaction mechanisms itself could not be determined. Therefore, the task of this thesis is to give new insights into the plasma repair process. The focus will be placed on the possible repair fragments which can be obtained from the silylation molecules, as well as their repair reactions. These topics will be investigated in detail in chapters 4.2 and 5, respectively.

## 2.2. Reaction Theory

### 2.2.1. Reaction Process

During chemical reactions, a rearrangement of atoms and bonds takes place (see figure 2.5). In their pre-reaction state the chemicals are called educts, whereas in their post-reaction geometry they are named products. Both products and educts are in their ground state. This means, that they are local minima of the energy landscape and thus they are free of internal forces. For small geometrical disturbances, the structure will relax towards the product or educt geometry.

Further, during the chemical reaction, a complex is formed between the involved educts. This complex is referred to as the transition state (TS) as the complex can transform to either the products or the educts. In case of an irreversible reaction, from the transition state only the products can be formed. In the energy landscape, the TS is a first order saddle point.

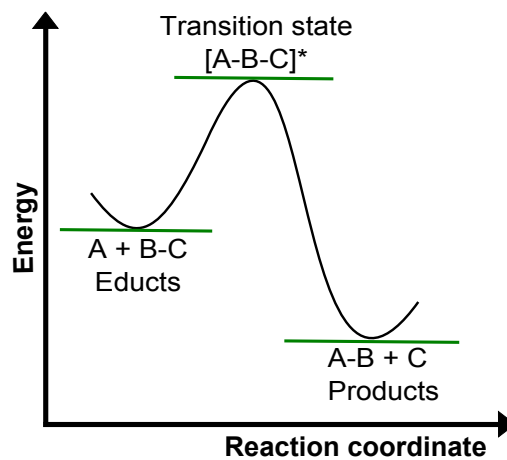


Figure 2.5.: Reaction process. The educts A and B-C react to the products A-B and C. At the transition state the complex  $[A\_B\_C]^*$  is formed.

The energy differences during the various states of the reaction are of interest. For example, the reaction energy  $E_R$  determines whether the reaction releases energy or if energy is adsorbed. The reaction energy  $E_R$  is defined as the difference between the sum of the products' energy and the sum of the educts' energy:

$$E_R = \sum_i E_{Products} - \sum_i E_{Educts} \quad (2.1)$$

If  $E_R < 0$ , then the reaction is exothermic, and therefore energy is released. If  $E_R > 0$ , then the reaction is endothermic and external energy must be supplied to form the products.

Besides the reaction energy, there is also the activation energy  $E_A$ . This energy determines if an energy barrier must be overcome to form the complex that will lead to the products. Thus, the activation energy is defined as:

$$E_A = \sum_i E_{TS} - \sum_i E_{Educts} \quad (2.2)$$

If  $E_A < 0$ , then the reaction is barrier free<sup>5</sup> and will happen spontaneously. Otherwise energy is needed to overcome the activation barrier. Figure 2.6 summarizes the above mentioned possibilities.

<sup>5</sup>In the case of a barrier free reaction, the TS is actually an intermediate state. For convenience, it will be labeled as a TS in the scope of this thesis.

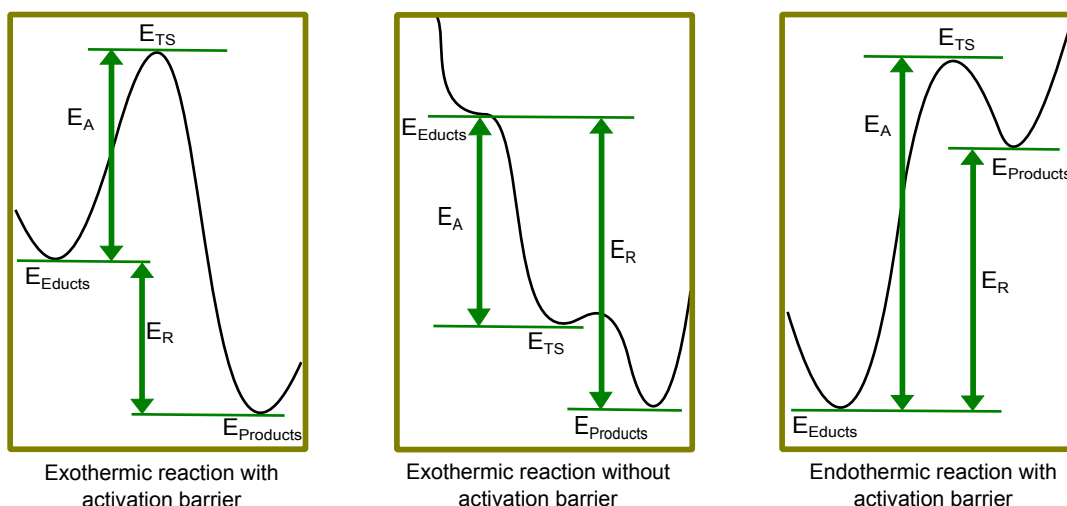


Figure 2.6.: Overview of reaction processes

### 2.2.2. Thermal Influence

In quantum chemical calculations, the energies are computed at 0 K. To obtain the reaction and activation energies at temperatures  $T$  above 0 K, thermal correction terms for the enthalpy  $H$  and the entropy  $S$  need to be added. Here, the enthalpy  $H$  includes the additional energies by the excitation of atoms because of vibrational ( $E_{\text{vib}}$ ) and rotational ( $E_{\text{rot}}$ ) degrees of freedom, as well as from translational ( $E_{\text{trans}}$ ) movements at finite temperatures. Therefore, the correction term  $H(T)$  is defined as:

$$H(T) = E_{\text{vib}}(T) + E_{\text{rot}}(T) + E_{\text{trans}}(T) + RT, \quad (2.3)$$

$R$  being the ideal gas constant.

The entropy  $S$  takes the energy the systems gains due to its disorder into account. Analogous to  $H(T)$ , the entropy correction  $S(T)$  has vibrational ( $S_{\text{vib}}$ ), rotational ( $S_{\text{rot}}$ ) and translational ( $S_{\text{trans}}$ ) contributions:

$$S(T) = S_{\text{vib}}(T) + S_{\text{rot}}(T) + S_{\text{trans}}(T) \quad (2.4)$$

Together, the entropy correction  $S(T)$  and the enthalpy correction  $H(T)$  lead to the Gibbs free energy correction  $G(T)$ , which is defined as:

$$G(T) = H(T) - TS(T) \quad (2.5)$$

Usually, the entropy correction  $S(T)$  multiplied with  $T$  is one magnitude below the enthalpy correction  $H(T)$ <sup>6</sup>.  $G(T)$  is directly proportional to  $T$  for temperatures above 0 K.

The energy  $E(T)$  of a molecule is defined as:

$$E(T) = E(T = 0) + G(T) \quad (2.6)$$

For  $T = 0$  K there is a jump in the  $E(T)$ -curve (see figure 2.7). This is due to the zero-point vibrational energy<sup>7</sup> (ZPVE), which contributes to  $E_{\text{vib}}(T)$  in equation 2.3 and is by convention not included when energies are given for  $T = 0$  K. “Even for a small molecule, the total ZPVE can

<sup>6</sup>For example the thermal correction values for OMCTS at room temperature are 213 kcal/mol for the enthalpy  $H$  and -47 kcal/mol for the entropy  $S$ .

<sup>7</sup>This is, as the name implies, the vibrational energy a molecule possesses at 0 K.

## 2. Theoretical Background

amount to several tens of kcal/mol” [29], thus a jump in the  $E(T)$ -curve occurs when the Gibbs free energy correction is added for the first time.

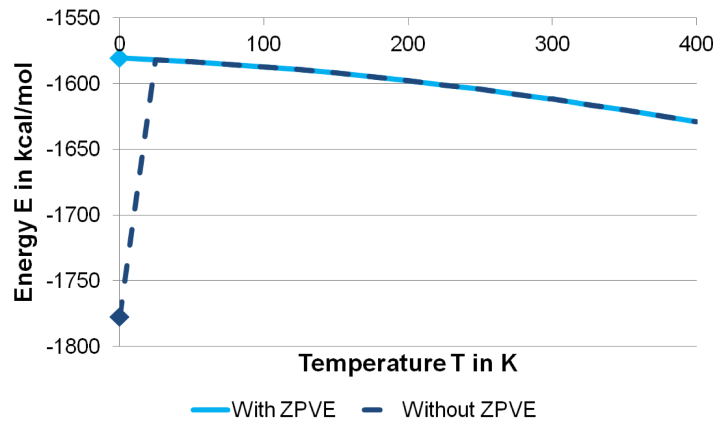


Figure 2.7.: Exemplary entropy correction for OMCTS. The entropy correction  $G(T)$  was first added for  $T = 25$  K. The light blue line shows  $E(T)$ , when the ZPVE is added for  $T = 0$  K. The dark blue, dotted line shows  $E(T)$  when the ZPVE is not added for  $T = 0$  K. In case of OMCTS, the ZPVE has a value of 197 kcal/mol.

Analogous to the energy the Gibbs free energy correction terms  $\Delta G_R(T)$  and  $\Delta G_A(T)$  for the reaction and activation energies are calculated as defined in equation 2.7.

$$\begin{aligned}\Delta G_R(T) &= \sum_i G_{Products}(T) - \sum_i G_{Educts}(T) \\ \Delta G_A(T) &= \sum_i G_{TS}(T) - \sum_i G_{Educts}(T)\end{aligned}\tag{2.7}$$

This leads to the reaction energy  $E_R$  and the activation energy  $E_A$  at the temperature  $T > 0$  being defined as:

$$\begin{aligned}E_R(T) &= E_R(T=0) + \Delta G_R(T) \\ E_A(T) &= E_A(T=0) + \Delta G_A(T)\end{aligned}\tag{2.8}$$

In a temperature-energy diagram, the reaction and activation energies will display a linear behavior with a jump at the temperature at which the Gibbs free energy correction terms is added for the first time. This is due to the above-mentioned neglect of the ZPVE for  $T = 0$  K in the Gibbs free energy correction  $G(T)$ .

## 3. Computational Methods

### 3.1. Overview

Today there are many different computational methods in use, each with their own (dis-)advantages. The available range of methods starts with molecular mechanics (MM) with classical empirical potentials, which yield total energies and geometries. Depending on their implementation Kinetic Monte Carlo (KMC) and molecular dynamics (MD) simulations can offer the calculation of additional thermodynamic properties such as pressure. And with quantum based methods such as Hartree-Fock (HF) and post-HF methods or density functional theory (DFT) properties like frequencies, UV spectra and electron distributions can be calculated [30].

Analogous to the methods including different calculable properties, different methods are used for certain system sizes. For example, DFT is used for molecules and small clusters with up to 300 atoms. To investigate reactions inside a reactor, programs based on computational fluid dynamics (CFD) are necessary.

The decision for or against the use of a certain method is primarily defined by the required level of accuracy and information one wants to reach, the size of the investigated system as well as the time frame. Figure 3.1 gives an overview of the above mentioned methods in relation to the system size and time frame and also lists the main concept behind the methods.

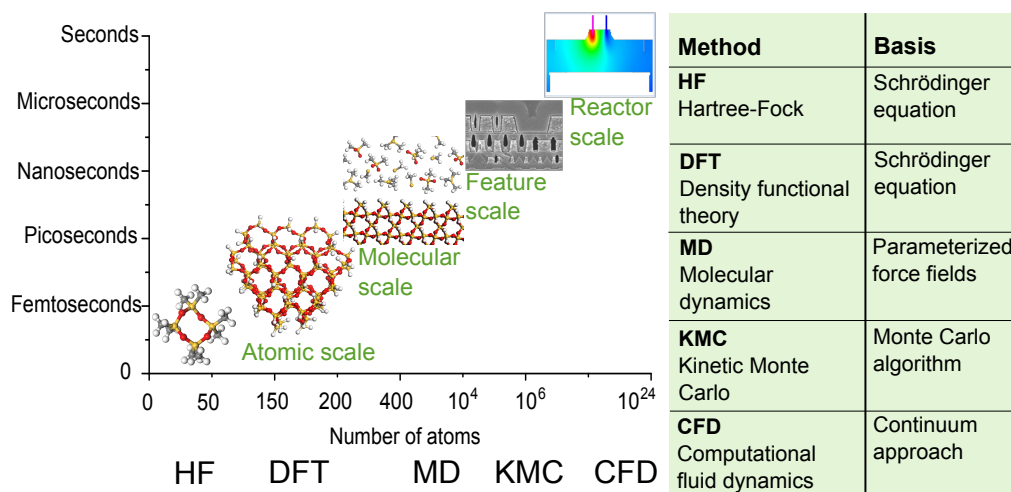


Figure 3.1.: Overview of computational methods

This study about the repair of damaged ULK materials deals with systems consisting of nine atoms up to systems with slightly over three hundred atoms. Therefore, according to figure 3.1 HF, DFT and MD are the best suited methods for this study. Since post-HF methods are superior to HF, only post-HF methods and MD methods will be considered.

As mentioned in figure 3.1, MD methods are based on parametrized force fields. Out of the available MD force fields, not every field contains all the necessary parameters for this study. This is either because atoms are completely missing in parameter sets or selected atom-atom interaction parameters are not included in the force field. Force fields which include (nearly) all necessary

### 3. Computational Methods

parameters needed for this study are the one developed by Brenner [31], the Dreiding force field [32] or the ReaxFF<sup>8</sup> [33] force fields. The ReaxFF parametrization is superior to Brenner or Dreiding [33] because ReaxFF takes into account all important atomic interactions, whereas in the other two force fields some interactions are not considered. Thus, ReaxFF is the MD force field which will be used in this thesis and described in more detail in chapter 3.3.

From the wide array of available post-HF methods, the most prominent ones are Møller–Plesset perturbation theory of the order  $x$  (MP $x$ ), the coupled cluster (CC) approach with different excitations and density functional theory (DFT). The decision for one of these post-HF method is based on the required accuracy of the calculations, as well as their scaling behavior which is illustrated in figure 3.2. Considering that the systems which will be investigated consist of up to three hundred atoms, only DFT with a scaling behavior of  $\sim N^3$  will be applicable in a reasonable calculation time with accurate energies. Therefore, DFT is the method of choice for this thesis and will be described in the following sub-chapter.

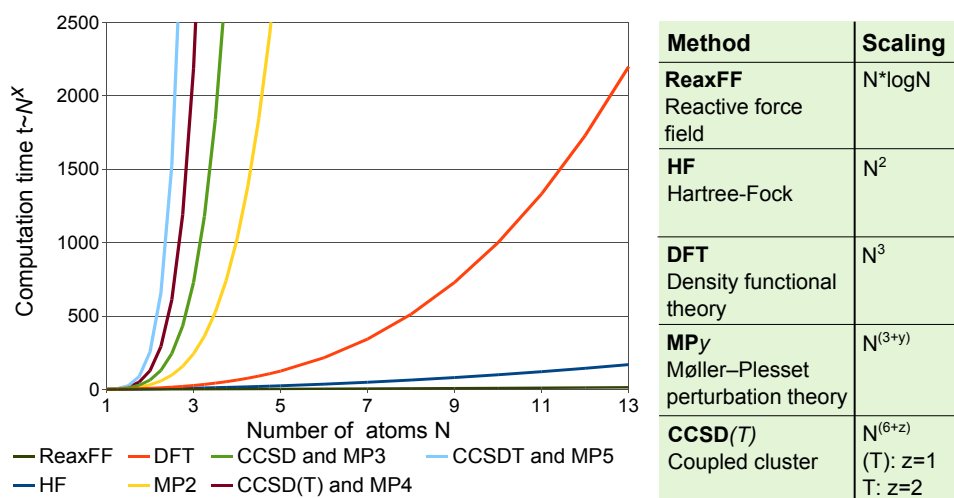


Figure 3.2.: Scaling of HF, ReaxFF and post-HF methods

## 3.2. Density Functional Theory

### 3.2.1. Theoretical Background

The following two sub-chapters on the theoretical background of the density functional theory (DFT) are based on chapter three in the previous bachelor thesis<sup>9</sup> [35]. The third sub-chapter is based on [34].

#### 3.2.1.1. The Schrödinger Equation and the Variational Principle

The basis of density functional theory (DFT) is the time-independent, non-relativistic Schrödinger equation (eq. 3.1) which states that the product of the wave function  $\Psi$  with the energy  $E$  of the system equals the Hamilton operator  $\hat{H}$  employed on the same wave function  $\Psi$ .

<sup>8</sup>Short for Reactive Force Field.

<sup>9</sup>Wolfram Koch and Max. C. Holthausen's book "A Chemist's Guide to Density Functional Theory"[34] was used as the basis for the chapter on DFT in [35].



$$\hat{H}\Psi = E\Psi \quad (3.1)$$

The Hamilton operator  $\hat{H}$  (eq. 3.2) for a system with  $N$  electrons (indices  $i, j$ ) and  $M$  nuclei (indices  $A, B$ ) consists of five terms:

$$\hat{H} = -\frac{1}{2} \sum_{i=1}^N \nabla_i^2 - \frac{1}{2} \sum_{A=1}^M \frac{1}{M_A} \nabla_A^2 - \sum_{i=1}^N \sum_{A=1}^M \frac{Z_A}{r_{iA}} + \sum_{i=1}^N \sum_{j>i}^N \frac{1}{r_{ij}} + \sum_{A=1}^M \sum_{B>A}^M \frac{Z_A Z_B}{r_{AB}} \quad (3.2)$$

The first two terms represent the kinetic energy of the electrons and nuclei, respectively. The remaining three terms contribute the potential energy of the system in the following order: electron-nucleus, electron-electron and nucleus-nucleus interaction. According to the used indices  $r_{xy}$  represents the distance between electron-electron, electron-nucleus or nucleus-nucleus,  $Z_M$  the charge of the nuclei and  $M_A$  the mass of the nuclei.

While the Schrödinger equation gives the exact energy, solving the equation for systems with more than one electron is complicated, if not impossible. Therefore, one needs to simplify the problem with the smallest possible lost of accuracy. The simplest way to achieve this is to use the Born-Oppenheimer approximation. Here, the large difference between the masses of electrons and nuclei by a factor of 1836 is taken advantage of by regarding the nuclei as static in comparison to the electrons. This yields the kinetic energy of the nuclei becoming zero, while the potential energy term for the nucleus-nucleus repulsion becomes a constant (equation 3.3).

$$E_{nuc} = \hat{V}_{nn} = \sum_{A=1}^M \sum_{B>A}^M \frac{Z_A Z_B}{r_{AB}} = \text{const.} \quad (3.3)$$

Therefore, the energy  $E_{tot}$  of the system can be described as:

$$E_{tot} = E_{elec} + E_{nuc} \quad (3.4)$$

The electronic energy  $E_{elec}$  can be gained by solving the electronic Schrödinger equation (eq. 3.5) with  $\hat{H}_{elec}$  being the electronic Hamilton operator (eq. 3.6).

$$\hat{H}_{elec} \Psi_{elec} = E_{elec} \Psi_{elec} \quad (3.5)$$

$$\hat{H}_{elec} = -\frac{1}{2} \sum_{i=1}^N \nabla_i^2 - \sum_{i=1}^N \sum_{A=1}^M \frac{Z_A}{r_{iA}} + \sum_{i=1}^N \sum_{j>i}^N \frac{1}{r_{ij}} = \hat{T}_e + \hat{V}_{en} + \hat{V}_{ee}, \quad (3.6)$$

Even with this approximation, solving equation 3.5 for systems with more than one electron is analytically still not possible. However, equation 3.5 simplifies to numerically gain the ground state energy  $E_0$  for more-electrons systems. For this, equation 3.7 must be solved, where  $E_0$  is the expectation value of the Hamilton operator and  $\Psi_0$  the wave function of the ground state.

$$\langle \Psi_0 | \hat{H} | \Psi_0 \rangle = E_0 \quad (3.7)$$

However, in practice,  $\Psi_0$  is unknown and instead only an approximated wave function  $\Psi_b$  is available. To still get closed to the ground state the Variational Principle (equation 3.8) is employed. It states that all energies  $E_b$  which are gained by solving equation 3.7 with an approximated wave function  $\Psi_b$  are greater than or equal to the real ground state energy  $E_0$ .

$$\langle \Psi_b | \hat{H} | \Psi_b \rangle = E_b \geq E_0 \quad (3.8)$$

Therefore,  $E_b$  needs to be minimized.

### 3. Computational Methods

#### 3.2.1.2. From the Electron Density to the Kohn-Sham Approach

The singularity of density functional theory is that instead of the wave function  $\Psi$ , the electron density  $\rho$  is used to calculate  $E$ . Hereby, the electron density for a system with  $N$  electrons is defined as:

$$\rho(\vec{r}) = N \int \dots \int |\Psi(\vec{x}_1, \vec{x}_2, \dots, \vec{x}_i, \dots, \vec{x}_j, \dots, \vec{x}_N)|^2 ds_1 d\vec{x}_2 \dots d\vec{x}_N, \quad (3.9)$$

where  $\Psi$  is integrated for  $N - 1$  electrons over all electron coordinates<sup>10</sup>  $\vec{x}_i$  and only over the spin coordinate  $s_1$  for the remaining electron. Therefore,  $\rho$  can be describes as the probability to find one electron in the volume element  $d\vec{r}_1$  while all other spatial and spin states can be freely assigned as defined by  $\Psi$ .

“Furthermore, the electron density fulfills the following two properties:  $\rho(\vec{r} \rightarrow \infty) = 0$  and  $\int \rho(\vec{r}) d\vec{r}_1 = N$ . This means that the possibility to find an electron infinitely afar from the nucleus is zero and that the density integrated over the whole space results in the overall number of electrons” [35].

The foundation to use the electron density for chemical calculations as it is known today under DFT was laid by Hohenberg and Kohn in 1964 when they publicized their two theorems [36]. The first of the Hohenberg-Kohn theorems states that each electron density  $\rho$  leads to its unique Hamilton operator  $\hat{H}$ . This is proven with the reductio ad absurdum method<sup>11</sup>.

The second Hohenberg-Kohn theorem guaranties that that only the ground state density  $\rho_0$  will yield the ground state energy  $E_0$ . This is proven by utilizing the variational principle in analogy to its use in equation 3.8. Here,  $\psi_b$  is exchanged for a trial density  $\tilde{\rho}$ . This trial density  $\tilde{\rho}$  consequently defines  $\tilde{\Psi}$  and its own  $\tilde{H}$ . The so gained  $\tilde{\Psi}$  is used with the real ground state Hamilton operator  $\hat{H}$ , which leads to the following equation<sup>12</sup>:

$$\langle \Psi_0 | \hat{H} | \Psi_0 \rangle = E_0[\rho_0] \leq E[\tilde{\rho}] = T[\tilde{\rho}] + V_{ee}[\tilde{\rho}] + \int \tilde{\rho}(\vec{r}) V_{ext} d\vec{r} = \langle \tilde{\Psi} | \hat{H} | \tilde{\Psi} \rangle \quad (3.10)$$

Since the electron density of the ground state  $\rho_0$  defines  $\hat{H}$ , it in turn also defines  $E_0$ :

$$E_0[\rho_0] = T[\rho_0] + E_{ee}[\rho_0] + E_{ne}[\rho_0] \quad (3.11)$$

From equation 3.11 the energy of the electron-nuclei interaction  $E_{ne}$  is known and defined as  $E_{ne} = \int \rho_0(\vec{r}) V_{ne} d\vec{r}$ . The remaining two terms are summarized as the Hohenberg-Kohn functional  $F_{HK}$ :

$$F_{HK}[\rho_0] = T[\rho_0] + E_{ee}[\rho_0] = \langle \Psi | \hat{T} + \hat{V}_{ee} | \Psi \rangle \quad (3.12)$$

with  $E_{ee}[\rho_0] = J[\rho_0] + E_{ncl}[\rho_0]$  and  $J[\rho_0] = \frac{1}{2} \int \int \frac{\rho(\vec{r}_1)\rho(\vec{r}_2)}{r_{12}} d\vec{r}_1 d\vec{r}_2$

Here, only the the classical Coulomb interaction part  $J[\rho_0]$  of  $E_{ee}[\rho_0]$  is known. If the definitions for the kinetic energy  $T[\rho]$ , as well as for the non-classical electron-electron interaction  $E_{ncl}[\rho]$  were known, then the Schrödinger equation could be solved exactly.

In a non-interacting reference system, built of one-electron functionals  $\phi_i$ , the exact kinetic energy can be calculated. Therefore, to get closer to the exact solution of the Schrödinger equation, Kohn and Sham proposed to divide  $T[\rho]$  [37]. This way  $T[\rho]$  consists of the exact kinetic energy

<sup>10</sup>The sum of the spatial ( $\vec{r}_i$ ) and spin coordinates ( $s_i$ ).

<sup>11</sup>For details see [35], chapter 3.3.1.

<sup>12</sup>This paragraph is partially cited from [35].

of the reference system  $T_s[\rho]$  and the difference  $T_C[\rho]$  between the kinetic energy of the reference system to the real system (see equation 3.13) .

$$T[\rho] = T_s[\rho] + T_C[\rho] = -\frac{1}{2} \sum_i^N \langle \phi_i | \nabla^2 | \phi_i \rangle + T_C[\rho] \quad (3.13)$$

With this equation 3.12 can be written as:

$$\begin{aligned} F_{HK}[\rho_0] &= T_s[\rho_0] + J[\rho_0] + E_{XC}[\rho_0] \\ \text{with } E_{XC}[\rho_0] &= T_C[\rho_0] + E_{ncl}[\rho_0] \end{aligned} \quad (3.14)$$

This leaves the exchange-correlation energy  $E_{XC}$  as the only unknown term. Therefore, the quality of a result depends on how well the exchange-correlation functional is defined [38].

### 3.2.1.3. Exchange-Correlation Functionals and Basis Sets

The current exchange-correlation functionals can be divided into three main categories: local-density approximation (LDA), generalized gradient approximations (GGA) and hybrid functionals. The latter two functionals are advancement of the first, thus LDA has the simplest expression for the exchange-correlation energy  $E_{XC}$ :

$$E_{XC}^{LDA}[\rho] = \int \rho(\vec{r}) \epsilon_{XC}(\rho(\vec{r})) d\vec{r} \quad (3.15)$$

Here a hypothetical uniform electron gas is used as the basis, with  $\epsilon_{XC}$  being the exchange-correlation energy per particle of the electron gas. It can be further expanded to unrestricted systems with the spins  $\alpha, \beta$  and their densities  $\rho_\alpha$  and  $\rho_\beta$ , leading to the local spin-density approximation (LSD), defined as;

$$E_{XC}^{LSD}[\rho_\alpha, \rho_\beta] = \int \rho(\vec{r}) \epsilon_{XC}(\rho_\alpha(\vec{r}), \rho_\beta(\vec{r})) d\vec{r} \quad (3.16)$$

The GGA improves the LDA by also taking the gradient of the density  $\nabla \rho(\vec{r})$  into account. The exchange-correlation energy  $E_{XC}$  is then expressed as:

$$E_{XC}^{GGA}[\rho_\alpha, \rho_\beta] = \int f(\rho_\alpha, \rho_\beta, \nabla \rho_\alpha, \nabla \rho_\beta) d\vec{r} \quad (3.17)$$

How the function  $f$  is defined depends on the concrete GGA functional one chooses.

The hybrid functionals are, as the name suggests, a mix of different exchange-correlation functionals. The main idea is to split  $E_{XC}$  according to the coupling strength parameter  $\lambda$ . For  $\lambda = 0$  the exact term is known and for  $\lambda = 1$  a GGA functional is used. In real systems  $\lambda$  is less than one, but greater than zero. Therefore, in a hybrid functional there is a parametrization between the  $\lambda = 0$  and  $\lambda = 1$  contributions. For example the exchange-correlation energy  $E_{XC}$  for B3LYP is defined as:

$$E_{XC}^{B3LYP} = (1-a)E_X^{LSD} + aE_X^{\lambda=0} + bE_X^{B88} + cE_C^{LYP} + (1-c)E_C^{LSD} \quad (3.18)$$

As the exchange-correlation functional is the only approximation brought into DFT one should take caution when choosing a functional.

Another aspect which has a non-negligible influence on the accuracy of the calculations is the basis set. This basis set  $\{\eta_\mu\}$  constructs the wave functions  $\Psi_i = \sum_\mu c_{i\mu} \eta_\mu$ . Because the wave functions  $\Psi_i$  is only a mean to construct the electron density  $\rho(\vec{r})$  (see equation 3.9), the basis

### 3. Computational Methods

set in DFT has a less serve effect on the final energy than for wave function based methods like Hartree-Fock [34].

One possible option for a basis set are cartesian Gaussian-type-orbitals (GTOs). As the name implies, the basis set is constructed from Gaussian functions, with:

$$\eta^{GTO} = Nx^l y^m z^n \exp[-\alpha r^2] \quad (3.19)$$

Here,  $N$  is used to normalize  $\eta_\mu$  and  $l + m + n = L$ ;  $L$  being the orbital quantum number. The advantage of GTOs is that they are easy “to handle numerically because the product of two GTOs located at different atoms is another GTO located in between” [39]. However, they are unable to reproduce the correct behavior for  $r \rightarrow \infty$  and  $r \rightarrow 0$ .

In contrast to the GTOs, the Slayter-type-orbitals (STOs) display the correct behavior for  $r \rightarrow \infty$  and  $r \rightarrow 0$ . However, they are numerically harder to handle. STOs are simple exponentials that are defined as:

$$\eta^{STO} = Nr^{n-1} \exp[-\zeta r] Y_{lm}(\Theta, \phi) \quad (3.20)$$

Here,  $n$  is the principal quantum number,  $\zeta$  the orbital exponent “and  $Y_{lm}$  are the spherical harmonics that describe the angular part of the [basis] function” [34].

To achieve the accuracy of STOs, but at the same time still have the computational advantage GTOs offer, several Gaussian functions are combined. This leads to the contracted Gaussian functions (CGF), defined as:

$$\eta_\tau^{CGF} = \sum_a^A d_{a\tau} \eta_a^{GTO} \quad (3.21)$$

Here,  $d_{a\tau}$  is the contraction coefficient, which has the task of making the CGF resemble a STO as well as possible.

An alternative to the GTOs and STOs based basis sets are numerical basis sets. Instead of exponential functions atomic-centered spherical-polar meshes are used to build  $\eta_\mu$ . The angular part is still described by  $Y_{lm}$  [40].

Independent of the kind of basis set that is used, the number of basis functions which describe one orbital determines the accuracy of the calculation. The minimal basis set only consists of exactly one basis function for each orbital. Lithium’s minimal basis set, for example, consists of five functions (1s, 2s, 2p<sub>x</sub>, 2p<sub>y</sub>, 2p<sub>z</sub>). If two basis sets are used for each orbital, then one gains double-zeta basis sets, triple-zeta for three functions per orbital, and so on. And while each additional function increases the accuracy of the calculation [41] it also increases the calculation time.

In addition to enlarging the basis set, it is possible to add polarization functions (denoted with \*) and diffuse functions (denoted with +). The first option adds the next highest orbital to an atom. For example, instead of only having one basis function for its 1s orbital, helium would also receive d orbital functions. Through this, the bonding between atoms can be simulated in a better way. Additional diffuse functions ensure that the part of the orbital that is far away from the atomic center is included by using small exponents [42].

These additional functions are often used in connection with Pople style basis sets. Here, a number  $n$  of primitive GTOs (PGTOs) are fitted to resemble STOs. These PGTOs in turn are CGFs where the coefficients  $d_{a\tau}$  are constants. The favored 6-31g Pople basis set for example has six PGTOs for the core orbitals, three PGTOs for the inner valence orbitals and one for the outer valence orbital [43]. Figure 3.3 shows an exemplary correlation between the basis set size, added polarization and diffuse functions and the calculation time.

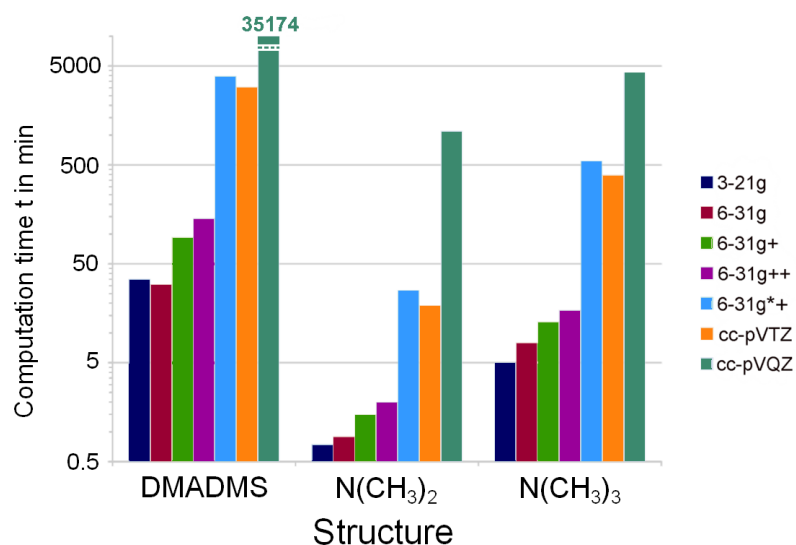


Figure 3.3.: Correlation between the basis set size and the calculation time

The exemplary calculations show that the addition of polarization functions to Pople style basis sets considerably increases the calculation time (compare 6-31g+ and 6-31g\*+ in figure 3.3). The addition of diffuse functions, on the other hand, has only a small influence on the calculation time.

The cc-pVTZ and cc-pVQZ basis sets illustrate how the addition of a further basis function to each orbital (from a triple-zeta to a quadruple-zeta basis set) increases the calculation time.

### 3. Computational Methods

#### 3.2.2. Used Program Packages

For this study two DFT program packages were employed: **Gaussian 09** [44] and **Dmol<sup>3</sup>** [45, 46] as included in Accelry's Materials Studio (Version 6.0) [47]. The reason why two different programs were used is that they either offer numerical (Dmol<sup>3</sup>) or Gaussian basis sets (Gaussian 09). This enables to study the influence the different basis sets have on the reaction energy. The detailed setups are summarized in table 3.1.

	Dmol <sup>3</sup>	Gaussian 09
Primary basis set	DNP (3.5) [45]	6-31g+ [43]
Primary functional	PBE [48]	B3LYP [49, 50, 51]
Restricted open shell/Unrestricted	Unrestricted	Unrestricted
SCF convergence	10 <sup>-6</sup>	10 <sup>-6</sup> –10 <sup>-4</sup>
Geometry convergence	10 <sup>-5</sup>	10 <sup>-5</sup> –10 <sup>-4</sup>
Smearing	thermal up to 0.008 Ha	— <sup>13</sup>
Orbital cutoff	4.6 Å	—
Corrections	Grimme DFT-D correction	—

Table 3.1.: Overview calculation details DFT

According to [52] the combination PBE/DNP in Dmol<sup>3</sup> is close to the accuracy of B3LYP/6-31g\*\*. However as the computational costs of 6-31g\*\* is too high (see figure 3.3), this basis set had to be substituted with 6-31g+, thus reducing the accuracy of the Gaussian calculations. This leads to the combinations PBE/DNP for Dmol<sup>3</sup> and B3LYP/6-31g+ for Gaussian. Due to discrepancies between Dmol<sup>3</sup> and Gaussian results, test calculations with inverted functionals<sup>14</sup> were done (see chapter 5.1.3).

The thermal smearing for Dmol<sup>3</sup> was only used when the calculation did not converge otherwise. Here, a smearing of 0.005 Ha was used at first, and if the calculation was still not converging, the value was increased to 0.008 Ha. After the optimization successfully completed, the end structure was used as the starting point for a second optimization where the smearing was disabled. However, this second optimization without smearing wasn't always successful. Therefore, some final energies were still obtained from calculation where the smearing was turned on.

The Grimme DFT-D correction was also activated due to the hydrogen atoms which play a major role in the studied reactions. The orbital cutoff value was fixed at 4.6 Å. This was necessary because H<sub>2</sub> has only a default value of 3.1 Å opposed to silicon's 4.6 Å.

Due to convergence problems with Gaussian, the SCF convergence needed to be lowered to 10<sup>-4</sup> for some calculations when using the PBE functional.

<sup>13</sup>In case of convergence problems fermi smearing was used. However, the calculations did still not converge. Thus, all Gaussian results in this work are obtained without smearing.

<sup>14</sup>Dmol<sup>3</sup> with B3LYP and Gaussian with PBE

### 3.3. ReaxFF

The following sub-chapter on the theoretical background of ReaxFF is based on [33].

#### 3.3.1. Theoretical Background

MD simulations are used when the investigated systems are too large to be studied with methods which are based on solving the Schrödinger equation. As mentioned in chapter 3.1, force fields are the basis of this method. These force fields consist of a set of parameters which include only a small assortment of atoms and limited interactions between these atoms.

An exception to this trend in MD simulation is the reactive force field (ReaxFF) suggested by van Duin et. al [33]. Because ReaxFF is a collection of different force fields, it includes a wide array of optimized parameter sets for many molecules. Each parameter set is adjusted to a specific chemical problem according to the results from DFT calculations<sup>15</sup> of smaller reference systems.

This adjustment to a specific problem makes the ReaxFF force field sensitive of even small changes in the chemical environment. To gain reliable results in a changed chemical environment, the parameters need to be re-optimized.

Instead of solving the Schrödinger equation to gain the energy  $E$ , the total energy of the system  $E_{system}$  is divided into several components (see equation 3.22) which can be calculated relatively fast. This is the reason why ReaxFF is so much faster than DFT (compare figure 3.2).

$$E_{system} = E_{bond} + E_{over} + E_{under} + E_{val} + E_{pen} + E_{tors} + E_{conj} + E_{vdWaals} + E_{Coulomb} \quad (3.22)$$

One contribution to  $E_{system}$  is the bond energy  $E_{bond}$  which depends on the bond order. Here, ReaxFF uses a corrected bond order where, amongst other, overcoordination of bonds between carbon atoms is taken into consideration. This corrected bond order distinguishes ReaxFF from other MD methods like Dreiding [32], enabling to correctly simulate bond forming and breaking.

Furthermore, an energy penalty  $E_{over}$  for overcoordinated atoms is added as well as an energy contribution  $E_{under}$  for undercoordinated atoms. Similar the energy gained through valence angles  $E_{val}$  and a penalty for “two double bounds sharing an atom in a valence angle” [33] is accounted for. Also contributions for the energy depending on the torsion angle  $E_{tor}$  and for conjugated effects  $E_{conj}$  are included. And finally the van der Waals and Coulomb interactions contribute to the total energy of the system with  $E_{vdWaals}$  and  $E_{Coulomb}$ , respectively.

For example  $E_{over}$  is defined as:

$$E_{over} = p_{over} \Delta_i \left( \frac{1}{1 + \exp(\lambda_6 \Delta_i)} \right), \quad (3.23)$$

with  $\Delta_i$  describing the coordination,  $p_{over}$  being the bond parameter and  $\lambda_6$  is the parameter which needs to be fitted according to DFT reference data. The other above mentioned energy contributions also include at least one parameter  $\lambda_i$ . The optimization of the fitting parameters  $\lambda_i$  is done as described in [53]. As an example the ReaxFF parameter set ‘Hydrocarbons’ [33] consists of altogether twenty-eight parameters  $\lambda_i$  which need to be defined. The majority coming from the valence angle energy  $E_{val}$  contribution containing eight parameters  $\lambda_i$ .

The ReaxFF parametrization for silicon and silicon oxide as defined in [54] has thirty-three  $\lambda_i$  in total. Also an additional energy term  $E_{lp}$  for the lone electrons pairs is added to the total energy  $E_{tot}$  and therefore to equation 3.22. Thus, the number of parameters  $\lambda_i$  a ReaxFF set includes depends on the particular problem the field is fitted for. The fitting procedure itself is very time consuming and would extent the scope of this thesis. Thus, for the present work already developed implementations of ReaxFF parameter sets are used.

<sup>15</sup>Often B3LYP/6-31g\*\* is used to calculate the reference DFT energies and geometries.

### 3. Computational Methods

#### 3.3.2. Used Program Packages

For this study two implementations of ReaxFF were used: **Lammps**<sup>16</sup> [55] and **Gulp**<sup>17</sup> [56]. The latter implementation is part of Accelry's Materials Studio. The main reason why they were used is that while both use ReaxFF, Gulp's ReaxFF is a mixture of different force fields [57, 58, 59, 60], designed to treat a wide array of molecules. Lammps, on the other hand, requires a specific ReaxFF parameter set as an input. This means that for Lammps already existing force fields need to be tested against DFT results for their usability in this study.

Table 3.2 summarizes the calculation details for both Lammps and Gulp, while table 3.3 gives an overview of the ReaxFF parameter sets that were employed with Lammps.

	Gulp	Lammps
Force field	ReaxFF 6.0 [57, 58, 59, 60]	different fields (see table 3.3)
Task	Geometry optimization	Dynamical calculation followed by energy minimization
Parallelization	No	Yes
Ensemble	—	NVT <sup>18</sup>
Convergence	—	for dynamical calculations: $10^{-6}$ for energy minimization: $10^{-10}$
Time step	—	0.1
Number of steps <sup>19</sup>	—	10,000

Table 3.2.: Overview calculation details ReaxFF

Name	Purpose	Published in
Newsome	Oxidation of silicon carbide by O <sub>2</sub> and H <sub>2</sub> O	[61, 62]
Kulkarni	Oxygen interactions with silica surfaces	[63]
Zhang	Carbon cluster formation during thermal decomposition of HMX <sup>20</sup> and TATB <sup>21</sup> high explosives	[64]
Nielson	Transition metal catalyzed reactions with application to carbon nanotubes	[65]
Al_AIO_AIN	Al/AIO/AIN	[66]

Table 3.3.: Overview ReaxFF parameter sets for Lammps

As no parameter set listed in 3.3 was developed for the k-restore of ULK materials via plasma repair, the results gained from these fields need to be tested against the results gained by DFT to affirm their validity for the reactions which are studied in this thesis. This is done in chapter 4.2.2.

<sup>16</sup>Short for 'Large-scale Atomic/Molecular Massively Parallel Simulation'.

<sup>17</sup>Short for 'General Utility Lattice Program'.

<sup>18</sup>N...Atom number, V...Volume, T...Temperature; all kept constant

<sup>19</sup>For dynamical calculations.

<sup>20</sup>octahydro-1,3,5,7- tetranitro-1,3,5,7-tetrazocine

<sup>21</sup>1,3,5-triamino-2,4,6-trinitrobenzene



## 4. Model System

For the investigation of the plasma repair process, it is necessary to create a model system for the OH- and H-damage, as well as to ascertain into which plasma repair fragments the silylation molecules preferably fragment.

### 4.1. Damaged ULK Materials

The obvious approach would be to study the repair reactions on a ULK surface to be as close as possible to the experimental conditions. However, such a system is too large and complex to be handled by DFT. Especially the embodiment of the pores in the ULK materials would require a very large structure model which cannot be treated with DFT in a reasonable computation time. For example a ULK material created from DEMS and hexadiene with a k-value of 2.05 has an average pore radius of 0.92 nm [28], which would require a minimum set of approximately 700 atoms.

Instead, the ULK materials will be modeled based on ULK-fragments and a silicon oxide cluster. These two model systems are able to give first insights to the repair reactions in ULK materials at reasonable computation times. Here, the ULK-fragments fulfill the task of screening the possible repair reactions. The silicon oxide cluster is used to investigate selected repair reactions and the influence of surrounding atoms on the repair process.

#### 4.1.1. ULK-Fragments

The aim of the ULK-fragments is to study a wide array of reactions with possible repair fragments. This leads to the following requirements for the ULK-fragments:

The ULK-fragments have to be as small as possible to yield fast computation times. Thus, they contain a single silicon atom. Furthermore, they have to possess at least one Si-OH or Si-H group to represent an H- or OH-damage. As they stand for defective ULK materials, a small set of ULK-fragments should be used to model silicon in differently coordinated states. The latter requirement includes additional hydrogen or oxygen atoms being bound to the silicon atom to create open and close shell systems, as well as the silicon atom sharing a single or double order bond with oxygen.

Altogether, there are six different ULK-fragments (shown in figure 4.1) used in this thesis which fulfill the above listed demands.

As one can see in figure 4.1, four out of six ULK-fragments represent both an OH- and H-damage, while the remaining two ULK-fragments only display an H-damage. Especially in the former case, where one ULK-fragment represents two different defects, it is important to clearly distinguish between an H- and OH-damage. This is achieved by keeping the features unchanged which are not directly part of the reaction.

For example if the ULK-fragment  $\text{SiH}_3\text{OH}$  represents an OH-damage, then the three hydrogen atoms bound to silicon are fixed during the geometry optimization. This leaves only the silicon atom and the hydroxyl group free to react with the repair fragments. If the ULK-fragment  $\text{SiH}_3\text{OH}$  represents an H-damage, then all but one hydrogen atoms will be fixed together with the hydroxyl group.

A special role is taken by  $\text{SiH}_2\text{OH}_2$  and  $\text{SiH}_2(\text{OH})_2$ . The latter has two hydroxyl groups, which allows studying if the repair fragments preferably repair only one or two OH-damages.  $\text{SiH}_2\text{OH}_2$ ,

#### 4. Model System

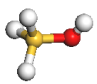
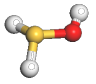
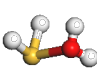
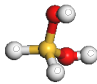
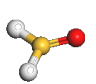
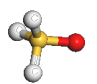
ULK-fragment						
Name	SiH <sub>3</sub> OH	SiH <sub>2</sub> OH	SiH <sub>2</sub> OH <sub>2</sub>	SiH <sub>2</sub> (OH) <sub>2</sub>	SiH <sub>2</sub> O	SiH <sub>3</sub> O
OH-damage	yes	yes	yes	yes	no	no
H-damage	yes	yes	yes	yes	yes	yes
closed/ open shell	closed shell	open shell	open shell	closed shell	closed shell	open shell

Figure 4.1.: Overview ULK-fragments

on the other hand, represents either an overcoordinated oxygen atom or it represents an absorbed water molecule inside the ULK material.

##### 4.1.2. Silicon Oxide Cluster

Silicon oxide has an empirical formula of SiO<sub>2</sub>. Its basic structure is a twelve-membered, folded ring consisting of six oxygen atoms and six silicon atoms as shown in figure 4.2. Here, each silicon/oxygen atom is part of more than one dodecagon in both the horizontal and vertical direction. The silicon atoms in a dodecagon are alternately aligned in two planes, which are the atomic planes in the corresponding silica crystal structure.

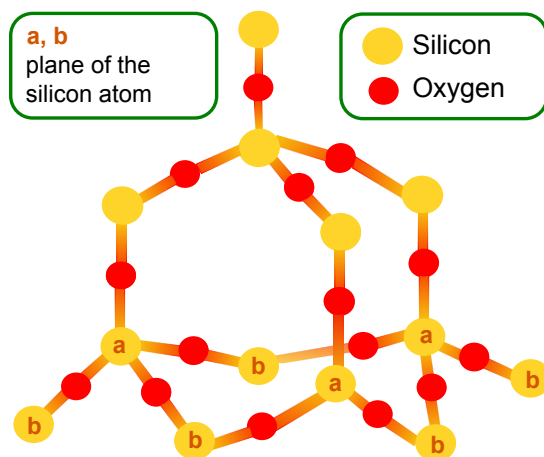


Figure 4.2.: Basic structure of the silica cluster. The only complete horizontal dodecagon in the lower half of the figure shows the alignment of the silicon atoms in two planes (planes a, b). This figure is based on [67].

It is necessary to investigate if the twelve-membered, folded ring structure influences the reaction energy, either by providing a steric hindrance or by preferring different optimized structures compared to the ULK-fragments. For this a silicon oxide cluster is created that can be handled with both DFT and MD methods.

As the calculation time is proportional to the number of atoms to the third power, it is necessary to build a silicon oxide cluster with the minimum amount of atoms. For this purpose, one silicon atom is chosen to function as the bonding partner for the hydrogen atom/hydroxyl group that

represent the H-/OH-damage<sup>22</sup>. In addition, all dodecagons which contain the defective silicon atom are also included in the cluster<sup>23</sup>. All of these atoms are free to move during the geometry optimization.

To ensure that the cluster does not deform during the repair reaction, an additional ring of dodecagons is added<sup>24</sup> to the cluster to serve as a boundary. Only the atoms in these dodecagons which are not a part of the dodecagons of the defective silicon are fixed during later geometry optimizations of the reactive cluster after a first full optimization of the cluster. Figure 4.3 summarizes the above described cluster creation.

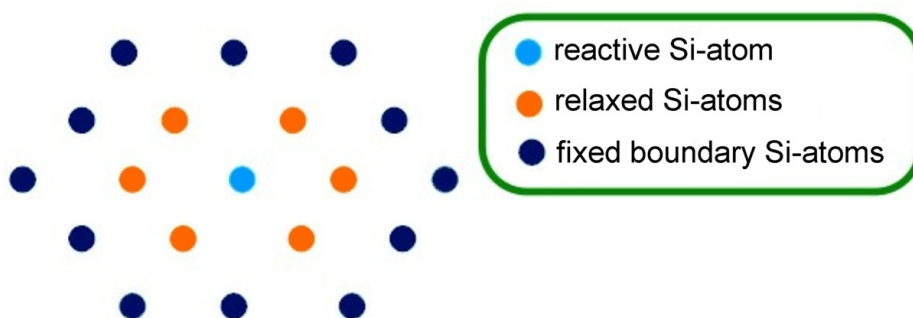


Figure 4.3.: Top view of the minimum silicon oxide cluster. Here only those silicon atoms which are in the same plane (see figure 4.2) as the reactive silicon atom with the OH-/H-damage are displayed as dots (see figure 4.4). The orange silicon atoms form either horizontal or vertical dodecagons with the light blue silicon atom. The dark blue silicon atoms in turn form dodecagons with at least one orange silicon atom.

Any dangling bonds of the cluster are saturated by hydrogen atoms. Thus, the saturating hydrogen atoms constitute about one quarter of the cluster. Together with the OH- and H-damage, this leads to an empirical formula of  $\text{Si}_{86}\text{O}_{135}\text{H}_{73}\text{-OH}$  or  $\text{Si}_{86}\text{O}_{135}\text{H}_{73}\text{-H}^{25}$ , depending on the damage the cluster represents. A picture of the cluster representing the OH-damage is shown in figure 4.4.

The hydrogenation of the silicon oxide cluster leads a silicon to oxygen ratio of  $\text{SiO}_{1.57}$  instead of  $\text{SiO}_2$ . This is due to the saturating hydrogen atoms bound to silicon atoms, substituting oxygen. While it would be possible to saturate undercoordinated oxygen atoms with hydrogen atoms to keep the silicon-oxygen ratio stable, the strongly polar bond of the hydroxyl group creates a dipole which hinders the geometry optimization. Furthermore, only six saturating hydrogen atoms are part of the reactive site of the cluster, the rest are saturating the boundary dodecagons. Therefore, the silicon-oxygen ratio around the reactive center is very close to  $\text{SiO}_2$ .

<sup>22</sup>See light blue dot in figure 4.3.

<sup>23</sup>See orange dots in figure 4.3.

<sup>24</sup>See dark blue dots in figure 4.3.

<sup>25</sup>The diameter of the orange ring in figure 4.3 equals the size of a pore in a porous ULK material. Thus, a cluster which also includes one pore would require an additional hexagonal silicon ring. This would at least double amount of atoms to construct the cluster.

#### 4. Model System

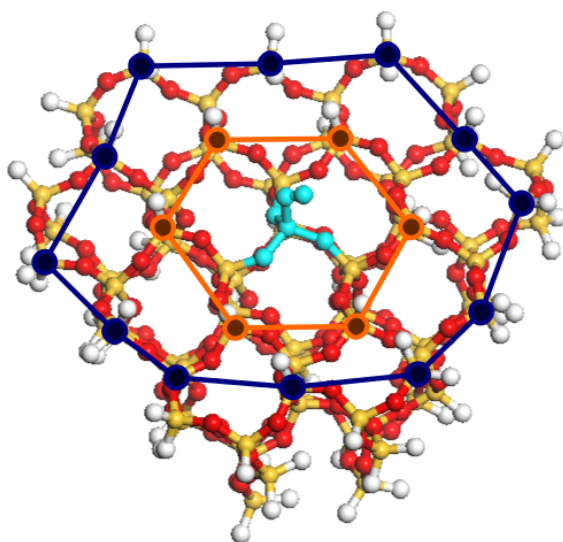


Figure 4.4.: The silicon oxide cluster. The atoms highlighted in light blue show the OH-damage region. Figure 4.3 is superimposed on the cluster to illustrate the freely optimized dodecagons (orange) and the geometrically constrained boundary dodecagons (dark blue).

## 4.2. Repair Fragments

### 4.2.1. Overview

In the previous chapter 2.1.2, eight possible repair fragments were introduced in figure 2.4. Based on unpublished experimental results from mass spectrometry of the repair plasma, two additional fragments,  $\text{Si}(\text{CH}_3)_3\text{H}$  and  $\text{SiCH}_3\text{H}_2$ , were taken into consideration. Overall, this leads to ten repair fragments which are investigated in this thesis. They are shown in figure 4.5, together with the damages they repair and their susceptibility to new defects.

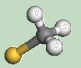
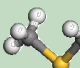
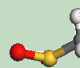
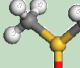
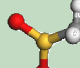
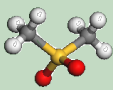
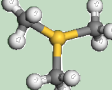
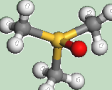
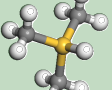
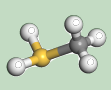
Repair-fragment					
Name	$\text{SiCH}_3$	$\text{Si}(\text{CH}_3)_2$	$\text{SiOCH}_3$	$\text{SiO}(\text{CH}_3)_2$	$\text{SiO}_2\text{CH}_3$
OH-repair	yes	yes	yes	yes	yes
H-repair	no	no	yes	yes	yes
prone to new defects	yes	no	yes	no	yes
Repair-fragment					
Name	$\text{SiO}_2(\text{CH}_3)_2$	$\text{Si}(\text{CH}_3)_3$	$\text{SiO}(\text{CH}_3)_3$	$\text{Si}(\text{CH}_3)_3\text{H}$	$\text{SiCH}_3\text{H}_2$
OH-repair	no	yes	no	yes	yes
H-repair	yes	no	yes	no	no
prone to new defects	no	no	no	no	yes

Figure 4.5.: Overview of the repair fragments. All ten investigated repair fragments together with the damages they can repair and their susceptibility to new defects are displayed.

The assumed reaction pathways of the first eight fragments were already displayed in figure 2.4. The added repair fragments  $\text{Si}(\text{CH}_3)_3\text{H}$  and  $\text{SiCH}_3\text{H}_2$ , on the other hand, are expected to behave more similar to silylation molecules because of their additional hydrogen atoms. This applies especially to the repair fragment  $\text{Si}(\text{CH}_3)_3\text{H}$  as the only closed shell repair fragment investigated. It should show a similar behavior as  $\text{Si}(\text{CH}_3)_3$  with a less exothermic reaction energy.

With the selection of the repair fragments, comes the question how they can be obtained. The major part of the chosen repair fragments can be gained by the fragmentation of silylation molecules. Others are obtained by repair fragments further reacting with methyl or methane.

The silylation molecules for the fragmentation were chosen according to their compatibility with the microelectronic industry. In particular, they should be molecules which are easy to integrate in the manufacturing process of ICs. In accordance to the experimental work in [10] and [68] DMADMS and OMCTS (see figure 4.6) are the silylation molecules whose fragmentation is studied in this thesis.

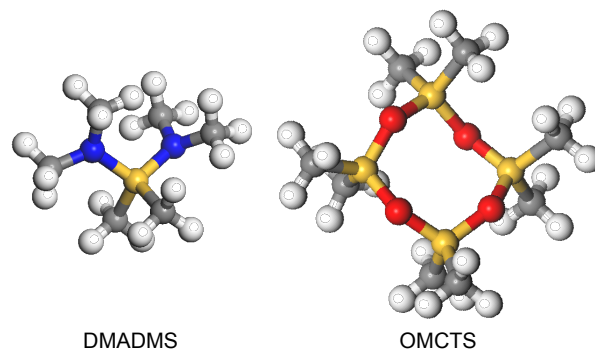


Figure 4.6.: DMADMS and OMCTS

#### 4.2.2. Fragmentation of DMADMS

DMADMS does not contain oxygen atoms, thus only repair fragments without oxygen can be obtained from this molecule. Six possible fragmentation reactions for DMADMS that seemed energetically preferable were studied. Three reactions lead to the repair fragments  $\text{Si}(\text{CH}_3)_2$  or  $\text{SiCH}_3$  together with closed shell byproducts, while the other three reactions result in open shell byproducts. The possible reactions are shown in figure 4.7 together with the reaction energies from Dmol<sup>3</sup> calculations at a temperature of 0 K. Appendix A.1.1 discusses the influence of additional thermal energy on the DMADMS fragmentation at temperatures above 0 K.

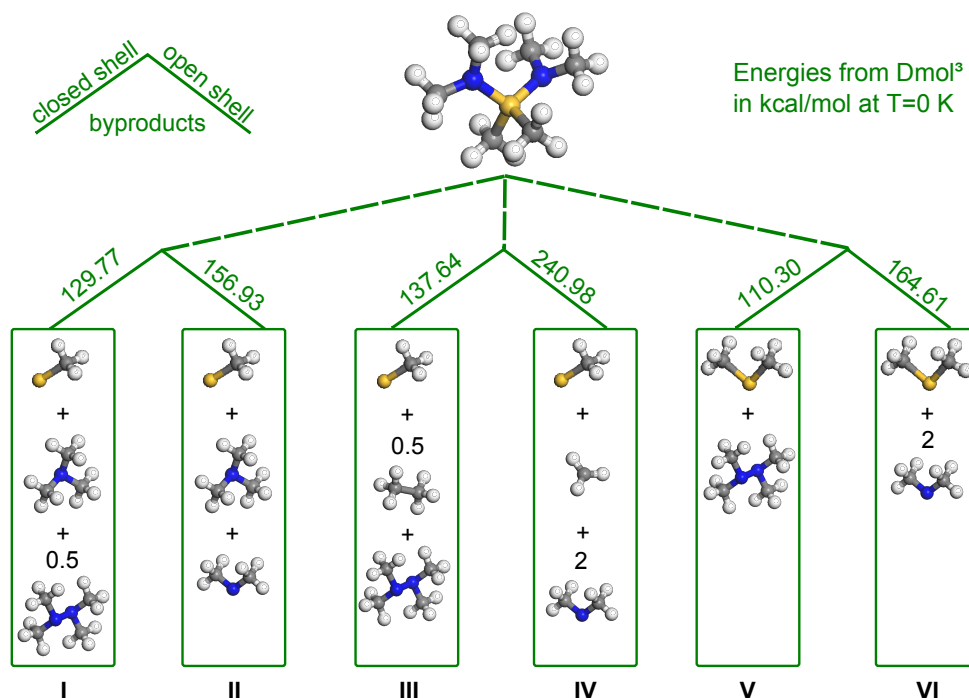


Figure 4.7.: Scheme of the DMADMS fragmentation. The reaction energies are taken from Dmol<sup>3</sup> calculations. On the left side of each bifurcation the byproducts are closed shell molecules. On the right side of the bifurcation they are split into open shell fragments.

All six reactions are connected, with every reaction having a counterpart in which the byproducts are present in their closed or open shell variation. As to be expected for such a reaction, all

fragmentation energies are endothermic. The fragmentation energies of the reactions with closed shell byproducts are lower than for the ones leading to open shell byproducts. The latter is due to the open shell state of the products, which is unfavorable as it requires additional bond breaking energies.

The favored fragmentation is reaction **V** which shows the lowest reaction energy. This is not only based on the closed shell byproducts but also on the number of products. It can be noted that the reaction energy increases with the number of products because of the additional bond breaking energies. It can be concluded that the fragmentation of DMADMS primarily leads to the repair fragment  $\text{Si}(\text{CH}_3)_2$ .

The fragmentation of DMADMS is also used to investigate the usability of the ReaxFF force fields which are available for Lammmps. All six fragmentation reactions were calculated with the force fields described in chapter 3.3.2. The results are shown in figure 4.8.

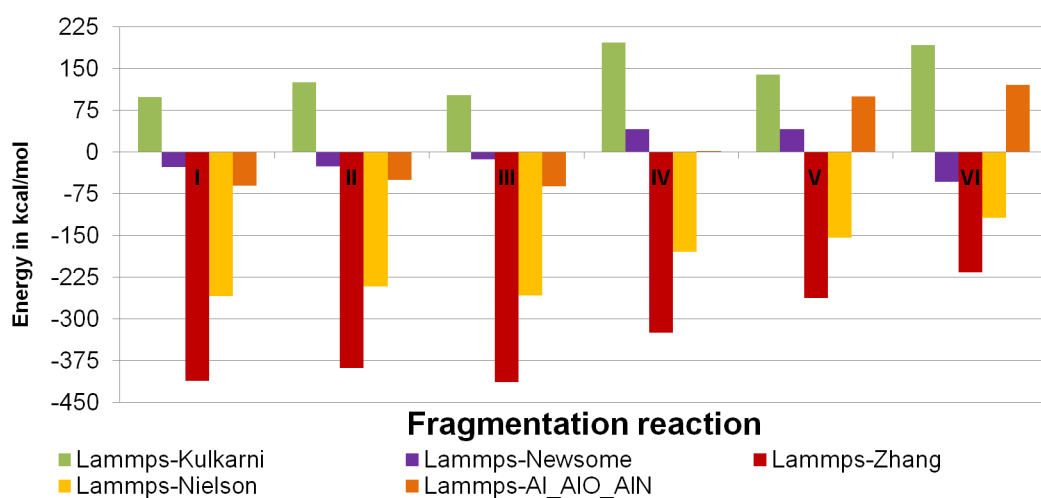


Figure 4.8.: Fragmentation of DMADMS with Lammmps. The energies for the fragmentation of DMADMS as shown in figure 4.7 are displayed.

Of all the ReaxFF force fields, only the one by Kulkarni et al. [63] always yields exothermic fragmentation energies. It is not surprising that the two force fields optimized for carbon by Nielson [65] and Zhang [64] perform poorly. While the Al\_AIO\_AIN [66] and Newsome force fields [66] both display a mediocre performance, only the latter field had been optimized for silicon containing reactions. The main conclusion, however, is that only the Kulkarni force field can be used in the scope of this thesis.

Finally, figure 4.9 displays the fragmentation energies obtained by all four approaches used for the calculation of the reaction energies. This comparison allows an implementation-independent comparison between DFT and MD. Here, one aim is to determine to what extent the MD results differ from the DFT results. This plays an important role when the model systems are too large for DFT methods and thus can only be investigated with MD.

Independent of the used program and method, fragmentation **IV** is the most unfavorable reaction. The results from both DFT programs and Gulp are in agreement that fragmentation **V** is the energetically most favorable reaction. In comparison to the DFT results, Gulp underestimates the fragmentation energies.

Lammmps with the Kulkarni force field however prefers fragmentation **I**. It is noticeable that only the reaction energies resulting in the repair fragment  $\text{Si}(\text{CH}_3)_2$  are energetically higher than the DFT results. This yields the conclusion that the energy for  $\text{Si}(\text{CH}_3)_2$  is overestimated, while the

#### 4. Model System

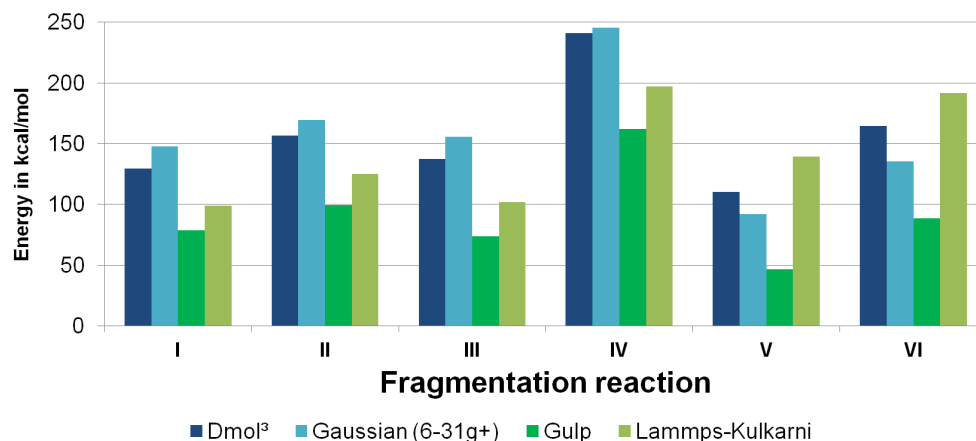


Figure 4.9.: Fragmentation of DMADMS for Dmol<sup>3</sup>, Gaussian, Gulp and Lammps.

energy for SiCH<sub>3</sub> is underestimated. This is due to the bond order dependent parametrization of the energy contributions in ReaxFF. Thus, to improve the results with the Kulkarni force field the Si-C interaction parameters need to be adjusted.

The Gaussian results were gained with the 6-31g+ basis set as the computational costs for larger basis set like cc-pVQZ or one with an additional polarization function<sup>26</sup> are too high (see figure 3.3). Appendix A.2.1 discusses in detail the impact this reduced basis set has on the reaction energy. The main conclusion is that with the 6-31g+ basis set the energy is underestimated by 15-25 kcal/mol in comparison to the extended basis sets.

In conclusion, all four approaches display different fragmentation behaviors regarding the energy of the reaction. However, they independently all favor reactions leading to close shell byproducts compared to the complementary open shell byproducts. Gulp, Gaussian and Dmol<sup>3</sup> being in agreement over the most favorable and unfavorable fragmentation.

<sup>26</sup>This leads to the basis set 6-31g+\*.



### 4.2.3. Fragmentation of OMCTS

In contrast to DMADMS, all considered repair fragments depicted in figure 2.4 can be gained by fragmenting OMCTS. There is a wide array of possible fragmentation reactions. Twelve possible fragmentation reactions that each lead to four repair fragments (and additional byproducts) are shown in figure 4.10 on page 28 and appendix A.1.2 discussed the temperature influence on the OMCTS fragmentation.

All fragmentation reactions are again endothermic. Here, reaction **VII**, which results in four  $\text{SiO}(\text{CH}_3)_2$  repair fragments, is energetically the most favored fragmentation. Also, all other fragmentations which result in at least one  $\text{SiO}(\text{CH}_3)_2$  are energetically preferable. The same applies to the repair fragments  $\text{SiO}(\text{CH}_3)_3$  and  $\text{Si}(\text{CH}_3)_3$ .

For some reactions, there seems to be a correlation between the number of products and the reaction energy. This is the most obvious for the reactions leading to six or more products as can be seen in figure 4.11.

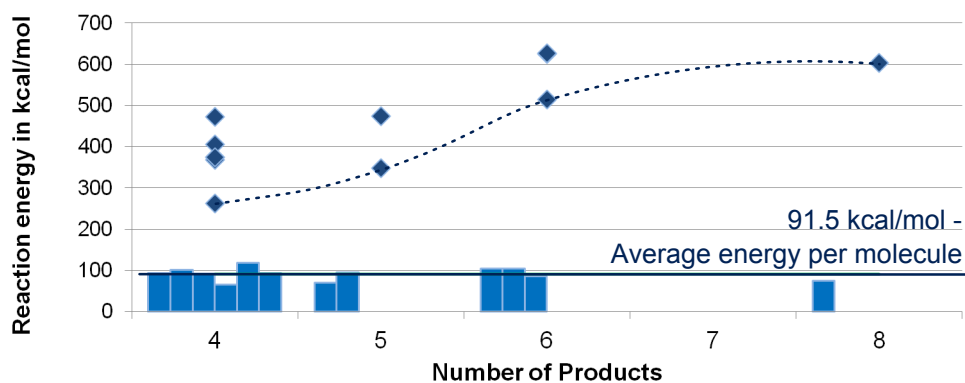


Figure 4.11.: Dependency between the number of products and the reaction energy. The dots display the overall reaction energy depending on the number of products, while the bars display the reaction energy per molecule. The dotted line is only a guide for the eyes and shows no correlations.

With every additional molecule the lowest reaction energy increases. However, if the energy per molecule is examined, then the energy is always around the average value of  $91.5 \text{ kcal/mol}^{27}$ .

Figure 4.12 shows the fragmentation reaction of OMCTS for all four methods.

The fragmentation energies obtained by the different methods differ in the same manner as for the DMADMS fragmentation. The overall reaction preference is nearly identical with all methods in favor of fragmentation **VII**. Further, the results from the different methods agree in predicting that  $\text{SiO}(\text{CH}_3)_2$ ,  $\text{SiO}(\text{CH}_3)_3$  and  $\text{Si}(\text{CH}_3)_3$  are advantageous repair fragments. There is an unexplained anomaly for reaction **VIII** regarding to the energy gained by Lammmps. This could be traced back to the oxygen molecule as oxygen is known to be problematic due to its triplet ground state.

Figure 4.13 shows the experimental results gained by mass spectroscopy as reported in [10]. There, vaporized, molecular OMCTS and vaporized OMCTS after the plasma fragmentation were investigated. It is important to know that during mass spectroscopy additional fragmentations are very probable to take place. For example, the mass spectroscopy of vaporized OMCTS only results in the detection of OMCTS fragments, opposed to the detection of OMCTS molecules. This

<sup>27</sup>The average energy per molecule of DMADMS, as studied in the previous sub-chapter, is about  $55 \text{ kcal/mol}$ .

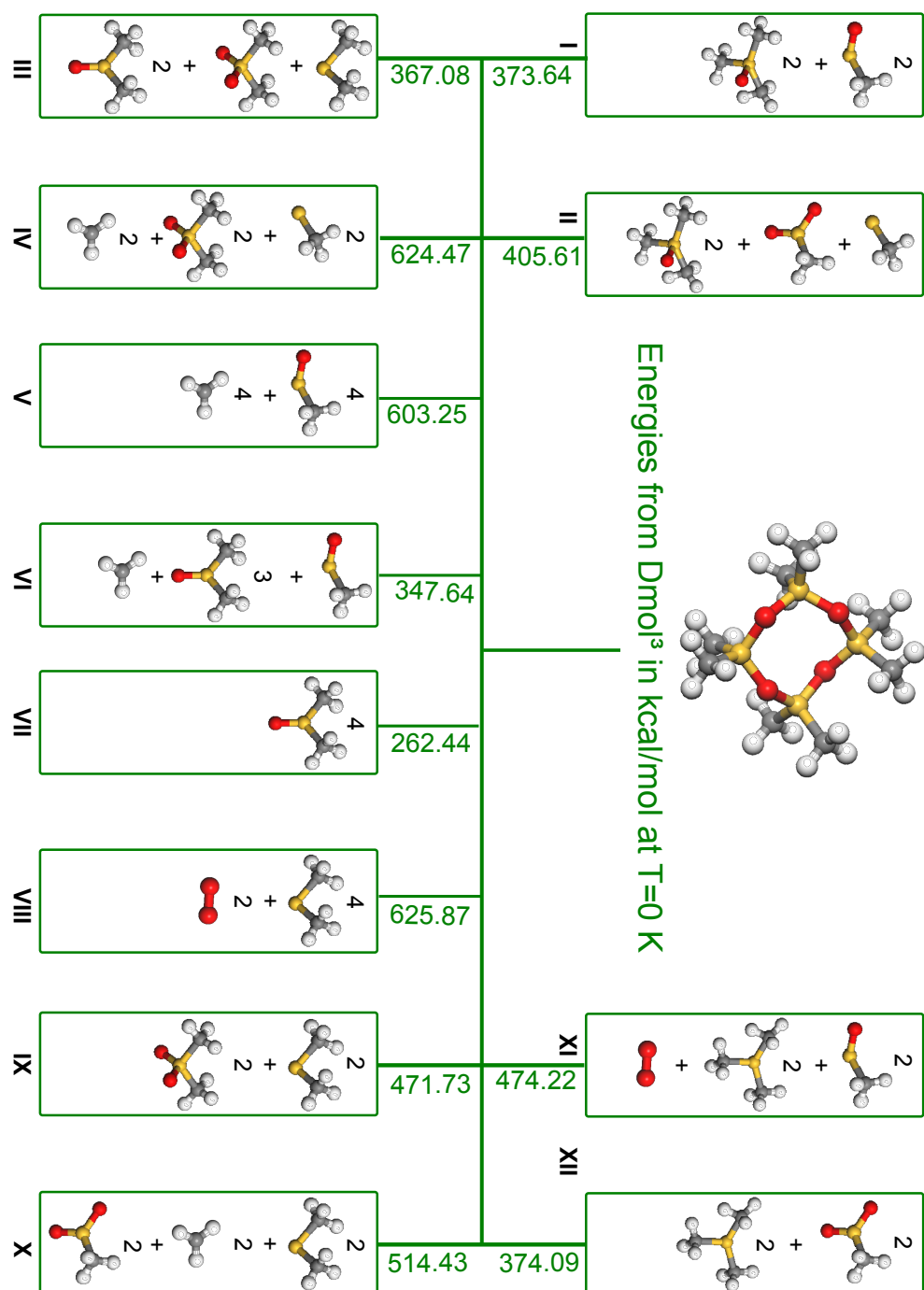


Figure 4.10.: Scheme of the OMCTS fragmentation. The reaction energies are taken from Dmol<sup>3</sup> calculations.

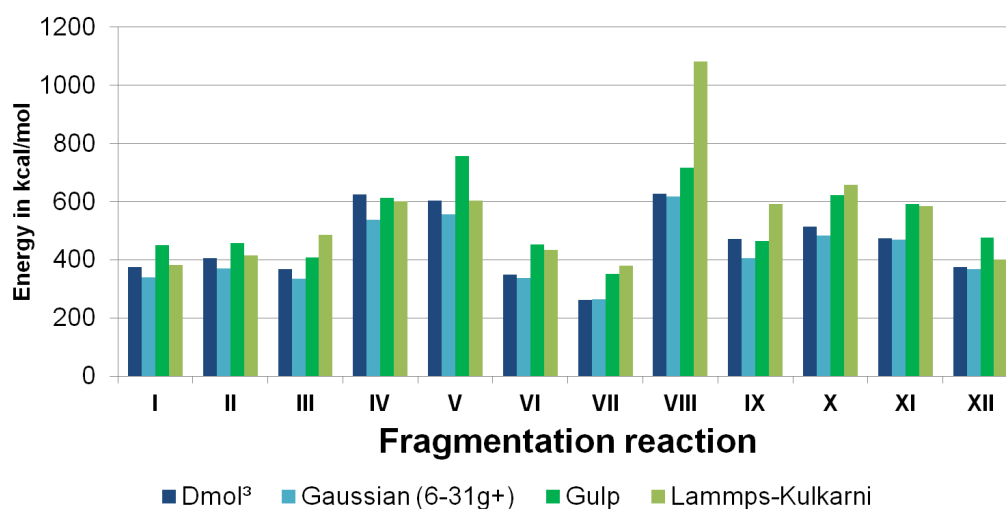


Figure 4.12.: Fragmentation of OMCTS for Dmol<sup>3</sup>, Gaussian, Gulp and Lammps.

means that mass spectroscopy of vaporized OMCTS molecules shows OMCTS after one fragmentation, whereas the mass spectroscopy of fragmented OMCTS is twice fragmented<sup>28</sup>. Thus, it is more likely that the mass spectroscopy result for the vaporized OMCTS is closer to the actual fragmentation than the result for the fragmented OMCTS plasma.

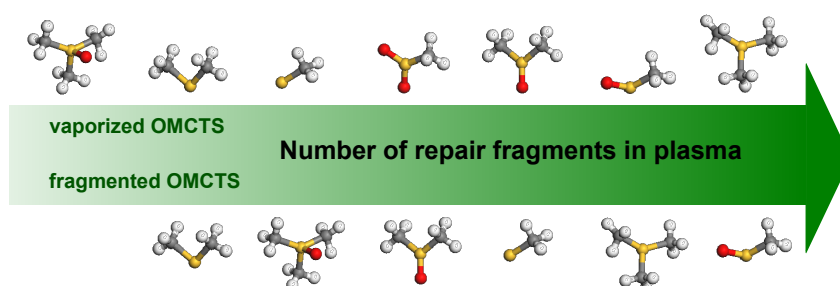


Figure 4.13.: Mass spectroscopy results for OMCTS vapor and fragmented OMCTS as reported in [10]. During the mass spectroscopy additional fragmentations take place. Thus the shown fragments were originally larger before the mass spectroscopy initiated further fragmentations.

The experimental results suggest that  $\text{SiOCH}_3$  and  $\text{Si}(\text{CH}_3)_3$  are the most prominent repair fragments gained by the fragmentation of OMCTS. However,  $\text{SiOCH}_3$  could originally have been  $\text{SiO}(\text{CH}_3)_2$  or  $\text{SiO}(\text{CH}_3)_3$  before the additional fragmentation took place during the mass spectroscopy. The mass spectrometer was set to only detect fragments larger than methane. This hinders a comparison as a large quantity of methyl would have supported the previously mentioned thesis. This effect of the mass spectroscopy makes comparing the experimental and computational results complicated.

<sup>28</sup>The first fragmentation occurs during the plasma fragmentation, the second fragmentation as part of the mass spectroscopy process.

### 4.2.4. Continuing Reactions

The small selection of studied DMADMS fragmentations only leads to two repair fragments. Due to their open shell nature, they are very reactive. Therefore, a wider range of repair fragments can be gained when they further react with methyl or methane. Also, the repair fragments  $\text{Si}(\text{CH}_3)_3\text{H}$  and  $\text{SiCH}_3\text{H}_2$  can be obtained by other repair fragments reacting with methyl and methane. Figure 4.14 displays ten possible reactions of the repair fragments obtained by the fragmentation of DMADMS and OMCTS with  $\text{CH}_4$ ,  $\text{CH}_3$  and  $\text{H}_2\text{O}$ .

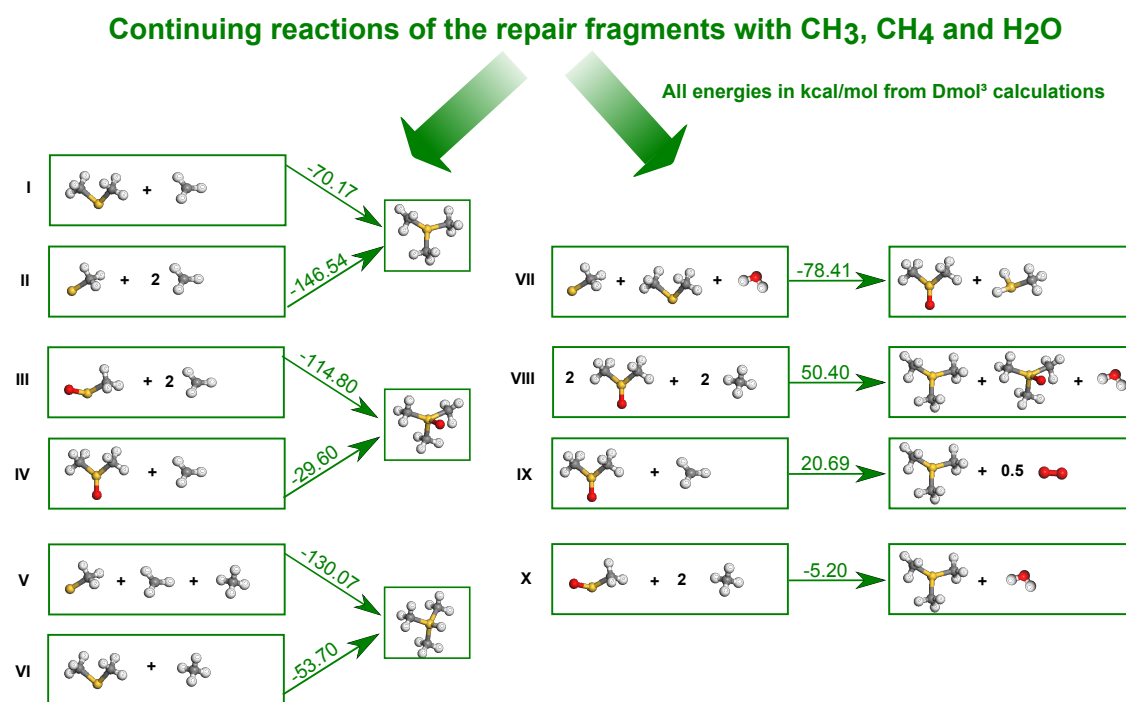


Figure 4.14.: Continuing reactions of the repair fragments. Possible further reactions of the repair fragments which are obtained by fragmenting DMADMS and OMCTS are shown.

Reactions **I** to **VI** are highly exothermic and indicate that larger repair fragments with three methyl groups are preferential. Further, reactions **VII** and **IX** demonstrate that oxygen containing repair fragments are energetically favored. Finally, reaction **X** shows that the effect of replacing one oxygen atom by two methyl groups does not yield a substantial energy gain, but one would rather expect an equilibrium situation with contributions of both educts and products. Here the reaction barrier would be crucial.

Figure 4.15 compares again the reaction energies obtained with all four methods.

While again Dmol<sup>3</sup> and Gaussian are in good agreement, the MD programs differ when either oxygen or water is involved in the reaction. However, they all agree that the addition of further methyl groups, and thus larger repair fragments, is preferential.

This leads to the conclusion that as long as enough methyl groups are present, the DMADMS fragmentation would primarily lead to the repair fragment  $\text{Si}(\text{CH}_3)_3$ . Otherwise all non-oxygen containing repair fragments should be distributed nearly equally.

The fragmentation of OMCTS, on the other hand, would primarily lead to  $\text{SiO}(\text{CH}_3)_2$ ,  $\text{SiO}(\text{CH}_3)_3$  and  $\text{Si}(\text{CH}_3)_3$ , with the preference changing in favor of  $\text{SiO}(\text{CH}_3)_3$  in a methyl rich atmosphere.

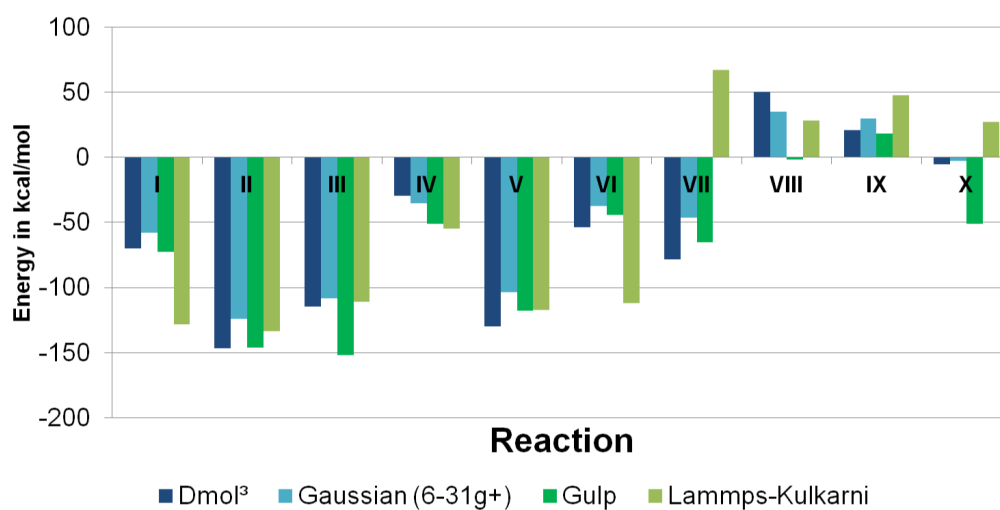


Figure 4.15.: Continuing reactions of the repair fragments with Dmol<sup>3</sup>, Gaussian, Gulp and Lammps.



## 5. Results and Discussion

The fragmentation reactions of DMADMS and OMCTS have shown that, while different absolute values for the reaction energies are obtained by the four different methodical approaches, the reaction preference is similar for all four methods. Thus, only Dmol<sup>3</sup> will be used here to study all possible repair reactions with the ULK-fragments. Based on these results selected repair reactions will be further studied with the remaining three implementations, either with ULK-fragments or on the silicon oxide cluster.

### 5.1. Reactions between Repair Fragments and ULK-Fragments

In this chapter the repair reactions between the ULK-fragments (see figure 4.1) and the repair fragments (see figure 4.5) are investigated with Dmol<sup>3</sup> and compared with the Gaussian results in chapter 5.1.3.

#### 5.1.1. Repair of OH-damages

As shown on figure 4.5, only eight of the ten repair fragments are able to repair an OH-damage. Furthermore, there are four ULK-fragments that represent an OH-damage, with SiH<sub>2</sub>OH<sub>2</sub> and SiH<sub>2</sub>(OH)<sub>2</sub> also presenting an OH<sub>2</sub>– and (OH)<sub>2</sub>–damage, respectively. This leads to 48 reactions in total which have to be investigated. The resulting reaction energies are displayed in figure 5.1.

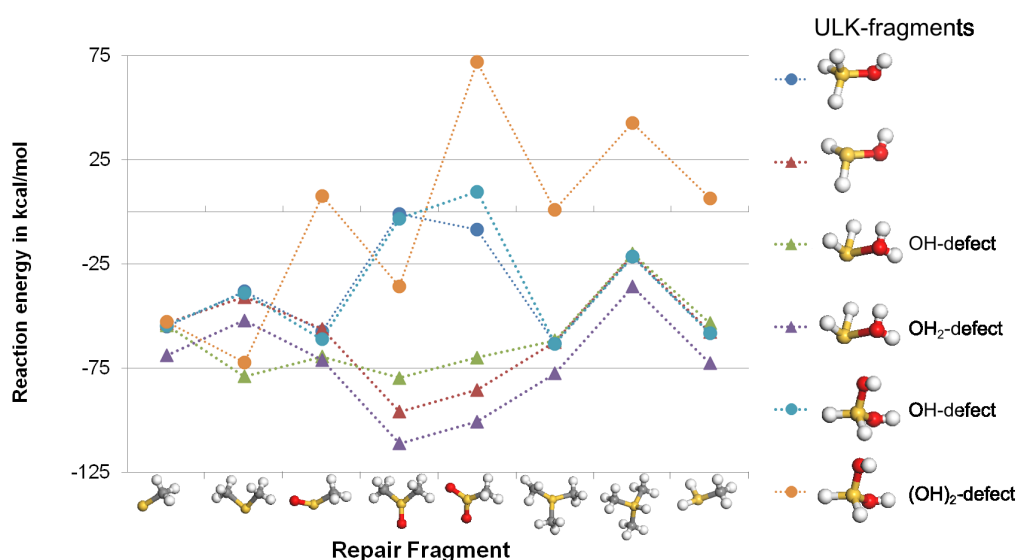


Figure 5.1.: Reaction energies from the repair of OH-damages. The ULK-fragments represented by dots are closed shell fragments, whereas the open shell ULK-fragments are displayed by triangles in the diagram. The dotted lines are only a guide for the eyes and show no correlations.

## 5. Results and Discussion

The most notable result from figure 5.1 is that all open shell ULK-fragments display a similar repair behavior. The energies between the different open shell ULK-fragments are only shifted by a nearly constant value. The same applies to the closed shell ULK-fragments when they represent a single OH-damage. The best suited repair fragments for the curing of an OH-damage are  $\text{SiO}(\text{CH}_3)_2$  and  $\text{Si}(\text{CH}_3)_3$  for open and closed shell ULK-fragments, respectively. Coincidentally, they are also the repair fragments that are favored during the fragmentation of OMCTS and DMADMS.

The reason why the reaction energies between closed and open shell ULK-fragments are in agreement for some specific cases, while they differ for other repair fragments is based on the structure of the product. Figure 5.2 shows exemplary reactions for each ULK-fragment type.

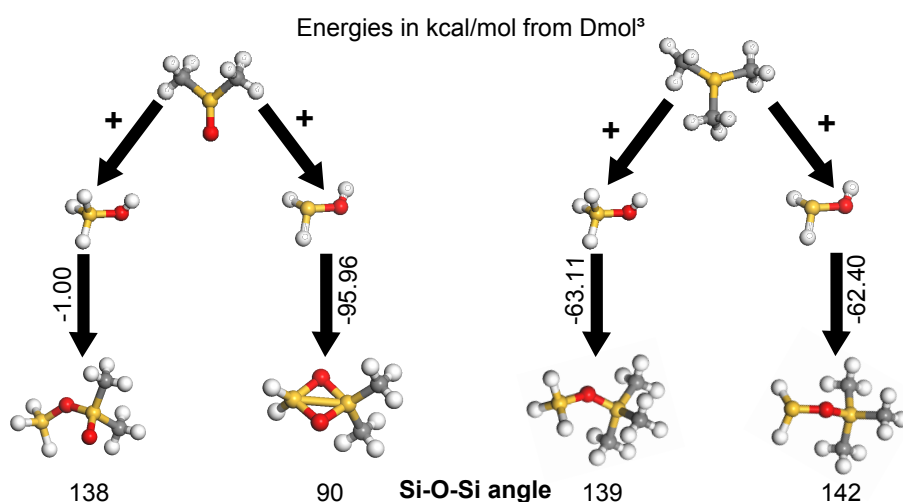


Figure 5.2.: Exemplary OH-damage repair reactions for ULK-fragments  $\text{SiH}_3\text{OH}$  (closed shell, left bifurcations) and  $\text{SiH}_2\text{OH}$  (open shell, right bifurcations). The desorbed 0.5  $\text{H}_2$  molecule is not displayed.

When the repair fragment  $\text{Si}(\text{CH}_3)_3$  (right in figure 5.2) reacts with the ULK-fragments  $\text{SiH}_3\text{OH}$  and  $\text{SiH}_2\text{OH}$ , the resulting products and the reaction energies are similar. This also shows up in the Si-O-Si angles that only differ by 4°.

For the repair fragment  $\text{SiO}(\text{CH}_3)_2$  (left in figure 5.2) the reaction energies differ immensely. The reason for this is that the open shell ULK-fragment  $\text{SiH}_2\text{OH}$  forms a product with a diamond-shaped SiO-center. This geometry is energetically preferential as the whole product becomes symmetric. All other energetically favorable products of open shell ULK-fragments also display the preferential diamond-shaped SiO-center. The product of the closed shell ULK-fragment  $\text{SiH}_3\text{OH}$ , on the other hand, displays a dangling oxygen bond. This results in the reaction energy being nearly 0 kcal/mol.

The diamond-shaped SiO-center is also energetically favorable during the  $\text{OH}_2^-$  and  $(\text{OH})_2^-$ -repair reactions (see figure 5.3). Here, the repair of an  $(\text{OH})_2^-$ -damage is only exothermic for the smaller repair fragments as they possess a higher amount of unpaired electrons and can build the diamond-shaped SiO-center. Repair fragments with only one unpaired electron are not able to close the second oxygen atom's dangling bond. Thus, the reaction energies for these repair fragments become endothermic.

For all repair fragments the repair of an  $\text{OH}_2^-$ -damage is strongly exothermic. This means that, in theory, all repair fragments should be able to eliminate enclosed water molecules from the ULK material. In practice, effects like steric hindrances block the water elimination.



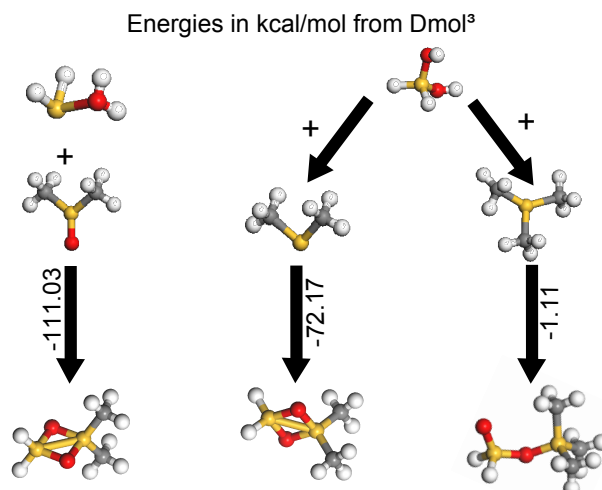


Figure 5.3.: Exemplary OH<sub>2</sub>- and (OH)<sub>2</sub>-damage repair reactions for the ULK-fragments SiH<sub>2</sub>OH<sub>2</sub> and SiH<sub>2</sub>(OH)<sub>2</sub>. The desorbed H<sub>2</sub> molecule is not displayed.

### 5.1.2. Repair of H-damages

Only five of the ten repair fragments contain oxygen atoms which are necessary to repair an H-damage, whereas all six ULK-fragments display an H-damage. This leads to 30 repair reactions that need to be studied. The resulting reaction energies are displayed in figure 5.4.

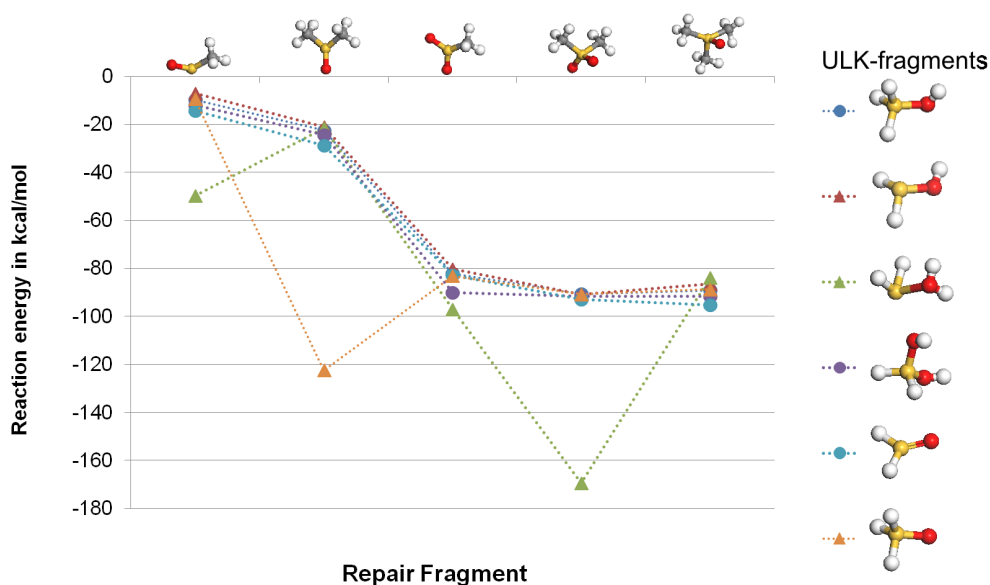


Figure 5.4.: Reaction energies from the repair of H-damages. The ULK-fragments represented by dots are closed shell fragments, whereas the open shell ULK-fragments are displayed by triangles in the diagram. The dotted lines are only a guide for the eyes and show no correlations.

All repair reactions are exothermic and independent of the close or open shell nature of the ULK fragment. It is notable that the reaction energies for the repair fragment SiO(CH<sub>3</sub>)<sub>2</sub> are by far higher for the repair of an H-damage than for the repair of an OH-damage. The repair

## 5. Results and Discussion

fragments  $\text{SiO}_2\text{CH}_3$ ,  $\text{SiO}_2(\text{CH}_3)_2$  and  $\text{SiO}(\text{CH}_3)_3$  all display similar reaction energies of around -90 kcal/mol even without the energetically preferable diamond-shaped SiO-center. Exemplary reactions are shown in figure 5.5. This is due to the flexibility of the Si-O-Si structure which differs by  $16^\circ$  without a correlation to the reaction energy.

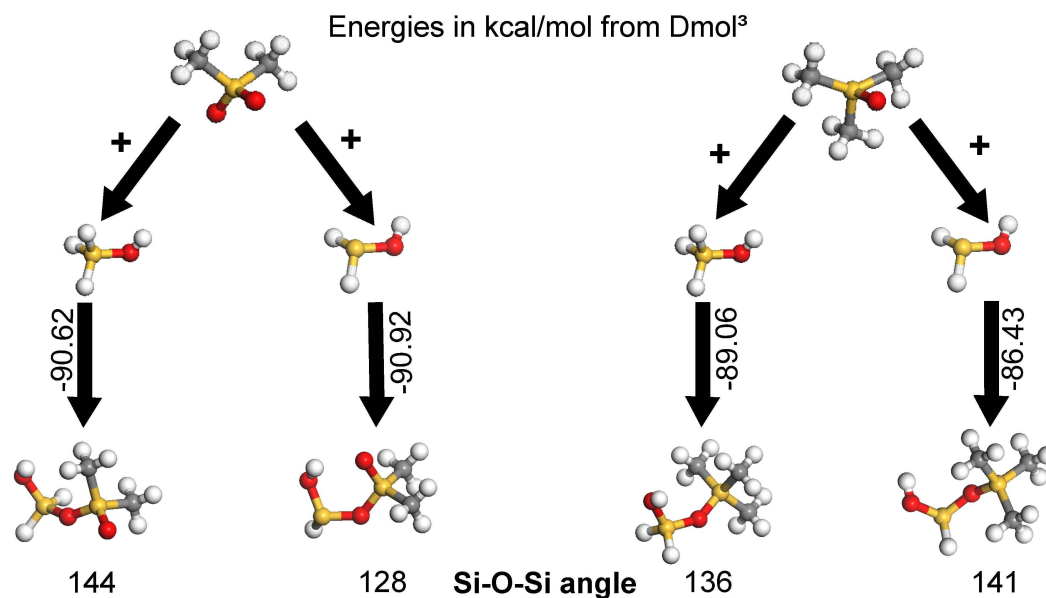


Figure 5.5.: Exemplary H-damage repair reactions for ULK-fragments  $\text{SiH}_3\text{OH}$  and  $\text{SiH}_2\text{OH}$ . The desorbed  $0.5 \text{ H}_2$  molecule is not displayed.

The energies for the reactions  $\text{SiH}_2\text{OH}_2$  with  $\text{SiO}_2(\text{CH}_3)_2$  and  $\text{SiH}_3\text{O}$  with  $\text{SiO}(\text{CH}_3)_2$  differ strongly from the other reactions. The reason for this is that both products are transition states as they still display imaginary frequency in the vibrational modes<sup>29</sup>. Further, the product of  $\text{SiH}_3\text{O}$  with  $\text{SiO}(\text{CH}_3)_2$  forms the preferable diamond-shaped Si-O-center (see figure 5.6).

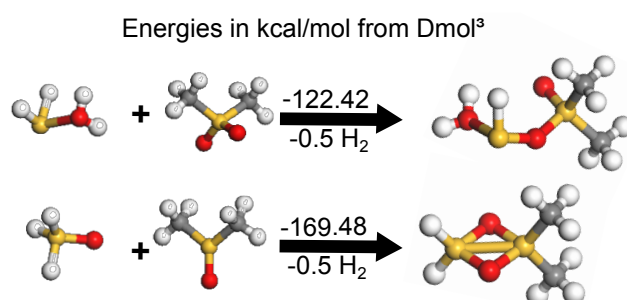


Figure 5.6.: Anomalous H-damage repair reactions for the ULK-fragments  $\text{SiH}_2\text{OH}_2$  and  $\text{SiH}_3\text{O}$ . The desorbed  $0.5 \text{ H}_2$  molecule is not displayed.

<sup>29</sup>The eigenvector following method was employed to find the corresponding ground states, but without success.

### 5.1.3. Selected Repair Reactions with Gaussian

With Dmol<sup>3</sup> the studied repair reactions have shown that each ULK-fragment has between one to three favored repair reactions. Thus, only the eight most promising OH-damage repair reactions and ten favored H-damage repair reactions will be re-studied with Gaussian. The expected deviations between Gaussian and Dmol<sup>3</sup> stem from methodical differences, such as a numerical basis set (DNP) versus a Gaussian type basis set (6-31g+) and the PBE functional versus the B3LYP functional.

The results of these eighteen reactions are displayed in figures 5.7 and 5.8.

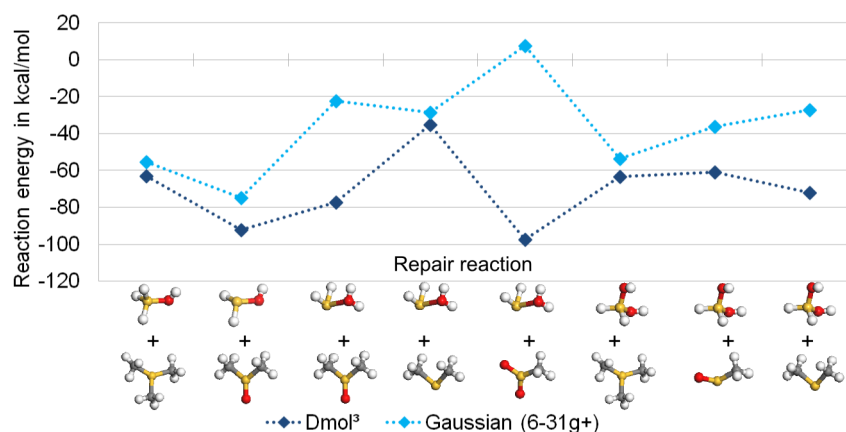


Figure 5.7.: Selected OH-repair reaction energies from Gaussian (light blue) in comparison with the Dmol<sup>3</sup> results (dark blue). The dotted lines are only a guide for the eyes and show no correlations.

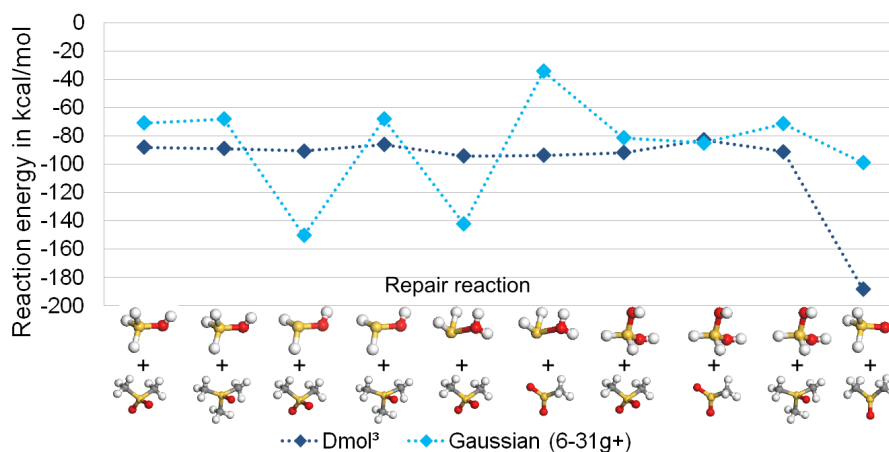


Figure 5.8.: Selected H-repair reaction energies from Gaussian (light blue) in comparison with the Dmol<sup>3</sup> results (dark blue). The dotted lines are only a guide for the eyes and show no correlations.

First, it is necessary to note that in contrast to Dmol<sup>3</sup>, the Gaussian calculations had trouble converging. This is a sign that the single reference method of Gaussian is not suited for open shell systems, making its results arguable.

Second, the gained reaction energies often differ from the Dmol<sup>3</sup> results, while other reactions indicate a fixed deviation of about 15 kcal/mol. These discrepancies could be due to the different

## 5. Results and Discussion

kind of basis sets or the functionals that were used with both methods. To eliminate the latter, the reaction energies were determined while using the B3LYP functional with Dmol<sup>3</sup> and Gaussian employing the PBE functional (see figures 5.9 and 5.10).

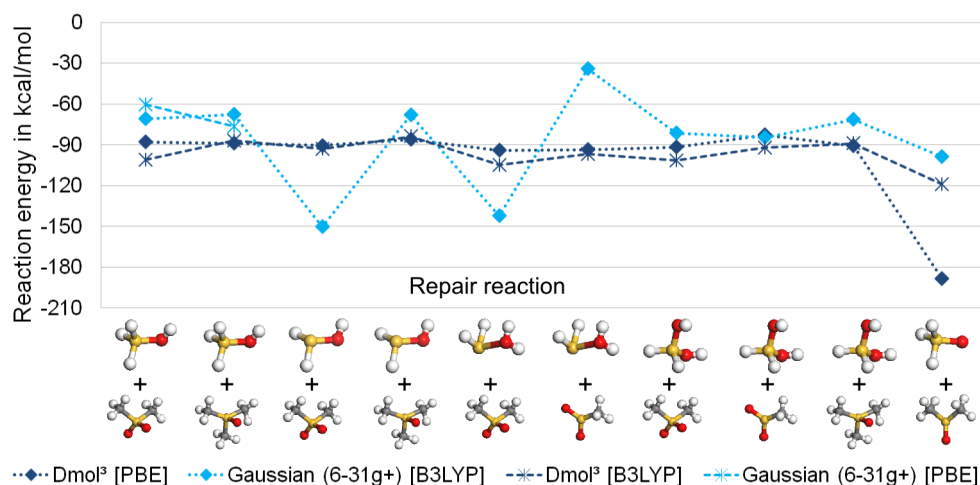


Figure 5.9.: Reaction energies from Gaussian (light blue) and Dmol<sup>3</sup> (dark blue) H-repair calculations with different functionals. The dotted lines are only a guide for the eyes and show no correlations.

Figure 5.9 shows that there is a normal, insignificant difference in the reaction energy when the functional in Dmol<sup>3</sup> is exchanged. For Gaussian only some reaction energies with the PBE functional could be calculated due to a worsening of the convergence, even though the SCF convergence criterion was lowered to  $10^{-4}$ . It again shows that the treatment by Gaussian is not suitable for this kind of repair reactions. Further, these functional based deviations cannot account for the differences between Gaussian and Dmol<sup>3</sup>.

The repair of OH-damages shows a similar result (see figure 5.10). Here, Gaussian had even stronger convergence problems that no reliable energies<sup>30</sup> with the PBE functional could be calculated. Thus, only the energies for Dmol<sup>3</sup> with the PBE functional can be discussed.

The dispersion correction used in Dmol<sup>3</sup> was investigated as a further possible source of the deviation. However, the results show that the dispersion correction is not the source of the discrepancies. Appendix A.3.2 shows the detailed results. The results also imply that the deviations are either due to the different basis sets<sup>31</sup> or the implementation. Considering Gaussian's convergence problem, it is likely that the latter is the case. In summary, it can be said that Gaussian with the used settings is not suited for this problem.

<sup>30</sup>The calculations only converge for a SCF convergence criterion of  $10^{-2}$ . This is too low to be considered accurate.

<sup>31</sup>Dmol<sup>3</sup> uses a numerical basis set, whereas Gaussian's basis set consists of Gaussian type orbitals.

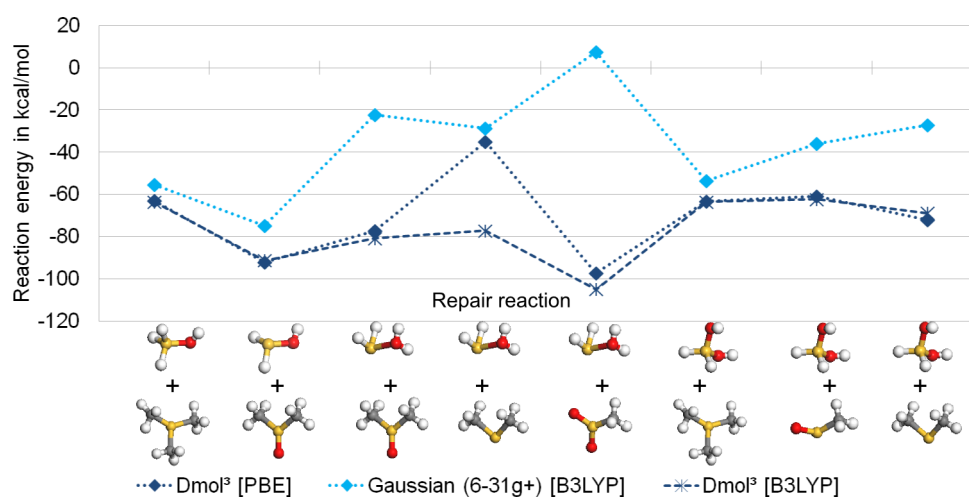


Figure 5.10.: Reaction energies from Gaussian (light blue) and Dmol<sup>3</sup> (dark blue) OH-repair calculations with different functionals. The dotted lines are only a guide for the eyes and show no correlations.

## 5.2. Reactions Between Repair Fragments and Silicon Oxide Cluster

As described in chapter 4.1, the final aim of the present work is to investigate the repair reactions on large clusters that contain pores. To get a first insight to what extent the presence of a cluster influences the reaction energies the preferred repair reactions from the chapters 5.1.1 and 5.1.2 were repeated on the silicon oxide cluster. Here, Dmol<sup>3</sup>, Gulp and Lammmps-Kulkarni were used. Gaussian was not used as the results of the ULK-fragment reactions were questionable.

### 5.2.1. Comparison Between ULK-Fragments and Silicon Oxide Cluster

First, the impact of the silicon oxide cluster on the reaction energy is studied with Dmol<sup>3</sup>. For this, the preferable repair molecules from the chapters 5.1.1 and 5.1.2 react with the silicon oxide cluster. For the repair of an OH-damage these are:  $\text{Si}(\text{CH}_3)_2$ ,  $\text{SiOCH}_3$ ,  $\text{SiO}(\text{CH}_3)_2$ ,  $\text{SiO}_2\text{CH}_3$  and  $\text{Si}(\text{CH}_3)_3$ . For the repair of an H-damage, there are:  $\text{SiO}(\text{CH}_3)_2$ ,  $\text{SiO}_2\text{CH}_3$ ,  $\text{SiO}_2(\text{CH}_3)_2$  and  $\text{SiO}(\text{CH}_3)_3$ .

To determine whether the boundary (as described in chapter 4.1.2) was chosen correctly, the product energies were calculated with a fixed cluster boundary and repeated with a freely relaxed boundary. The results of both calculations, as well as the energy of the repair reactions with the ULK-fragment  $\text{SiH}_2(\text{OH})_2$  (for comparison reason), are shown in figures 5.11 and 5.12.

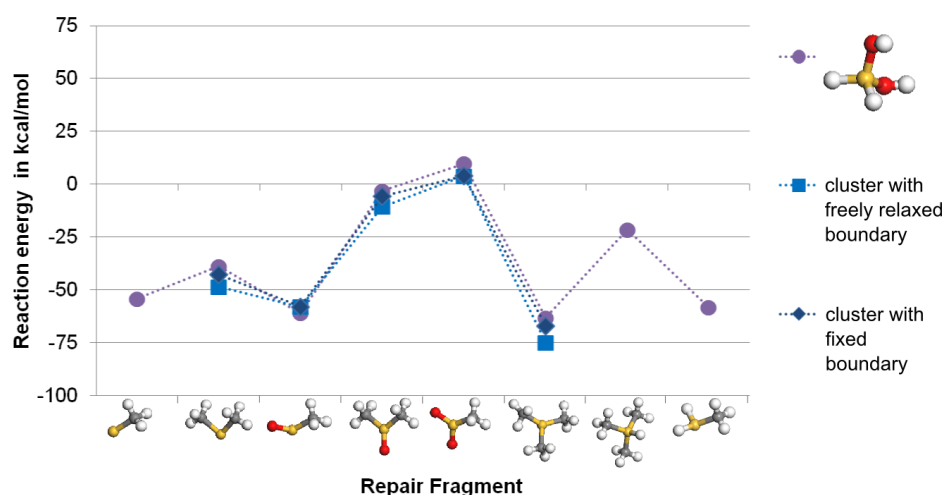


Figure 5.11.: OH-repair on the silicon oxide cluster (blue). The energy of the ULK-fragment  $\text{SiH}_2(\text{OH})_2$  are added in violet for comparison reason. The dotted lines are only a guide for the eyes and show no correlations.

The first conclusion that can be gained from figures 5.11 and 5.12 is that the energies of a geometrically fixed and a fully optimized cluster boundary only differ slightly. Therefore, the chosen boundary was selected correctly and will not significantly influence the calculation results while saving computation time (refer to appendix A.2.3).

The second conclusion is that the reaction energies between the cluster and the closed shell ULK-fragment  $\text{SiH}_2(\text{OH})_2$  are nearly identical. Therefore, the silicon oxide surface of the cluster does not influence the reaction energy.

For further investigations with possible new repair fragments this means that instead of calculating the reaction with the time-consuming silicon oxide cluster, their repair behavior can be studied with ULK-fragments. Hereby, not only the closed shell fragment  $\text{SiH}_2(\text{OH})_2$  should be

## 5.2. Reactions Between Repair Fragments and Silicon Oxide Cluster

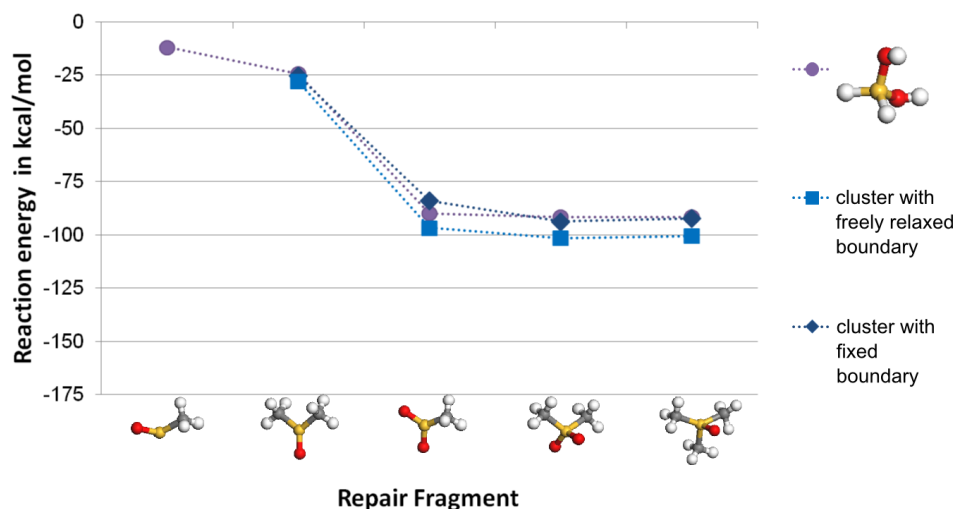


Figure 5.12.: H-repair on the silicon oxide cluster (blue). The energy of the ULK-fragment  $\text{SiH}_2(\text{OH})_2$  are added in violet for comparison reason. The dotted lines are only a guide for the eyes and show no correlations.

used but also the open shell fragment  $\text{SiH}_2\text{OH}$  or  $\text{SiH}_2\text{OH}_2$ . The reason for this approach is that the silicon oxide cluster used in the present work is a closed shell system. However, in reality the defective ULK material with its pores is likely to be an open shell system. Thus, both types of ULK-fragments should be taken into consideration as they display a different repair behavior (see chapter 5.1).

### 5.2.2. Comparability of DFT and MD Results

While the previous sub-chapter showed that the silicon oxide clusters can be approximated by the ULK-fragments, the effect of pores is still not taken into consideration. For this larger clusters need to be designed which can only be treated with MD methods. Therefore, the silicon oxide cluster is an ideal test system to compare the repair reactions with DFT-Dmol<sup>3</sup> and the MD implementations Gulp and Lammmps-Kulkarni.

Figure 5.13 shows the reaction energy for the repair of OH-damages obtained with Dmol<sup>3</sup>, Gulp and Lammmps-Kulkarni.

In analogy to the DMADMS and OMCTS fragmentations, Gulp and Lammmps with the Kulkarni force field differ from the Dmol<sup>3</sup> results. The energy calculated with Lammmps and the Kulkarni force field are always more strongly exothermic than the Dmol<sup>3</sup> reference energies. Especially the high energy difference for the repair reaction of  $\text{Si}(\text{CH}_3)_2$  clearly indicates the limits of this force field approach.

Gulp, on the other hand, is (with some exceptions) in relatively good agreement with Dmol<sup>3</sup>. For the repair reactions of  $\text{SiO}(\text{CH}_3)_2$  and  $\text{SiO}_2\text{CH}_3$  the discrepancies between the Dmol<sup>3</sup> and Gulp results are the most pronounced. To investigate this, additional Dmol<sup>3</sup> calculations were carried out with the optimized Gulp structures as the starting geometry (see turquoise bars in figure 5.13).

While these new reaction energies still differ from the original Dmol<sup>3</sup> results, they are still in the error range of Dmol<sup>3</sup>. The energy landscape of the studied silicon oxide cluster is the reason for those differences. During the geometry optimization either the energy barrier was too high to overcome and reach the energetically lower state, or there are many local minima with nearly

## 5. Results and Discussion

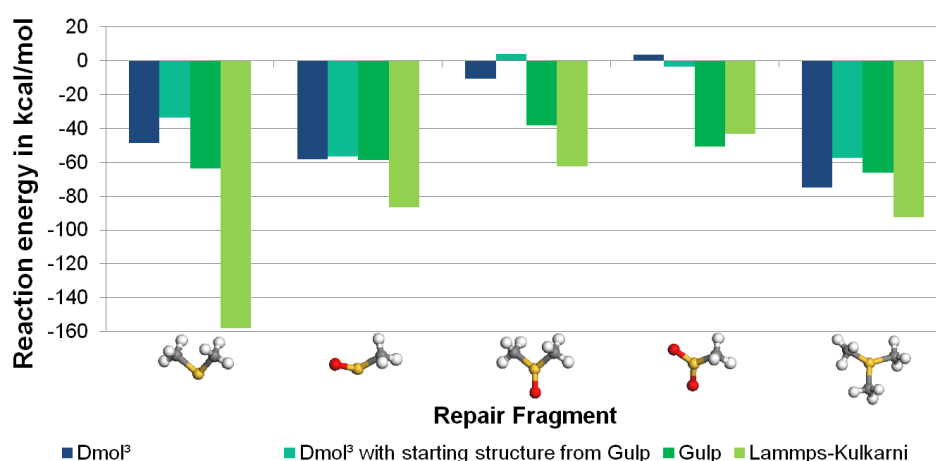


Figure 5.13.: OH-repair on the silicon oxide cluster with Dmol<sup>3</sup>, Gulp and Lammmps-Kulkarni. The turquoise bars show the results from Dmol<sup>3</sup> calculations where the starting geometry was taken from the Gulp optimized structure.

identical energies, or the barriers between various local minima are too high <sup>32</sup>.

The repair of H-damages was also studied with MD methods (see figure 5.14). Gulp is once again closer to the DFT results gained with Dmol<sup>3</sup> than the Lammmps with the Kulkarni force field. However, they both deviate more strongly from the Dmol<sup>3</sup> reference energies in comparison to the OH-repair. Still, Gulp would be the better suited method to investigate larger silica clusters that also include pores and methyl groups. Here, an approximate error range of 20 kcal/mol should be taken into consideration.

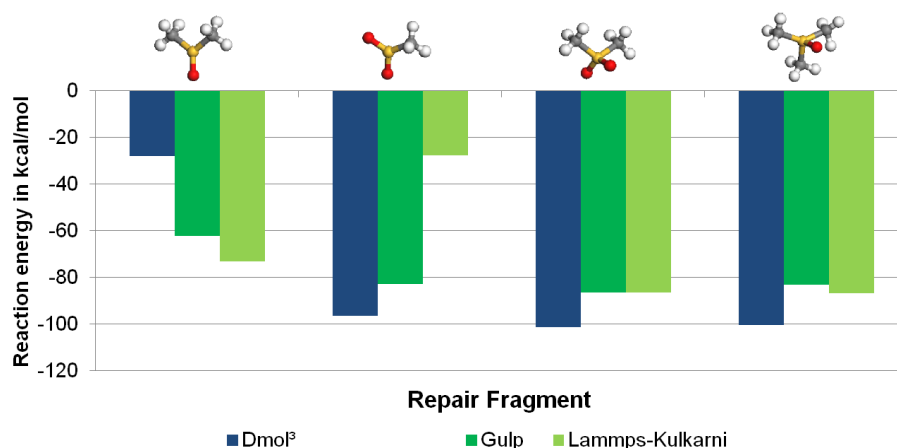


Figure 5.14.: H-repair on the silicon oxide cluster with Dmol<sup>3</sup>, Gulp and Lammmps-Kulkarni.

To illustrate the energy difference between Dmol<sup>3</sup> and Lammmps, the optimized clusters for the repair of the H-damage with SiO<sub>2</sub>CH<sub>3</sub> are displayed in figure 5.15. The deviation in the energy is due to two obvious differences in the geometry of the repaired cluster.

First, the alignment of the repair fragment is different. The oxygen atoms of SiO<sub>2</sub>CH<sub>3</sub> are

<sup>32</sup>The silicon oxide cluster is too large to calculate its eigenfrequencies in Dmol<sup>3</sup> and the MD methods do not offer eigenfrequency calculations. Thus, it cannot be determined if the found geometry is a ground or transition state. However, the structure with the lowest energy should be the one closest to the real ground state.



orientated vertically to the cluster in Dmol<sup>3</sup>, whereas in Lammmps-Kulkarni they display a more horizontal orientation.

Second, with Lammmps-Kulkarni the cluster's basic structure is closer to the ordered bulk phase, whereas the Dmol<sup>3</sup> cluster displays a much more disordered basic structure. Thus, the entropy contribution to the overall energy is larger after the optimization with Dmol<sup>3</sup> cluster than with Lammmps-Kulkarni. This explains why the reaction of the H-repair with SiO<sub>2</sub>CH<sub>3</sub> is more exothermic in DFT-PBE calculations (Dmol<sup>3</sup>) than in the simulations with Lammmps and the Kulkarni force field.

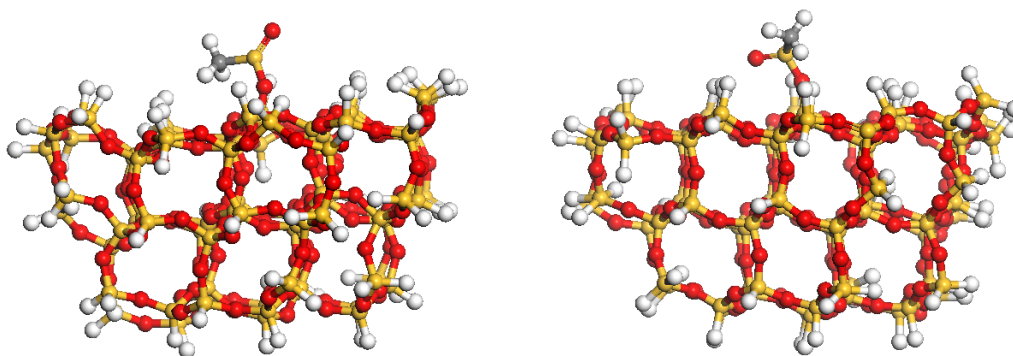


Figure 5.15.: Silicon oxide cluster from Dmol<sup>3</sup> (left) and Lammmps (right) after the repair of an H-damage with SiO<sub>2</sub>CH<sub>3</sub>.

In summary, to reliably investigate the repair reactions on a silicon oxide cluster the current MD force fields either must be improved or a new force field must be developed.

### 5.3. Comparison with Experimental Results

Finally, the theoretical results gained in the present work are compared with experimental works. In the student research project [68] the repair effect of DMADMS and OMCTS was studied and the results are currently in the process of being published [69].

Both studies only measure the magnitude of the  $\gamma$ -restore process and not which repair fragment is responsible or if an H- or OH damage was repaired. In short, they are unable to pinpoint the exact repair mechanism.

The experimental investigations [68] and [69] are summarized in figure 5.16. Here, the results of surface energy measurements are displayed, and divided into their polar (light gray) and dispersive (dark gray) contributions. The reference values for the pristine and damaged ULK material illustrate that the polar contribution to the surface energy should be nonexistence to obtain a defect free ULK material. The increased polar contribution in the damaged sample is a result of water adsorption and the development of H- and OH-damages. Thus a repair effect shows in the decrease of the polar surface energy contribution, as well as a decreased total surface energy.

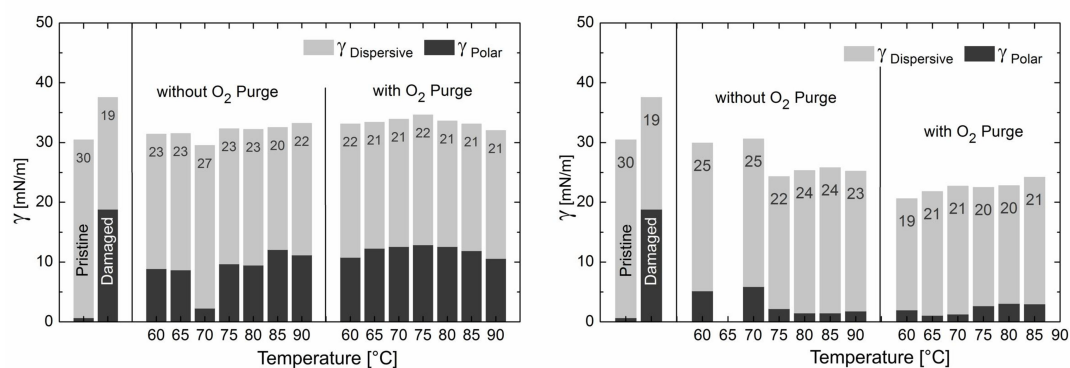


Figure 5.16.: Experimental repair of damaged ULK materials with DMADMS (left) and OMCTS (right). They display the results of surface energy measurements after plasma repair at different temperatures, with and without oxygen purge and reference measurements of the pristine and damaged ULK material. The good repair effect of DMADMS at  $T=70^{\circ}\text{C}$  is a defective outlier. Diagrams taken from [69].

There are three major results that can be taken from figure 5.16. First, the repair fragments from both DMADMS and OMCTS fragmentations display a repair effect. However, neither process can deliver a 100% repair effect (see figure 5.16). Second, the repair with OMCTS fragments is more successful than the repair with DMADMS fragments (see polar contributions in figure 5.16). And finally, while an oxygen pretreatment<sup>33</sup> positively influences the OMCTS repair, it lessens the effectivity of the DMADMS repair.

While the last point was not investigated within the present work, the first two points can be confirmed. The results for the OH-repair show that the repair fragment  $\text{Si}(\text{CH}_3)_3$  is preferable, while for the H-damage repair the fragments  $\text{SiO}_2(\text{CH}_3)_2$  and  $\text{SiO}(\text{CH}_3)_3$  are better suited. However, these repair fragments provide a steric hindrance which prevents other repair reactions to take place in its vicinity (refer figure 5.15). Thus, not all defects can be repaired. Also, defects that are enclosed in pores or are too deep inside the material, cannot be reached by the fragments and thus no repair process can take place in these areas.

The obtained reaction energies show that the repair of an H-damage is more strongly exother-

<sup>33</sup>Before the damaged ULK materials react with the repair fragments, the ULK materials are exposed to oxygen with the aim to convert H-damages into OH-damages.

### 5.3. Comparison with Experimental Results

mic than the repair of an OH-damage. Further, only OMCTS yields oxygen containing repair fragments for the H-damage repair<sup>34</sup>. Thus, the OMCTS fragments show a better repair behavior than the DMADMS fragments.

---

<sup>34</sup>Through the reaction with water and oxygen the non-oxygen containing repair fragments obtained from DMADMS can react to oxygen containing ones (compare chapter 4.2.4).



## 6. Summary and Outlook

In the present work, the plasma repair for damaged ULK materials, newly developed at the Fraunhofer ENAS, was studied with DFT and MD methods to obtain new insights into this repair process. The ULK materials owe their low  $k$ -value to the insertion of  $k$ -value lowering methyl groups. During the manufacturing process, the ULK materials are damaged and their  $k$ -values increase due to the adsorption of hydroxyl groups (OH-damage) and hydrogen atoms (H-damage) that replaced the methyl groups. So far, the plasma repair process is the only known method that can repair H-damages.

The first investigation point was the creation of repair fragments. For this purpose the silylation molecules DMADMS and OMCTS were fragmented. Here, only fragmentation reactions that lead to repair fragments that contain one silicon atom and at least one methyl group were considered.

The fragmentation of DMADMS shows that, at a temperature of 0 K, all fragmentation reactions are endothermic with fragmentation energies of at least 110 kcal/mol. Here, the fragmentations that lead to closed shell byproducts are preferable. Further, the repair fragment  $\text{Si}(\text{CH}_3)_2$  is favored. However, in a methyl containing atmosphere this repair fragment will further react to  $\text{Si}(\text{CH}_3)_3$  with an exothermic reaction energy of -70 kcal/mol.

The fragmentation of the oxygen containing OMCTS silylation molecule is also strongly endothermic with energies of at least 262 kcal/mol. Here, the preferably formed repair fragments are  $\text{SiO}(\text{CH}_3)_2$ ,  $\text{SiO}(\text{CH}_3)_3$  and  $\text{Si}(\text{CH}_3)_3$ , with the preference changing in favor of  $\text{SiO}(\text{CH}_3)_3$  in a methyl rich atmosphere.

The different fragmentation energies of OMCTS and DMADMS are comparable to their use as silylation molecules. In [25] the activation energy for DMADMS was stated as 20 kcal/mol and for OMCTS a value of 36 kcal/mol was given. This energy proportion of OMCTS requiring twice as much energy as DMADMS reflects in their lowest fragmentation energies (262 kcal/mol for OMCTS to 110 kcal/mol for the DMADMS fragmentation).

For the investigation of the repair behavior of the above gained fragments two model systems were created that represented OH- and H-damages. A small set of ULK-fragments was used to screen many possible repair reactions, whereas a silicon oxide cluster was used to study selected repair reactions and the influence of surrounding atoms.

The screening of the repair reactions between the ULK-fragments and the repair fragments showed that for the repair of an OH-damage the repair fragments  $\text{Si}(\text{CH}_3)_2$ ,  $\text{SiOCH}_3$ ,  $\text{SiO}(\text{CH}_3)_2$ ,  $\text{SiO}_2\text{CH}_3$  and  $\text{Si}(\text{CH}_3)_3$  are the most promising. For the repair of an H-damage  $\text{SiO}(\text{CH}_3)_2$ ,  $\text{SiO}_2\text{CH}_3$ ,  $\text{SiO}_2(\text{CH}_3)_2$  and  $\text{SiO}(\text{CH}_3)_3$  are the most successful. This result is consistent with the studied fragmentations as most of these best working repair fragments were favored during the DMADMS and OMCTS fragmentations.

The repair reactions of the above listed favorable repair fragments were repeated on a silicon oxide cluster. Here,  $\text{Si}(\text{CH}_3)_3$  was confirmed as the most effective repair fragment for an OH-damage, and  $\text{Si}(\text{CH}_3)_2$  for a double OH-damage. And for the repair of an H-damage,  $\text{SiO}_2\text{CH}_3$ ,  $\text{SiO}_2(\text{CH}_3)_2$  and  $\text{SiO}(\text{CH}_3)_3$  were found equally successful. Figure 6.1 summarizes these findings.

As for a comparison with experimental results, the main problem is that from the experimental side only the overall results of the repair with various fragments can be determined or that the measurements bias the results. The latter is especially the case for the mass spectroscopy results, where additional fragmentation take place during the measuring process. Here, at least a general preference for  $\text{SiO}(\text{CH}_3)_2$  and  $\text{Si}(\text{CH}_3)_3$  could be confirmed.

## 6. Summary and Outlook

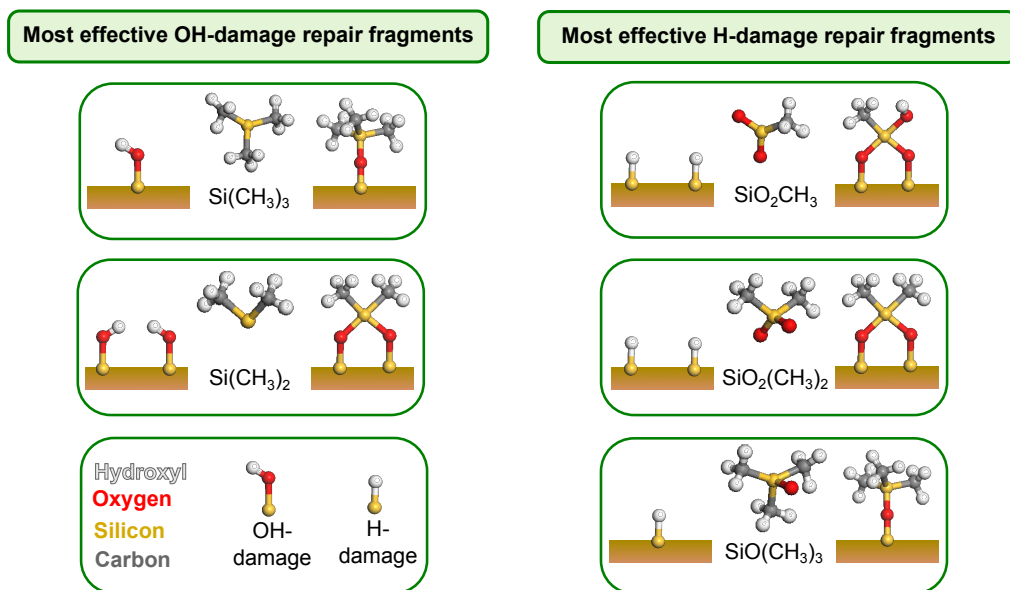


Figure 6.1.: The most effective repair fragments for the repair of OH- and H-damages from the silicon oxide cluster calculations. The repair fragment  $\text{Si}(\text{CH}_3)_3$  effectively repairs a single OH-damage, whereas  $\text{Si}(\text{CH}_3)_2$  is preferable for the repair of a double OH-damage.

Further, the experimental results show that in comparison to DMADMS, OMCTS displays a better repair effect. This difference can be explained with the results from the present work. The reaction energies for the H-repair are more strongly exothermic than for the OH-repair and as the DMADMS fragments only can repair OH-damages, it is a less effective repair agent than OMCTS.

Finally, the present work lays a foundation for future studies. The reaction energies obtained from the repair processes on the silicon oxide cluster are similar to the ULK-fragment  $\text{SiH}_2(\text{OH})_2$ . Thus, for example, if the repair effect of new possible repair fragments is to be investigated, then testing the repair effect with the closed shell ULK-fragment  $\text{SiH}_2(\text{OH})_2$ , as well as with one of the two open shell fragment  $\text{SiH}_2\text{OH}$  or  $\text{SiH}_2\text{OH}_2$  is sufficient.

When the ULK-fragment  $\text{SiH}_2(\text{OH})_2$  was investigated as a double OH-damage, the effect of steric hindrance was very prominent, making  $\text{Si}(\text{CH}_3)_2$  preferable to  $\text{Si}(\text{CH}_3)_3$ . Thus, a more realistic cluster with different forms of steric hindrance in forms of pores and adsorbed methyl groups should be studied in the future. For this the MD implementation Gulp should be used. While both MD implementations used in the present work (Gulp and Lammmps-Kulkarni) deviated from the DFT-Dmol<sup>3</sup> results, Gulp is closer to the Dmol<sup>3</sup> values. However, an error of about  $\pm 20$  kcal/mol in comparison to the Dmol<sup>3</sup> results has still to be taken into consideration.

Among the tested ReaxFF force fields for Lammmps, only the Kulkarni force field [63] came close to the Dmol<sup>3</sup> reaction energies. Thus, if a ReaxFF force field for the repair of damaged ULK materials should be optimized, the Kulkarni force field would be a good starting point. Here, especially the oxygen-silicon interaction parameters should be adjusted based on the results shown in figure 4.9.

In summary, this work provides the basis for the quantum chemical investigation of the plasma repair process of damaged ULK materials. However, in the future an expanded silicon oxide cluster with pores and adsorbed methyl groups should be created to take the effect of the steric hindrance into a better consideration. In addition, the expanded cluster can be used to study how deep the repair fragments can penetrate into the defective ULK material.

## A. Appendix

### A.1. Temperature Influence

#### A.1.1. Temperature Influence on the DMADMS Fragmentation in $\text{Dmol}^3$

Figure A.1 shows the results for the DMADMS fragmentation as given in figure 4.7 in dependence of the reaction temperature. Here a range from 0-600 K<sup>35</sup> was considered.

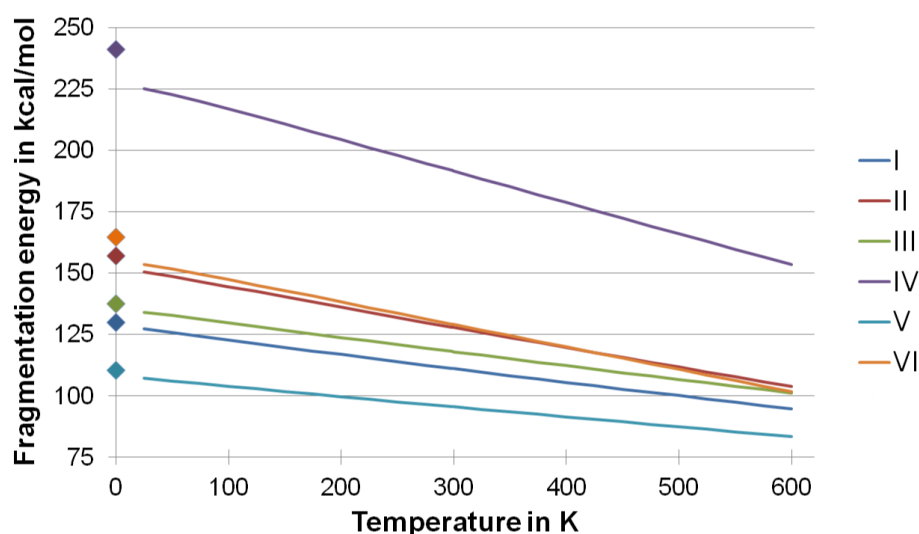


Figure A.1.: Temperature influence on the DMADMS fragmentation in  $\text{Dmol}^3$

The jump between 0 K and 25 K is due to the first addition of the Gibb's free energy correction term<sup>36</sup> to the reaction energy at 0 K. From there on, the temperature influence is linear. In the investigated temperature range, fragmentation V is always the energetically favorable. However, the stronger descent of the open shell byproducts' reactions tends towards them becoming preferential at higher temperatures (above 1000 K).

Figure A.1 also confirms that the outlier in figure 5.16 is a defective outlier as no special behavior in the the fragmentation energy curve of DMADMS can be observed.

#### A.1.2. Temperature Influence on the OMCTS Fragmentation in $\text{Dmol}^3$

In analogy to the DMADMS fragmentation, the temperature dependence of the OMCTS fragmentation as given in figure 4.10 is shown in figure A.2. Here, also a range from 0-600 K<sup>37</sup> was considered.

<sup>35</sup>The reaction energies were calculated every 25 K.

<sup>36</sup>See chapter 2.2 for details.

<sup>37</sup>The reaction energies were calculated every 25 K.

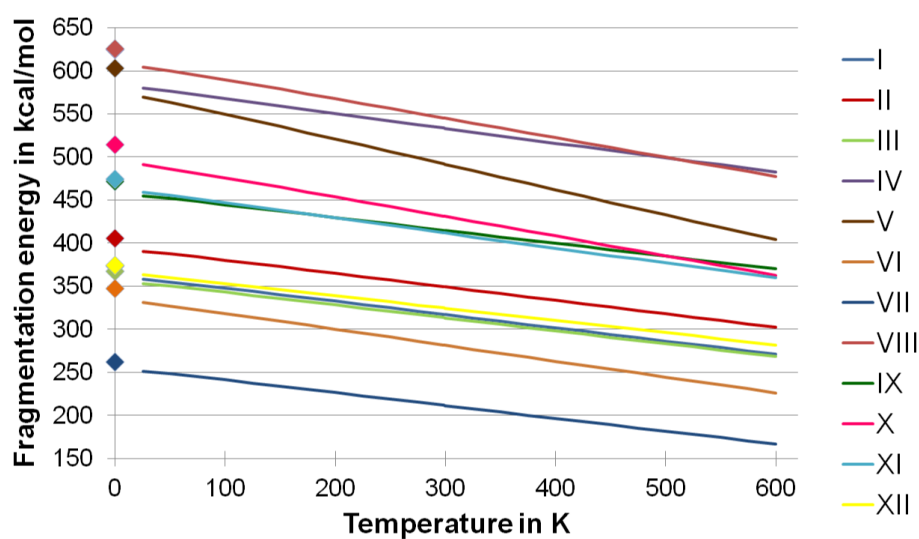


Figure A.2.: Temperature influence on the OMCTS fragmentation in Dmol<sup>3</sup>

Again, the jump between 0 K and 25 K is due to the first addition of the Gibb's free energy correction term<sup>38</sup> to the reaction energy at 0 K. From there on, the temperature influence is linear. In the investigated temperature range, fragmentation **VII** is always the energetically favorable. It is notable that reaction **V** has the strongest descend. At higher temperatures of about 2100 K this reaction together with reaction **VI** will become as energetically preferable as reaction **VII**. This is also roughly the temperature at which the fragmentation becomes exothermic.

<sup>38</sup>See chapter 2.2 for details.



## A.2. Tests

### A.2.1. DMADMS Fragmentation with Gaussian

Figure A.3 shows the results from Gaussian for the DMADMS fragmentation reactions as depicted in figure 4.7. Here, not only the results for the 6-31g+ basis set with additional polarization functions, but also of the larger basis sets cc-pVTZ/cc-pVQZ are displayed. While the calculation times for these three basis sets are too high to be used in this thesis, their results for the DMADMS fragmentation allow inference for further results with the 6-31g+ basis set.

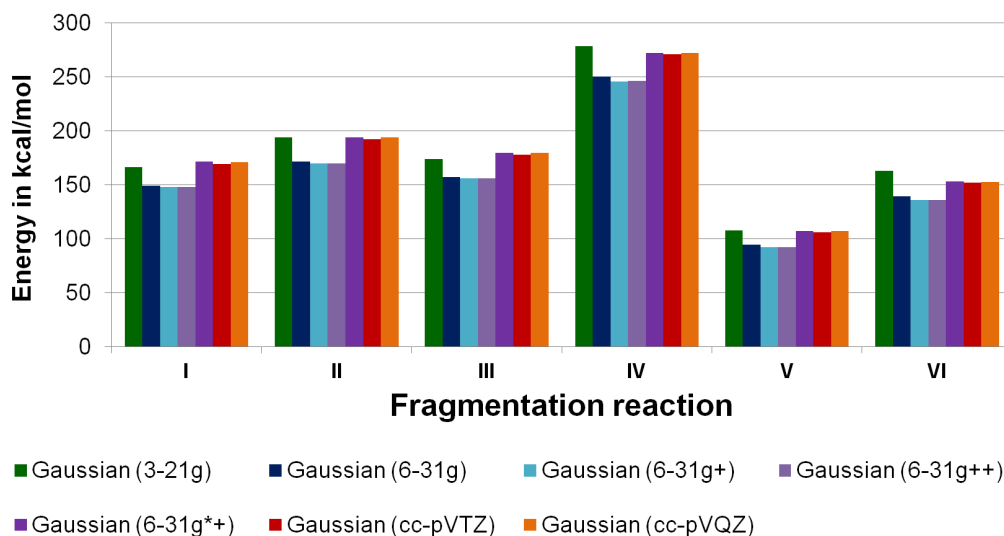


Figure A.3.: Fragmentation of DMADMS with different Gaussian basis sets

It is interesting to note that for this example the results for the small and very fast basis set 3-21g is close to the ones from 6-31g\*+ and cc-pVQZ. However, these agreements are only incidental and the 3-21g basis set is too small to obtain reliable reaction energies. Thus, the 3-21g basis set will not be used in the scope of this thesis.

Furthermore, there is a rather constant energy difference of 15-25 kcal/mol between the 6-31g+ basis set used throughout this thesis and the larger basis sets 6-31g\*+ and cc-pVQZ. Thus, one should keep in mind that the energies gained with Gaussian (6-31g+) are underestimated by 15-25 kcal/mol.

### A.2.2. G2 Test Set

Curtiss et al. published their paper 'Assessment of Gaussian-2 and density functional theories for the computation of enthalpies of formation' [70] in 1997, which later became known as the G2 test set. They investigated the performance of different functionals in Gaussian-2 by calculating the heat of formation energies.

Seven silicon containing complexes from the G2 test set were chosen to study the performance of the DFT and MD methods used in this thesis. The energies were calculated as described in [70] and are shown in figure A.4.

There are three major conclusions that can be made from figure A.4. The first one is that both DFT methods underestimate the energies in comparison to the experimental data from the G2 test set. Hereby, Dmol<sup>3</sup> shows a systematical error of about -6.5 kcal/mol per paired silicon electron.

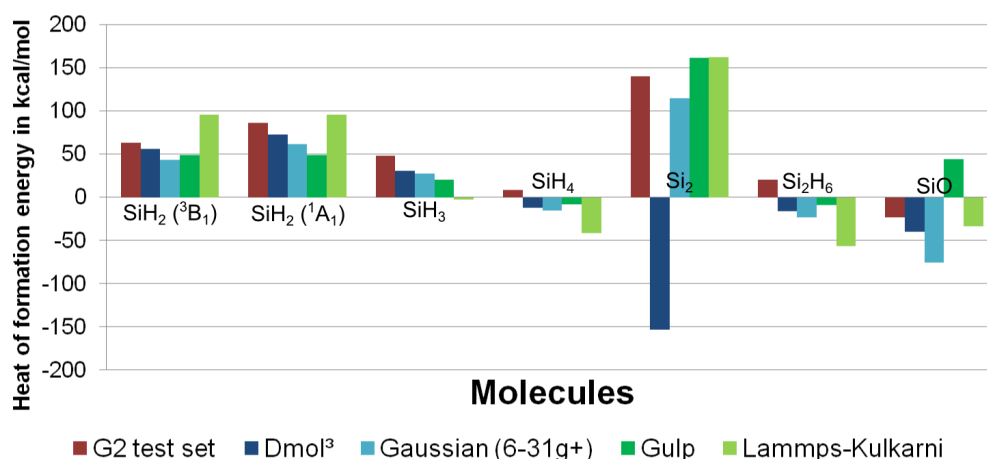


Figure A.4.: G2 test set comparison

Secondly, as expected, neither MD method is able to differentiate between the SiH<sub>2</sub>'s (<sup>1</sup>A<sub>1</sub>) and (<sup>3</sup>B<sub>1</sub>) state. Furthermore, opposed to the DFT methods, both Lammmps and Gulp unsystematically under- and overestimate the heat of formation energies.

And finally, the comparison with the G2 test set gives a first estimation of the error of each method. Gaussian and Lammmps-Kulkarni display an error range of about  $\pm 11$  kcal/mol per paired silicon electron and Gulp a value of  $\pm 8$  kcal/mol per paired silicon electron.

### A.2.3. Calculation Time of the Silicon Oxide Cluster in Dmol<sup>3</sup>

In chapter 5.2.1 it was demonstrated that the energy difference of the silicon oxide cluster with a fixed and a freely relaxed boundary is minimal. Here, figure A.5 illustrates the deviations for selected reactions in the reaction energy with the corresponding calculation times.

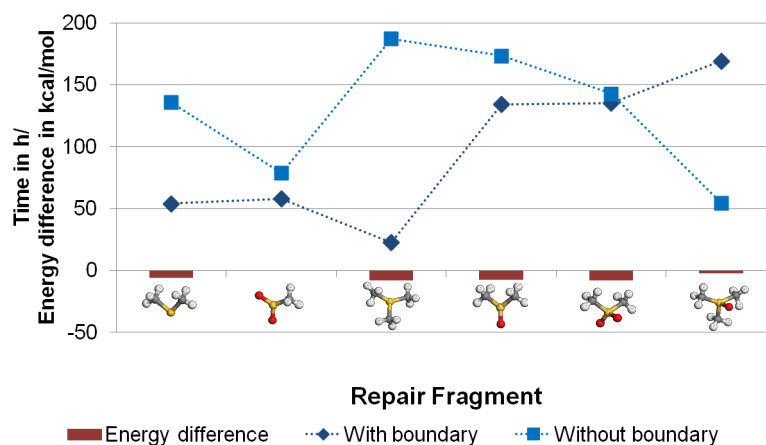


Figure A.5.: Energy and calculation time deviation of the silicon oxide cluster with (dark blue) and without a boundary (light blue). The dotted lines are only a guide for the eyes and show no correlations.

With one exception, the calculations from the cluster with a fixed boundary are always faster while the energy deviation is under 10 kcal/mol. Figure A.5 also shows that the calculation time differs for each repair fragment.

## A.3. Error Analysis

### A.3.1. Basis Set Superposition Error in Dmol<sup>3</sup>

The basis set superposition error (BSSE) has an important influence on the reaction energy when a small and a large molecule react, or when one reactant contains heavy atoms while the second reactant only consists of light atoms. In both cases, the smaller reactant has a smaller basis set and thus their wave functions are less flexible.

The BSSE can be calculated by subtracting the energy of the monomers from the dimer. This leads to an energy difference  $E_{BSSE}$  defined as:

$$E_{BSSE} = E_{Dimer} - \sum_i E_{Monomer_i} \quad (A.1)$$

Figure A.6 shows the BSSE for the reactions of the ULK-fragments with the repair fragments. Here, the BSSE is about  $\pm 8$  kcal/mol, with all open shell ULK fragments having a BSSE below 0 kcal/mol. This is still in the DFT error range of  $\pm 10$  kcal/mol.

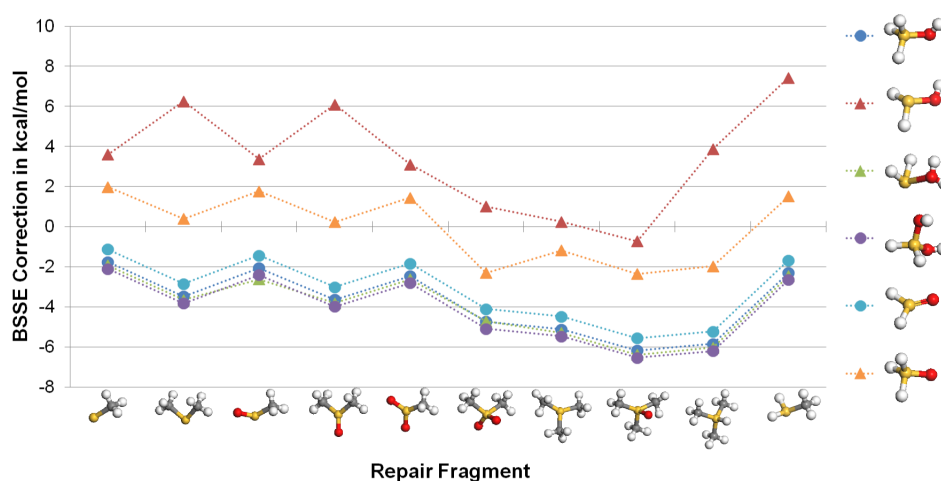


Figure A.6.: BSSE for ULK-fragment repair reactions in Dmol<sup>3</sup>. The ULK-fragments represented by dots are closed shell fragments, whereas the open shell ULK-fragments are displayed by triangles in the diagram. The dotted lines are only a guide for the eyes and show no correlations.

### A.3.2. Dispersion Correction

Chapter 3.2.2 stated that a dispersion correction was only used for Dmol<sup>3</sup>. To eliminate that the discrepancies between the Dmol<sup>3</sup> and Gaussian in chapter 5.1.3 are due to the use of the Grimme DFT-D correction, some of the H-damage repair reactions were re-calculated in Gaussian with dispersion corrections (see figure A.7).

As can be seen in figure A.7, the dispersion correction minimally changes the reaction energy for Gaussian. Thus, it can be concluded that the dispersion correction is not the source of the discrepancy between Dmol<sup>3</sup> and Gaussian results.

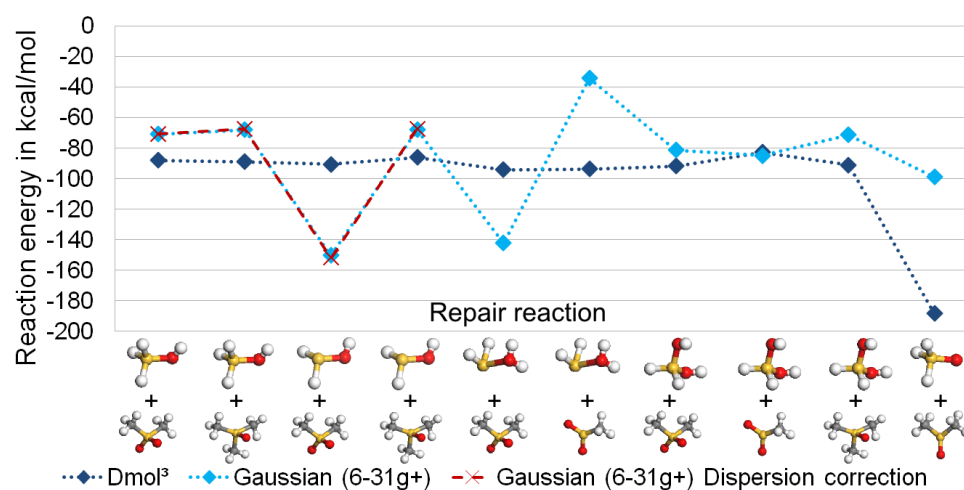


Figure A.7.: H-repair with dispersion correction. The Dmol<sup>3</sup> results (dark blue) already include the Grimme DFT-D correction. The dotted lines are only a guide for the eyes and show no correlations.

## A.4. Illustration of Defects

As described in chapter 4.1.1 the majority of the ULK-fragments stand for more than one defect. All additional molecules which are not part of the investigated defect are fixed during geometry optimizations. For example, both hydroxyl groups and one hydrogen atoms in  $\text{SiH}_2(\text{OH})_2$  are fixed when this ULK-fragment presents an H-damage.

As  $\text{SiH}_2\text{OH}_2$  and  $\text{SiH}_2(\text{OH})_2$  each model three different defects, they are used to illustrate the above described handling of the ULK-fragments. Figure A.8 shows the two ULK-fragments and one of their products for each defect they model. Here, the products visualize how the fixation of uninvolved atoms can change the final product (see figure A.8,  $\text{SiH}_2(\text{OH})_2$  as an OH- and  $(\text{OH})_2$ -defect).

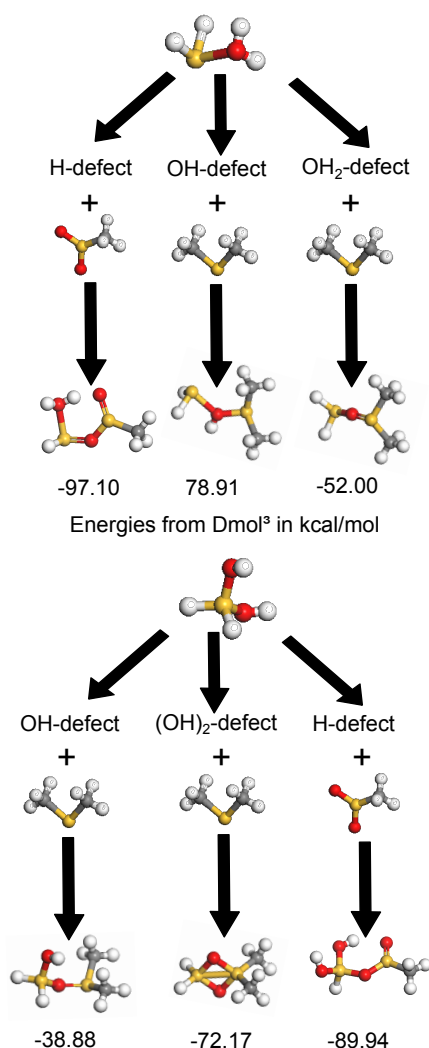


Figure A.8.: Illustration of the three different defect types  $\text{SiH}_2\text{OH}_2$  (upper scheme) and  $\text{SiH}_2(\text{OH})_2$  (lower scheme) are possessing. The final products illustrate with which atoms of the ULK-fragment the repair molecules reacted when the ULK-fragments are treated as a certain defect type. The desorbed  $0.5 \text{ H}_2$  or  $\text{H}_2$  molecule is not displayed.

## A.5. Bookmark

The printed version includes a bookmark that is displayed in figure A.9.

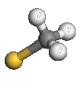
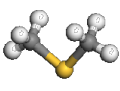
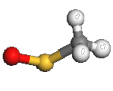
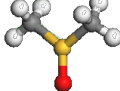
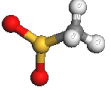
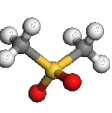
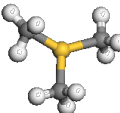
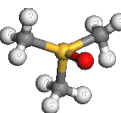
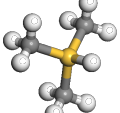
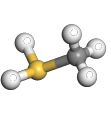
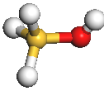
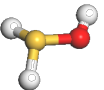
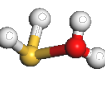
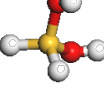
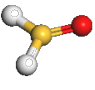
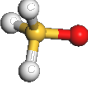
Repair fragments					
	SiCH <sub>3</sub>	Si(CH <sub>3</sub> ) <sub>2</sub>	SiOCH <sub>3</sub>	SiO(CH <sub>3</sub> ) <sub>2</sub>	SiO <sub>2</sub> CH <sub>3</sub>
					
	SiO <sub>2</sub> (CH <sub>3</sub> ) <sub>2</sub>	Si(CH <sub>3</sub> ) <sub>3</sub>	SiO(CH <sub>3</sub> ) <sub>3</sub>	Si(CH <sub>3</sub> ) <sub>3</sub> H	SiCH <sub>3</sub> H <sub>2</sub>
ULK-fragments					
	SiH <sub>3</sub> OH	SiH <sub>2</sub> OH	SiH <sub>2</sub> OH <sub>2</sub>	SiH <sub>2</sub> (OH) <sub>2</sub>	SiH <sub>2</sub> O
					
	SiH <sub>3</sub> O				

Figure A.9.: Bookmark

# Bibliography

- [1] W. Schroter, K. A. Jackson (Eds.), Handbook of Semiconductor Technology: Electronic Structure and Properties of Semiconductors Volume 1, Wiley-VCH, 2000.
- [2] J. Hruska, Samsung and GlobalFoundries buddy up for 14nm, while IBM heads for the exit, Online, [Accessed 23 September 2014] (2014).  
URL <http://www.extremetech.com/computing/181136-samsung-and-globalfoundries-buddy-up-for-14nm-while-ibm-heads-for-the-exit>
- [3] G. E. Moore, Cramming More Components onto Integrated Circuits, Electronics (1965) 114–117Reprinted version.  
URL <http://www.cs.utexas.edu/~fussell/courses/cs352h/papers/moore.pdf>
- [4] Intel, Excerpts from A Conversation with Gordon Moore: Moore’s Law, Online, accessed on 17.06.2014 (2005).  
URL [http://large.stanford.edu/courses/2012/ph250/lee1/docs/Excerpts\\_A\\_Conversation\\_with\\_Gordon\\_Moore.pdf](http://large.stanford.edu/courses/2012/ph250/lee1/docs/Excerpts_A_Conversation_with_Gordon_Moore.pdf)
- [5] Wgsimon, Transistor Count and Moore’s Law -2011, Online, [Accessed 17 June 2014].  
URL [en.wikipedia.org/wiki/File:Transistor\\_Count\\_and\\_Moore's\\_Law\\_-\\_2011.svg](http://en.wikipedia.org/wiki/File:Transistor_Count_and_Moore's_Law_-_2011.svg)
- [6] B. Weber (Ed.), TÜF - Tabellen, Übersichten, Formeln, Schroedel Verlag GmbH, Braunschweig, 2008.
- [7] Wikipedia, Relative permittivity-Wikipedia, The Free Encyclopedia, Online, [Accessed 19 June 2014] (2014).  
URL [http://en.wikipedia.org/wiki/Relative\\_permittivity#Terminology](http://en.wikipedia.org/wiki/Relative_permittivity#Terminology)
- [8] M. R. Baklanov, J.-F. de Marneffe, D. Shamiryan, A. M. Urbanowicz, H. Shi, T. V. Rakhimova, H. Huang, P. S. Ho, Plasma processing of low-k dielectrics, Journal of Applied Physics 113 (4). doi:<http://dx.doi.org/10.1063/1.4765297>.
- [9] J. Bao, H. Shi, J. Liu, H. Huang, P. Ho, M. D. Goodner, M. Moinpour, G. M. Kloster, Mechanistic Study of Plasma Damage and CH<sub>4</sub> Recovery of Low k Dielectric Surface, in: International Interconnect Technology Conference, IEEE 2007, 2007, pp. 147–149. doi:10.1109/IITC.2007.382366.
- [10] N. Köhler, Entwicklung eines Prozesses zur plasmagestützten Reparatur geschädigter ultra low-k Materialien in der 28 nm Technologie, Diploma Thesis, TU Chemnitz (2014).
- [11] M. Baklanov, P. S. Ho, E. Zschech (Eds.), Advanced Interconnects for ULSI Technology, 1st Edition, John Wiley & Sons, New York, 2012.

## Bibliography

- [12] K. Maex, M. R. Baklanov, D. Shamiryan, F. Iacopi, S. H. Brongersma, Z. S. Yanovitskaya, Low dielectric constant materials for microelectronics, *Journal of Applied Physics* 93 (11) (2003) 8793–8841. doi:<http://dx.doi.org/10.1063/1.1567460>.
- [13] M. Baklanov, K. Maex, M. Green (Eds.), *Dielectric films for advanced microelectronics*, 1st Edition, John Wiley & Sons, New York, 2007.
- [14] A. Grill, V. Patel, Ultralow-k dielectrics prepared by plasma-enhanced chemical vapor deposition, *Applied Physics Letters* 79 (6) (2001) 803–805. doi:<http://dx.doi.org/10.1063/1.1392976>.
- [15] A. Grill, V. Patel, Ultralow dielectric constant pSiCOH films prepared with tetramethylcyclotetrasiloxane as skeleton precursor, *Journal of Applied Physics* 104 (2) (2008) –. doi:<http://dx.doi.org/10.1063/1.2959341>.
- [16] Y. Shacham-Diamand, T. Osaka, M. Datta, T. Ohba, Y. Shacham-Diamand, T. Osaka, M. Datta, T. Ohba (Eds.), *Advanced Nanoscale ULSI Interconnects: Fundamentals and Applications*, first edition Edition, Springer, Berlin, Heidelberg, 2009.
- [17] K. Kurihara, T. Ono, K. Kohmura, H. Tanaka, N. Fujii, N. Hata, T. Kikkawa, Carbon loss induced by plasma beam irradiation in porous silica films, *Journal of Applied Physics* 101 (11). doi:<http://dx.doi.org/10.1063/1.2740334>.
- [18] T. Oszinda, M. Schaller, D. Fischer, C. Walsh, S. E. Schulz, Investigation of physical and chemical property changes of ultra low-k SiOCH in aspect of cleaning and chemical repair processes, *Microelectronic Engineering* 87 (3) (2010) 457 – 461, materials for Advanced Metallization 2009 Proceedings of the eighteenth European Workshop on Materials for Advanced Metallization 2009. doi:<http://dx.doi.org/10.1016/j.mee.2009.06.028>.
- [19] Y. Li, I. Ciofi, L. Carbonell, N. Heylen, J. Van Aelst, M. R. Baklanov, G. Groeseneken, K. Maex, Z. Tokei, Influence of absorbed water components on SiOCH low-k reliability, *Journal of Applied Physics* 104 (3). doi:<http://dx.doi.org/10.1063/1.2966578>.
- [20] H. Ren, G. A. Antonelli, Y. Nishi, J. L. Shohet, Plasma damage effects on low-k porous organosilicate glass, *Journal of Applied Physics* 108 (9). doi:<http://dx.doi.org/10.1063/1.3506523>.
- [21] H.-S. Lu, K. Gottfried, N. Ahner, S. Schulz, X.-P. Qu, Surface modification of porous low-k material by plasma treatment and its application on reducing the damage from sputtering and CMP process, in: *Interconnect Technology Conference and 2011 Materials for Advanced Metallization (IITC/MAM)*, 2011 IEEE International, 2011, pp. 1–3. doi:10.1109/IITC.2011.5940315.
- [22] T. Oszinda, M. Schaller, S. E. Schulz, Chemical Repair of Plasma Damaged Porous Ultra Low- k SiOCH Film Using a Vapor Phase Process, *Journal of The Electrochemical Society* 157 (12) (2010) H1140–H1147. doi:10.1149/1.3503596.
- [23] H. Shi, Mechanistic study of plasma damage to porous low-k process development and dielectric recovery, Phd thesis, The University of Texas at Austin (2001). URL <http://repositories.lib.utexas.edu/bitstream/handle/2152/ETD-UT-2010-05-749/SHI-DISSERTATION.pdf>
- [24] O. Böhm, R. Leitsmann, P. Plänitz, C. Radehaus, M. Schreiber, M. Schaller, k-Restoring Processes at Carbon Depleted Ultralow-k Surfaces, *The Journal of Physical Chemistry A* 115 (29) (2011) 8282–8287. doi:10.1021/jp202851p.



- [25] O. Böhm, R. Leitsmann, P. Plänitz, T. Oszinda, M. Schaller, M. Schreiber, Novel k-restoring scheme for damaged ultra-low-k materials, *Microelectronic Engineering* 112 (0) (2013) 63 – 66. doi:<http://dx.doi.org/10.1016/j.mee.2013.05.017>.
- [26] N. Azizi, M. R. Saidi, Novel and Efficient Method for the Silylation of Hydroxyl Groups with Hexamethyldisilazane (HMDS) under Solvent-Free and Neutral Conditions, *Organometallics* 23 (6) (2004) 1457–1458. doi:10.1021/om0341505.
- [27] T. Oszinda, Characterization and chemical recovery of plasma damaged porous low-k SiOCH dielectric for the semiconductor industry, Ph.D. thesis, TU Chemnitz (2012).  
URL <http://publica.fraunhofer.de/eprints/urn:nbn:de:0011-n-1971787.pdf>
- [28] A. Grill, Porous psicoh ultralow-k dielectrics for chip interconnects prepared by pecvd, *Annual Review of Materials Research* 39 (1) (2009) 49–69. doi:10.1146/annurev-matsci-082908-145305.
- [29] zero-point vibrational energy (ZPVE), Excerpt of "IUPAC Compendium of Chemical Terminology ", [Accessed 17 September 2014] (2006).  
URL <http://old.iupac.org/goldbook/ZT07133.pdf>
- [30] E. G. Lewars, *Computational Chemistry - Introduction to the Theory and Applications of Molecular and Quantum Mechanics*, 2nd Edition, Springer, 2011.
- [31] D. W. Brenner, Empirical potential for hydrocarbons for use in simulating the chemical vapor deposition of diamond films, *Physical Review B* 42 (1990) 9458–9471. doi:10.1103/PhysRevB.42.9458.
- [32] S. L. Mayo, B. D. Olafson, W. A. Goddard III, DREIDING: A Generic Force Field for Molecular Simulations, *Journal of Physical Chemistry* 94 (1990) 8897–8909.
- [33] A. C. T. van Duin, S. Dasgupta, F. Lorant, W. A. Goddard III, ReaxFF: A Reactive Force Field for Hydrocarbons, *Journal of Physical Chemistry A* 105 (2001) 9396–9409.
- [34] W. Koch, M. C. Holthausen:, *A Chemist's Guide to Density Functional Theory*, 2nd Edition, WILEY-VCH Verlag, Weinheim, 2001.
- [35] A. Förster, Ab-initio studies of reactions to functionalize carbon nanotubes, Bachelor Thesis, TU Chemnitz (2012).  
URL <http://nbn-resolving.de/urn:nbn:de:bsz:ch1-qucosa-103907>
- [36] P. Hohenberg, W. Kohn, Inhomogeneous electron gas, *Physical Review* 136 (3B) (1964) B864–B871. doi:10.1103/PhysRev.136.B864.
- [37] W. Kohn, L. J. Sham, Self-consistent equations including exchange and correlation effects, *Physical Review* 140 (4A) (1965) A1133–A1138. doi:10.1103/PhysRev.140.A1133.
- [38] A. D. Boese, J. M. L. Martin, N. C. Handy, The role of the basis set: Assessing density functional theory, *The Journal of Chemical Physics* 119 (6) (2003) 3005–3014. doi:<http://dx.doi.org/10.1063/1.1589004>.
- [39] K. Capelle, A Bird's-Eye View of Density-Fuctional Theory, *Brazilian Journal of Physics* 36 (4A) (2006) 1318–1343.  
URL <http://arxiv.org/abs/cond-mat/0211443>

## Bibliography

- [40] Unknown Author, Molecular Simulations Inc, DMol in Insight & standalone, Online, accessed on 30.05.2014 (1998).  
URL [http://hincklab.uthscsa.edu/html/soft\\_packs/msi\\_docs/insight980/dmol/2\\_Theory.html#194048](http://hincklab.uthscsa.edu/html/soft_packs/msi_docs/insight980/dmol/2_Theory.html#194048)
- [41] K. Riley, B. Op't Holt, K. Merz Jr., Critical assessment of the performance of density functional methods for several atomic and molecular properties, *Journal of Chemical Theory and Computation* 3 (2) (2007) 407–433.
- [42] F. Jensen, *Introduction to Computational Chemistry*, 2nd Edition, Wiley, 2007.
- [43] W. J. Hehre, R. Ditchfield, J. A. Pople, Self-Consistent Molecular Orbital Methods. XII. Further Extensions of Gaussian-Type Basis Sets for Use in Molecular Orbital Studies of Organic Molecules, *The Journal of Chemical Physics* 56 (5) (1972) 2257–2261. doi:<http://dx.doi.org/10.1063/1.1677527>.
- [44] M. J. Frisch, G. W. Trucks, H. B. Schlegel, G. E. Scuseria, M. A. Robb, J. R. Cheeseman, G. Scalmani, V. Barone, B. Mennucci, G. A. Petersson, H. Nakatsuji, M. Caricato, X. Li, H. P. Hratchian, A. F. Izmaylov, J. Bloino, G. Zheng, J. L. Sonnenberg, M. Hada, M. Ehara, K. Toyota, R. Fukuda, J. Hasegawa, M. Ishida, T. Nakajima, Y. Honda, O. Kitao, H. Nakai, T. Vreven, J. A. Montgomery, Jr., J. E. Peralta, F. Ogliaro, M. Bearpark, J. J. Heyd, E. Brothers, K. N. Kudin, V. N. Staroverov, R. Kobayashi, J. Normand, K. Raghavachari, A. Rendell, J. C. Burant, S. S. Iyengar, J. Tomasi, M. Cossi, N. Rega, J. M. Millam, M. Klene, J. E. Knox, J. B. Cross, V. Bakken, C. Adamo, J. Jaramillo, R. Gomperts, R. E. Stratmann, O. Yazyev, A. J. Austin, R. Cammi, C. Pomelli, J. W. Ochterski, R. L. Martin, K. Morokuma, V. G. Zakrzewski, G. A. Voth, P. Salvador, J. J. Dannenberg, S. Dapprich, A. D. Daniels, . Farkas, J. B. Foresman, J. V. Ortiz, J. Cioslowski, D. J. Fox, Gaussian 09 Revision D.01, gaussian Inc. Wallingford CT 2009.
- [45] B. Delly, An all-electron numerical method for solving the local density functional for polyatomic molecules, *The Journal of Chemical Physics* 92 (1) (1990) 508–517.
- [46] B. Delly, From molecules to solids with the DMol3 approach, *The Journal of Chemical Physics* 113 (18) (2000) 7756–7764. doi:10.1063/1.1316015.
- [47] Accelrys Software Inc., *Materials Studio Release Notes*, Release 6.0, San Diego Accelrys Software Inc., 2011.
- [48] J. P. Perdew, K. Burke, M. Ernzerhof, Generalized Gradient Approximation Made Simple, *Physical Review Letters* 77 (18) (1996) 3865–3868. doi:10.1103/PhysRevLett.77.3865.
- [49] A. D. Becke, Density-functional exchange-energy approximation with correct asymptotic behavior, *Physical Review A* 38 (1988) 3098–3100. doi:10.1103/PhysRevA.38.3098.
- [50] C. Lee, W. Yang, R. G. Parr, Development of the Colle-Salvetti correlation-energy formula into a functional of the electron density, *Physical Review B* 37 (1988) 785–789. doi:10.1103/PhysRevB.37.785.
- [51] S. H. Vosko, L. Wilk, M. Nusair, Accurate spin-dependent electron liquid correlation energies for local spin density calculations: a critical analysis, *Canadian Journal of Physics* 58 (1980) 1200. doi:10.1139/p80-159.
- [52] B. Delly, Ground-state enthalpies: evaluation of electronic structure approaches with emphasis on the density functional method, *The Journal of Physical Chemistry A* 110 (50) (2006) 13632–13639. doi:10.1021/jp0653611.

- [53] A. C. T. van Duin, J. M. A. Baas, B. van de Graaf, Delft molecular mechanics: a new approach to hydrocarbon force fields. Inclusion of a geometry-dependent charge calculation, *J. Chem. Soc., Faraday Trans.* 90 (1994) 2881–2895. doi:10.1039/FT9949002881.
- [54] A. C. T. van Duin, A. Strachan, S. Stewman, Q. Zhang, X. Xu, W. A. Goddard III, ReaxFF-SiO Reactive Force Field for Silicon and Silicon Oxide Systems, *The Journal of Physical Chemistry A* 107 (19) (2003) 3803–3811. doi:10.1021/jp0276303.
- [55] S. Plimpton, Fast Parallel Algorithms for Short-Range Molecular Dynamics, *Journal of Computational Physics* 117 (1) (1995) 1–19. doi:http://dx.doi.org/10.1006/jcph.1995.1039.
- [56] J. D. Gale, P. Raiteri, A. C. T. van Duin, A reactive force field for aqueous-calcium carbonate systems, *Phys. Chem. Chem. Phys.* 13 (2011) 16666–16679. doi:10.1039/C1CP21034C.
- [57] T. T. Jarvi, A. C. T. van Duin, K. Nordlund, W. A. Goddard III, Development of Interatomic ReaxFF Potentials for AuSCH Systems, *The Journal of Physical Chemistry A* 115 (37) (2011) 10315–10322. doi:10.1021/jp201496x.
- [58] O. Rahaman, A. C. T. van Duin, W. A. Goddard III, D. J. Doren, Development of a ReaxFF Reactive Force Field for Glycine and Application to Solvent Effect and Tautomerization, *The Journal of Physical Chemistry B* 115 (2) (2011) 249–261. doi:10.1021/jp108642r.
- [59] M. Aryanpour, A. C. T. van Duin, J. D. Kubicki, Development of a Reactive Force Field for IronOxyhydroxide Systems, *The Journal of Physical Chemistry A* 114 (21) (2010) 6298–6307. doi:10.1021/jp101332k.
- [60] D. Raymand, A. C. van Duin, D. Spangberg, W. A. Goddard III, K. Hermansson, Water adsorption on stepped ZnO surfaces from "MD" simulation, *Surface Science* 604 (2010) 741–752. doi:http://dx.doi.org/10.1016/j.susc.2009.12.012.
- [61] D. A. Newsome, D. Sengupta, H. Foroutan, M. F. Russo, A. C. T. van Duin, Oxidation of Silicon Carbide by O<sub>2</sub> and H<sub>2</sub>O: A ReaxFF Reactive Molecular Dynamics Study, Part I, *Journal of Physical Chemistry C* 116 (2012) 16111–16121.
- [62] D. A. Newsome, D. Sengupta, A. C. T. van Duin, High-Temperature Oxidation of SiC-Based Composite: Rate Constant Calculation from ReaxFF MD Simulations, Part II, *Journal of Physical Chemistry C* 117 (2013) 5014–5027.
- [63] A. D. Kulkarni, D. G. Truhlar, S. G. Srinivasan, A. C. T. van Duin, P. Norman, T. E. Schwartzenuber, Oxygen Interactions with Silica Surfaces: Coupled Cluster and Density Functional Investigation and the Development of a New ReaxFF Potential, *Journal of Physical Chemistry C* 117 (2013) 285–269.
- [64] L. Zhang, S. V. Zybin, A. C. T. van Duin, S. Dasgupta, W. A. Goddard III, Carbon Cluster Formation during Thermal Decomposition of Octahydro-1,3,5,7-tetranitro-1,3,5,7-tetrazocine and 1,3,5-Triamino-2,4,6-trinitrobenzene High Explosives from ReaxFF Reactive Molecular Dynamics Simulations, *Journal of Physical Chemistry A* 113 (2009) 10619–10640.
- [65] K. D. Nielson, A. C. T. van Duin, a. W.-Q. D. Jonas Oxgaard, W. A. Goddard III, Development of the ReaxFF Reactive Force Field for Describing Transition Metal Catalyzed Reactions, with Application to the Initial Stages of the Catalytic Formation of Carbon Nanotubes, *Journal of Physical Chemistry A* 109 (2005) 493–499.

## *Bibliography*

- [66] Lammps distribution from 12.01.2013.
- [67] J. Clark, The oxides of group 4, Online (2004).  
URL <http://www.chemguide.co.uk/inorganic/group4/oxides.html>
- [68] N. Köhler, Untersuchung des Repair-Effektes verschiedener Flüssigpräkursoren und Gaszusätze auf plasmageschädigten ultra low-k Schichten, Student research project, TU Chemnitz (2013).
- [69] S. Zimmermann, N. Köhler, T. Fischer, A. Förster, C. Wagner, J. Schuster, S. Gemming, S. Schulz, T. Gessner, Development of an in situ k-value-restore process with plasma enhanced fragmentation of liquid repair chemicals, Journal of Applied Physics, Submitted Manuscript.
- [70] L. A. Curtiss, K. Raghavachari, P. C. Redfern, J. A. Pople, Assessment of Gaussian-2 and density functional theories for the computation of enthalpies of formation, The Journal of Chemical Physics 106 (3) (1997) 1063–1079. doi:<http://dx.doi.org/10.1063/1.473182>.

# Acknowledgment

I thank Prof. Dr. Sibylle Gemming for accepting the position of the first examiner, as well as for her scientific advices and her feedback regarding the creation of this work during various discussions.

Secondly, I would like to thank Prof. Dr. Stefan E. Schulz for accepting the position of second examiner and giving me the opportunity to write my thesis in his Back-end of Line department of the Fraunhofer ENAS.

I would also like to thank the whole group of the Back-end of Line department in the Fraunhofer ENAS for their support. Especially Dr. Jörg Schuster and Christian Wagner for their feedback and helpful advice to improve this work. I thank Nicole Köhler for our discussions where we exchanges experimental and theoretical insights on the investigated topic.



# Statement of Authorship



TECHNISCHE UNIVERSITÄT CHEMNITZ

## Zentrales Prüfungsamt

(Anschrift: TU Chemnitz, 09107 Chemnitz)

### Selbstständigkeitserklärung\*

Name:	<b><u>Bitte Ausfüllhinweise beachten:</u></b> 1. Nur Block- oder Maschinenschrift verwenden.
Vorname:	
geb. am:	
Matr.-Nr.:	

Ich erkläre gegenüber der Technischen Universität Chemnitz, dass ich die vorliegende  
selbstständig und ohne Benutzung anderer als der  
angegebenen Quellen und Hilfsmittel angefertigt habe.

Die vorliegende Arbeit ist frei von Plagiaten. Alle Ausführungen, die wörtlich oder inhaltlich  
aus anderen Schriften entnommen sind, habe ich als solche kenntlich gemacht.

Diese Arbeit wurde in gleicher oder ähnlicher Form noch bei keinem anderen Prüfer als  
Prüfungsleistung eingereicht und ist auch noch nicht veröffentlicht.

Datum: .....

Unterschrift: .....

\* Diese Erklärung ist der eigenständig erstellten Arbeit als Anhang beizufügen.